Model-based estimation of seafloor parameters by use of acoustic backscattering

Bjarte Berntsen

Submitted to
the Norwegian University of Science and Technology
in partial fulfillment of the requirements
for the degree of
Doktor ingeniør

Norwegian University of Science and Technology
Department of Telecommunications
N-7491 Trondheim, Norway

June, 2001

Abstract

An algorithm for characterization of the seafloor by use of a parametric acoustic source has been developed. It is called FARIM – Frequency Analysis based Roughness and Impedance estimation Method. The work was done within the ISACS MAST-III project. ISACS is an acronym for Integrated System for Analysis and Characterization of the Seafloor.

The properties of a monostatic sonar system has been investigated, and the different processes identified and studied.

Various approaches to classification and characterization have been studied, and the necessary theory for understanding the developed characterization technique is presented in this thesis. A model-based approach was chosen, in order to improve the understanding of the problem and obtain a robust and traceable characterization method. The Kirchhoff theory was chosen for modeling the scattering from the seafloor.

The characterization algorithm itself is described. Changes in the frequency distribution as the roughness increases is used for estimating the roughness, as the low frequency components are less influenced by roughness. The energy of the return is used for estimating the impedance of the seafloor, while correcting for the estimated roughness and near-field effects of the parametric source and possibly also for the seafloor bathymetry.

Sensitivity analysis indicates that good estimation of seafloor roughness and impedance should be feasible, assuming moderate roughness compared to the probing wavelength. The chosen characterization features (center-of-gravity of the power spectrum and the energy of the return) are rather insensitive to most parameters of the chosen seafloor description. However, the features are relatively sensitive to the high-pass cut-off frequency of the power spectrum for the seafloor roughness, and this should be further studied. Stacking is shown to improve the parameter estimation.

The algorithm was tested on both synthetic and field data. The test on synthetic data was done both to verify the numerical implementation of the algorithm and to study the accuracy. The test showed excellent agreement between real values and the estimates, when the roughness was moderate, and suitable error estimates as reliable indicators of the accuracy of the estimates were found.

Field data from the Mediterranean, North Sea and Baltic have been analyzed. The estimates show very good agreement with the available ground truth data. We feel however that still more work should be done to verify the estimation technique on field data.

The estimation technique is numerically very quick, and the calculations can be done in real time.

A parametric source has been found to be suitable for use with this characterization technique, and the field data analyzed in this report was acquired with a parametric sonar.

Preface

This dissertation is submitted to the Norwegian University of Science and Technology, NTNU, in partial fulfillment of the requirements for the degree of Doktor ingeniør.

The work has been performed at the Acoustic group at the Department of Telecommunications at the Faculty for Electrical and Electronics Engineering, NTNU, in the years from 1996 to 2000. Professor Jens M. Hovem, of the Acoustic group, has been my supervisor. The work was done within the framework of the ISACS project, in the MAST-3 programme of EC. ISACS is an acronym for Integrated System for Analysis and Characterization of the Seafloor. The ISACS project started in March 1996 and finished in August 1999. I have been employed at the Department of Telecommunications at NTNU, and financed mainly through the ISACS project and partly through the Department of Telecommunications.

I want to thank Jens M. Hovem for being my supervisor, and the committee – Ilkka Karasalo, Freddy Pøhner and Peter Svensson – for doing a nice job and giving me good feedback. I also want to thank all the participants of the ISACS project for a fruitful collaboration. I want to especially mention Ilkka Karasalo from FOA, Oddbjørn Bergem and Eric Pouliquen from SACLANTCEN, Johnny Dybedal at Kongsberg Simrad, Andrea Caiti at University of Pisa and Svein Arne Frivik from Aker Geo. I am grateful to Svein Arne Frivik and Geir Helge Sandsmark (Simrad AS) for proof reading my manuscript. Also many thanks to my colleagues in the Acoustic group, and especially the Doctoral students, for fruitful discussions and many coffee breaks. Finally I want to thank my parents, Astrid and Arne Berntsen, for always supporting me.

Contents

Nomenclature

Symbols

Most of the symbols used in this thesis are defined below. Some symbols that only have a local meaning are only defined close to where they are used.

A	$= \hat{k}_x^- = \sin\theta_1 - \sin\theta_2 \cos\theta_3$; x-component of the unit change of the wavevector
A_M	Area of mean plane of scattering surface
B	$= \hat{k}_y^- - \sin\theta_2 \sin\theta_3$; y-component of the unit change of the wavevector
C	$= \hat{k}_z^- - (\cos\theta_1 + \cos\theta_2)$; z-component of the unit change of the wavevector
D_i	Directivity pattern for the incoming field (i.e. for the source)
D_r	Directivity pattern for the reflected field (i.e. for the receiver)
E_{field}	Total energy of the field data
$E_{ref}(d, \sigma)$	Reference energy, calculated from theory and synthetic data, as a function of depth and RMS roughness
$E_{surface}$	Energy content of the surface part of the trace
E_{volume}	Energy content of the volume part of the trace
$F(\theta_1, \theta_2, \theta_3)$	$= \frac{1}{2}\left(\frac{Aa}{C} + \frac{Bb}{C} + c\right)$
$F(r)$	Shape function, e.g. a beam pattern
I_0	Intensity of a field scattered from a smooth surface
I_d	Diffuse field intensity from a rough surface

J_0	The zeroth-order Bessel function of the first kind
K	$= 2\pi/\lambda = \omega/v$, wave number
K_{hp}	High-pass wave number, for use in filtering
K_{lp}	Low-pass wave number, for use in filtering
N	Number of samples
$P^0(d)$	Power spectrum for a smooth surface, as a function of depth
$P_{ijk}(d_j, \sigma_k)$	Power spectrum, as a function of depth and RMS roughness, calculated from theory and P^0
R	Distance from the acoustic source to the wave front
R_a	Rayleigh parameter ($=k\sigma\cos\theta_1$)
R_1	Distance of penetration into the sediment ($\mathbf{r}^{'} = \mathbf{r} + \mathbf{R_1}$)
S_0	Surface of integration
$W[n]$	Window function
W_s	Band-passed power law spectrum
X	Limit of the surface, in x-direction
Y	Limit of the surface, in y-direction
$Z = \rho v$	Impedance
Z_{field}	Impedance of the field data
Z_{ref}	Reference value of impedance
$\Delta\phi$	Phase difference
Δh	Height difference between points where acoustic rays hit the surface
Δt	Time delay
Δt_{pulse}	Pulse length
Δt_{rough}	Time delay due to roughness
$\Delta\Phi$	Phase shift (in Fresnel zones)
α	Attenuation coefficient
β	Attenuation, given in dB/m
ε	Smoothing coefficient
$\chi(kC)$	One-dimensional characteristic function of the surface

η	Normalization factor, in the power law for generation of surfaces
λ	Wave length
λ_0	Horizontal correlation length
λ_p	Compressional wavelength
$\mathbf{K}$	Two-dimensional wave vector
$\mathcal{R}$	Reflection coefficient
$\mathcal{R}_{01}$	Reflection coefficient between layer 0 and 1
$\mathcal{R}_{ref}$	Reference reflection coefficient
$\mathcal{T}$	Transmission coefficient
$\mathcal{T}_{01}$	Transmission coefficient between layer 0 and 1
$\mathcal{T}_{10}$	Transmission coefficient between layer 1 and 0
μ	Volume inhomogeneities factor
ν	Exponent in power spectrum for fractal surfaces
ω	Angular frequency
$\overline{c_0}$	Average sound speed in water
$\overline{n_1}$	Average refractive index in the first few meters of the bottom
ϕ	Phase function
ψ	The total field: $\psi(\mathbf{r}) = \psi^{inc}(\mathbf{r}) + \psi^{sc}(\mathbf{r})$
ψ^{inc}	Incoming field
ψ^{sc}	Scattered field
ψ_0^{sc}	Scattered field from a smooth surface
ψ_e	Edge effects
ρ	Density
ρ_0	Density of water
ρ_1	Density of sediment
σ	RMS roughness
θ	Angle
θ_1	Incident angle, relative to z direction
θ_2	Scattered angle, relative to z direction
θ_3	Scattered angle, out of the plane of incidence

θ_{beam}	Half beam width
θ_{max}	Maximum beam angle
$\mathbf{R}$	Vector from the acoustic source to a point
$\mathbf{R}_1$	Distance of penetration into the sediment ($\mathbf{r}^{'} = \mathbf{r} + \mathbf{R_1}$)
$\mathbf{n}$	Unit surface normal at point $\mathbf{r}_0$, pointing towards the surface
$\mathbf{r}$	Scattering point, generally away from the surface
$\mathbf{r}^{'} = \mathbf{r} + \mathbf{R_1}$	Location of volume element
$\mathbf{r}_0$	Vector from the origin on the seafloor surface to another point on this surface
a	$= \sin\theta_1(1-\mathcal{R}) + \sin\theta_2\cos\theta_3(1+\mathcal{R})$
b	$= \sin\theta_2\sin\theta_3(1+\mathcal{R})$
cc	$= \cos\theta_2(1+\mathcal{R}) - \cos\theta_1(1-\mathcal{R})$
c	Compressional sound speed
c_0	Compressional sound speed in water
c_1	Compressional sound speed in sediment
$e(t)$	Transmitted pulse (with derivatives $e^{''}(t)$, $e^{'}(t)$)
f	Frequency
f_{CofG}	Center-of-gravity frequency
f_s	Sampling frequency
h	Water depth
$k = 2\pi/\lambda$	Wave number
l_h	Horizontal correlation length
l_v	Vertical correlation length
l_{pulse}	Length of pulse
l_{rough}	A characteristic scale of the roughness, e.g. σ
n_1	Local refractive index at the location $\mathbf{r}^{'}$ of the volume element
p	Acoustic pressure
p_0	Average pressure of the signal, in the center of the beam
p_i	Pressure of incident beam
p_r	Pressure of reflected beam

p_t	Pressure of transmitted beam
t	Time
x	Direction parallel to surface mean plane, within the plane of incidence
y	Direction parallel to surface mean plane, perpendicular to the plane of incidence
z	Direction perpendicular to the surface mean plane
$\mathbf{P}$	Pressure field received at the source position

Abbreviations

BORIS	BOttom Response from Inhomogeneities and Surface (a numerical model for calculating backscattering from the seafloor)
$CofG$	Center-of-gravity
FARIM	Frequency Analysis based Roughness and Impedance estimation Method (the seafloor characterization algorithm described in this report)
FFT	Fast Fourier Transform
ISACS	Integrated System for Analysis and Characterization of the Seafloor (a MASTIII project)
sirOb	Seafloor Identification by Remote Sensing Of the Bottom (a seafloor characterization algorithm, using inversion)

Chapter 1

Introduction

The ocean covers more than 70% of the Earth's surface. It supplies food and is used for transportation as well as for recreation, and is a source of inspiration and reflection for many of us. It has however not been that easy to find out what is hidden beneath its surface. Electromagnetic waves do not penetrate well in water, especially in sea water, so they may only been used for fairly short distances. In fact, sometimes the visibility in water is extremely poor, perhaps only a few centimeters. Mechanical probing of the seafloor can be used, but is in general time consuming and expensive. What we are left with then is acoustic methods, which can be used for exploring large areas of both seafloor and volume much more effectively and less expensively than alternative methods.

Underwater acoustics is important in the fishing industry, both for estimating the number of fish in the sea (science and fishery politics), and for fishing vessels in their search for fish. Determination of seafloor properties can also be important for fisheries, as different fish lives in different habitats.

Seafloor properties and bathymetry are important for navigation (both for surface vessels and submarines), scientific purposes, off-shore purposes as when placing cables or equipment on the seafloor, underwater archeology and numerous other purposes. The military is also an extensive user of underwater acoustics, for surveillance (e.g. submarines), mine counter measures (MCM), communication, modeling of the seafloor (e.g. to improve sonar performance) etc.

There is thus a lot of interest in development of underwater acoustics, and there is still a lot of work to be done. This thesis reports on an effort to improve characterization of the seafloor by utilizing properties of sub-bottom profilers. The work includes implementation of suitable processing by using existing or newly developed strategies, as appropriate, as well as verification and testing of the developed algorithms.

1.1 The ISACS project

The work in this thesis has been done within the ISACS project. ISACS is an acronym for Integrated System for Analysis and Characterization of the Seafloor. Most of the information below are taken from [16] and [36].

The ISACS project started in March 1996 and finished in August 1999. The total cost of the project has been 2.1 million EURO of which the MAST-3 programme contributed 1.4 million EURO. The project coordinator was Jens M. Hovem from NTNU, Norway.

The partners of the project were:

- Norwegian University of Science and Technology (NTNU), Norway
- Universita degli Studie de Genova (DIST), Italy
- Universidade do Algarve (UALG), Portugal.
- Kongsberg Defence and Aerospace AS (KDA), Norway
- National Defence Research Establishment (FOA), Sweden
- Royal Institute of Technology (KTH), Sweden
- SACLANT Undersea Research Centre (SACLANTCEN), Italy
- Fugro Consultants International (FUGRO), The Netherlands

The objective of ISACS was to prove the feasibility of analysis and characterization of the seafloor by exploitation and suitable integration of data gathered from commercially available sonar equipment [16]. The input data was acoustic backscattered data. The data was acquired by multibeam echo sounder, side-scan-sonar and bottom penetrating parametric sonar. The objective was to determine geoacoustic properties from the acoustic backscattered data and to detect and possibly identify buried or semi-buried objects.

The project included 5 main tasks:

1. Field data acquisition. The data was primarily intended to be used within the ISACS project.
2. Data fusion and pre-processing, which involved choice of data formats and development of software (TRISMAP – TRIangulated Sea MAPs [16]) for determination of local grazing angle from bathymetric data.
3. Volume image processing, using data from the parametric bottom-penetrating sonar TOPAS PS040, and also integration with seafloor information from multibeam echosounder.
4. Data inversion and seafloor characterization/classification. Two seafloor characterization approaches were developed within the project; an inversion method called sirOb (Seafloor model Identification by acoustic Remote sensing Of the Bottom [16]) and the method FARIM (Frequency Analysis based Roughness and Impedance estimation Method) which is described in this report.
5. Test of the concept, which was an evaluation of the project.

The work reported on in this thesis was to be within task 4 of the ISACS project, and more specifically on characterization/classification of the seafloor using the parametric sonar TOPAS PS040. The focus of the work was therefore on finding or developing a suitable method for utilizing this specific kind of instrument (but not necessarily limited to parametric sonars). The main goal was to produce a working algorithm, verify it and test this on field data. The verification should preferably be done by checking it on synthetic data and by analytical investigation. A model-based approach was preferred to a statistical approach. The necessary understanding of the physics involved was believed to be favorable, and make it easier to establish the limits of the method. This could be more difficult when using a statistical approach.

1.2 Definition of the problem

The seafloor may be very complex, and an exact description of it is neither possible nor wanted. What we want is to do the description as accurate as necessary without making it too complex. The best way of describing the seafloor may thus highly depend on the purpose of the analysis. At the same time, the description of the seafloor is dependent upon available instrumentation and processing capacity.

The work described in this thesis has been done within the ISACS project. The focus in this project was on relatively shallow waters, and on gaining information about the seafloor surface and the first few meters of the seafloor. This put certain limits on possible equipment, as penetration into the seafloor is best for low frequencies (due to attenuation, see Sec. 2.3).

In a seafloor characterization, emphasis should be on estimating properties useful for geoacoustical description of the seafloor surface and subsurface. Such properties include seafloor surface (and subsurfaces) roughness, compressional and shear speed and attenuation (both as a function of depth), density as a function of depth, identification of sediment and rock types, true thicknesses and shapes of layers [33]. The available instrumentation limits the possibility of estimating all of these properties, e.g. compressional sound speed (v) and density (ρ) will only be identified together in the form of impedance ($Z = \rho v$), when using a monostatic system. The focus was also chosen to be on the surface parameters, i.e. roughness and impedance.

1.3 Analysis and description of the seafloor – state-of-the-art

A detailed analysis and description of the seafloor is necessary (or at least useful) for many applications, both civilian and military. The needed accuracy of the description may depend on the actual application. The terms segmentation, classification and characterization are often used in order to differentiate between various ways of describing the seafloor. However, it seems not to be any common definition of these terms in the literature, and they are sometimes used ambiguously. We choose to use the following definitions[1]:

Characterization: Quantitative determination of the specific parameters describing the seafloor. One possible set of such parameters is sediment sound speed and density, seafloor roughness, volume attenuation and volume inhomogeneities[2].

Classification: Qualitative determination of surficial sediment types (as sand, silt, clay, mud). Classification is used in e.g. geotechnical engineering.

Segmentation: Grouping of e.g. traces or areas with similar properties.

---

[1] These definitions are consistent with what was used within ISACS [36].

[2] These are also the parameters we use in our model

Characterization is often considered to be the most accurate of these descriptions; segmentations the least accurate. With the above definition, it would normally be possible to classify the seafloor after a characterization has been done, while the opposite might be more difficult.

The type of identification and choice of utilized processing technique usually depend on the type of instrument to be used. Three main types of instrument are often utilized:

Side-scan sonars: These are often mounted on a towed fish, and give a 2D 'shadow'-image of the seafloor. Common frequencies are 50kHz-500kHz.

Single-beam echosounders: Typical frequencies are 10kHz-150kHz. Fishing echosounders, at typically 38kHz, are very common. So-called sub-bottom profilers are often in the 2kHz-10kHz range, achieving a certain penetration into the sediments (~0-100m). The parametric sonar TOPAS PS040 belongs to this last category.

Multibeam echosounders: These use an array of transducers and beamforming to create several narrow beams along a line perpendicular to the travel path of the vessel. Normal frequencies are 10kHz-300kHz. Multibeam echosounders are commonly used to create bathymetry maps of the seafloor.

Several techniques have been developed for seafloor description. A good overview of the field is given by Lurton [42], covering all three of the above mentioned instrument groups. Other overviews are given by de Moustier [27], concentrating on side-scan and multibeam echosounders, and by Vilming [60], covering multibeam echosounders. In the following, a brief overview of the techniques is given (loosely following [42]).

The use of side-scan sonars for description of the seafloor has essentially been with two different approaches: Texture analysis of the obtained acoustic image utilizing techniques from image processing, and spectral analysis of the measured times signals. One way of spectral analysis was suggested by Pace & Gao [48], using features from the power spectrum of the backscattered signal for classification, essentially by discriminating between the different shapes of power spectra from different seafloors. A promising classification result was obtained.

There has been a large amount of work done in description of the seafloor with multibeam echosounders. Determination of seafloor bathymetry is by far the most common use. The multibeam echosounder might be said to cover the benefits of both single-beam echosounders and sidescan sonars, while having certain benefits in addition. There is one major difference though, multibeam sonars do not usually use as low frequencies as some single-beam echosounders, partially due to size and cost requirements. Several algorithms for segmentation and classification have been developed (less so on characterization), often with techniques from image processing (mainly segmentation of areas and boundary determination). See, e.g., [2], [28], [46]. Backscattering as a function of angle is another approach, first introduced by Jackson *et al.* [38]. Disadvantages are that the analyzed area (e.g. the illuminated beam width) needs to be considered as homogeneous, and there are some ambiguities in the parameter estimation [30]. Kongsberg Simrad AS produces a commercial system for seafloor classification, called Triton. This system uses 5 statistical features for the classification/segmentation, and use a training system to identify new classes.

There are several approaches to analysis and description of the seafloor by single-beam echosounders. The backscatter level is the primary feature that comes to mind. There is however an apparent ambiguity between impedance and roughness (since both affect the amplitude of the scattered signal), which can, in principle, be resolved by looking at the coherent reflection and using information from different frequencies. This was first proposed in 1953 by Eckart [29], and utilized by several others, e.g. Stanton & Clay [55]. This method is only applicable then the RMS roughness is small compared with the incoming wavelength. The parametric sonar seems very suitable for use with this technique, and this is the basis for our work in this report. An important experimental and theoretical work on scattering from a model rough surface using a parametric source was done by Thorne & Pace [57]. The technique has though not yet been taken into general (or commercial) use [42].

Another description approach for use with single-beam echosounders is to utilize the relative levels of the first and second echoes, where the second echo has been scattered twice by the seafloor and once by the sea surface [19]. This method is not dependent upon the use of low frequencies. It has been commercialized for use in classification, under the brand name 'RoxAnn' and produced by Marine Micro System, Aberdeen, Scotland. It is enjoying a certain degree of success. Pouliquen & Lurton [43] used a single-beam echosounder for classification by utilizing the return signal envelopes. The first part of the envelope stems from the vertical reflection and the later part comes from scattering away from vertical, thus the envelope represents in fact the reflection as a function of inclination angle. The results from tests on field data were quite good [42].

The Canadian company Quester Tangent has a classification system called 'QTC View'. It extracts 166 features from the returned echo, and reduces these to 3 features using principal component analysis. Both supervised and unsupervised classification can be done. However, this classification method is based on statistics, which means that physical interpretation of the results are difficult and additional information must be supplied (from the surveyed areas or from a data base) in order to do a classification and not just a segmentation. An advantage with the last three systems described (RoxAnn, Pouliquen & Lurton, QTC View) is that they can be used on relatively inexpensive equipment, e.g. echosounders meant for fisheries (often operating at 38-200kHz). These three systems do classification(/segmentation) with a certain degree of success. However, improvements can be done and a characterization method (instead of classification) may prove even more useful.

1.4 Overview of the thesis

This thesis describes work done to characterize the seafloor by using the parametric sonar TOPAS PS040. Included in the work was verifying the technique and testing it on both synthetic and field data.

To develop a characterization algorithm, a good understanding of the processes involved is necessary. Chapters 2 and 3 help in gaining this understanding, by presenting the background theory and analyzing a monostatic system.

The estimation algorithm itself is presented in Chapter 4, including validation of the implementation on synthetic data. In order to get an understanding of the potentials and limitations of the technique, both analytical and numerical sensitivity analysis has been done (Chapter 5). This study also aided in the development of the technique. The real test of an algorithm for analysis of the real seafloor needs to be on field data. This was done for different types of seafloor, from areas in the Baltic, North Sea and the Mediterranean (Chapter 6).

The contents of the thesis is summarized as:

Chapter 2. Theoretical background This chapter gives the theoretical background for the rest of the thesis. Scattering from rough surfaces is the main part. Definition of predefined seafloor classes is done.

Chapter 3. Description and analysis of a monostatic sonar system This chapter analyze a monostatic sonar system and identify the main processes, as well as estimate the importance of these processes. It also discuss scattering from seafloor volume and surface as a function of time and beam width.

Chapter 4. Estimation of seafloor parameters The estimation technique is described in this chapter, including some details of the implemented algorithm. Validation of the algorithm on synthetic data is presented.

Chapter 5. Sensitivity analysis A numerical sensitivity analysis of the model parameters is done in this chapter, with references to analytical sensitivity analysis done in Chapter 2.

Chapter 6. Analysis of field data This chapter is devoted to analyzing field data from different seafloors, using the developed algorithms. Areas in the Mediterranean, North Sea and Baltic have been analyzed, and comparisons have been done with ground truth data and other seafloor information (divers impressions etc.), as well as results from the characterization method sirOb.

Chapter 2

Theoretical background

This chapter presents theoretical background that will be used in the rest of the thesis. Only the theory relevant for this work is included, as underwater acoustics is well presented in standard textbooks (see, e.g., [26], [59]).

Transmission of sound over a limited range, and mostly near-vertical, is relevant for monostatic sonars used for characterization of the seafloor. This also includes attenuation in the water column and sediment, as well as ray bending. Scattering at rough surfaces is a very important item, which will be introduced by looking at scattering at a flat interface (the results will also be used in the estimation technique). Results from this chapter on theory will mainly be used in Chapter 3, where a monostatic sonar system is analyzed, and in Chapter 4 where the developed estimation technique is presented.

2.1 Reflection and transmission at a fluid-fluid interface

As a background for the more relevant model, we start with the simplest example. The seafloor is yet treated as a flat interface, and reflection- and transmission coefficients be calculated. A rough seafloor (compared to the acoustic wavelength) will modify the following equations, as described in Sec. 2.4. The following derivation mainly follows [39].

We first assume that the seafloor can be treated as a fluid. This is a valid approximation if the seafloor consists of a sediment that is not too rigid. We consider an incident plane wave with an angle relative to the z-direction of θ_i

(i is 0 in the water, 1 in the sediment). The geometry is illustrated in Fig. 2.1. The acoustic pressures can then be written as

$$p_i = \exp\left[ik_0(x\sin\theta_0 + z\cos\theta_0)\right] \tag{2.1}$$

$$p_r = \mathcal{R}\cdot\exp\left[ik_0(x\sin\theta_0 - z\cos\theta_0)\right] \tag{2.2}$$

$$p_t = \mathcal{T}\cdot\exp\left[ik_1(x\sin\theta_1 + z\cos\theta_1)\right] \tag{2.3}$$

where p_i, p_r, p_t are the incident, reflected and transmitted pressures, respectively, $\mathcal{R}$ the reflection coefficient and $\mathcal{T}$ the transmission coefficient.

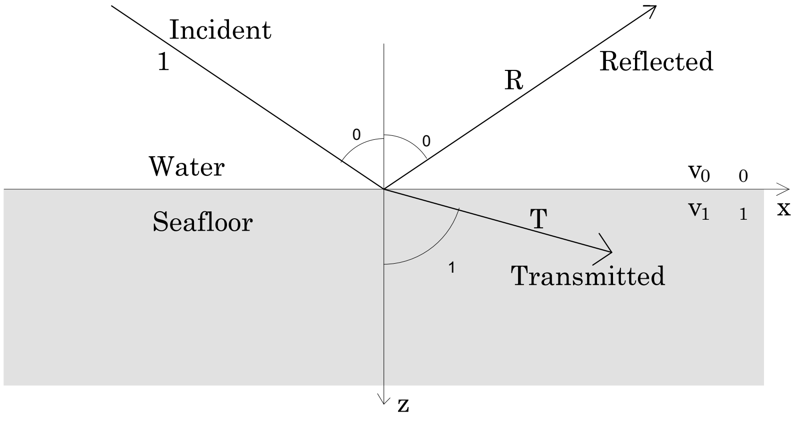

Figure 2.1: *Geometry for reflection and transmission at an interface.*

The boundary conditions at the surface requires continuity of pressure and vertical particle velocity across the surface. This can be written as

$$p_0 = p_1, \qquad \frac{1}{iw\rho_0}\cdot\frac{\partial p_0}{\partial z} = \frac{1}{iw\rho_1}\cdot\frac{\partial p_1}{\partial z} \tag{2.4}$$

The boundary condition of continuity of pressure leads to *Snell's law of refraction*, which can be written as

$$k_0\sin\theta_0 = k_1\sin\theta_1 \tag{2.5}$$

Using Eqs. (2.1)-(2.4), the reflection and transmission coefficients are found to be

$$\mathcal{R}_{01} = \frac{Z_1 - Z_0}{Z_1 + Z_0}, \qquad \mathcal{T}_{01} = \frac{2Z_1}{Z_1 + Z_0} \tag{2.6}$$

where $Z_i \equiv \rho_i c_i / \cos\theta_i$ is the acoustic impedance in the vertical direction and $\rho_i c_i$ is the specific acoustic impedance. The impedance Z_i can be replaced with a slightly more complicated impedance expression in order to incorporate the effect of shear waves ([39]). An illustration of the relation between impedance of a sediment and the reflection coefficient is shown in Fig. 2.2.

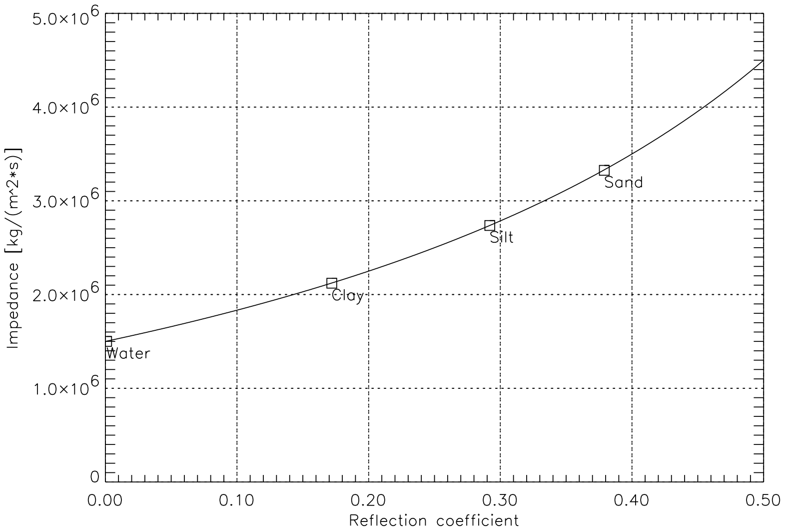

Figure 2.2: *Impedance of a sediment (with sea water on top), as a function of the reflection coefficient. Some typical values for specific acoustic impedance are included for reference.*

2.2 Attenuation of sound in sea water

Sound propagating in sea water is continuously attenuated. This is partly due to acoustic energy being transformed into heat and partly due to scattering by different kinds of inhomogeneities ([39]). This attenuation is highly frequency and salinity dependent, and is also somewhat dependent upon temperature, pressure and acidity. The following empiric formula ([39], [58]) is however considered sufficiently accurate for most ocean underwater applications.

$$\alpha \simeq 3.3 \cdot 10^{-6} + \frac{1.1 \cdot 10^{-4} f^2}{1 + f^2} + \frac{4.4 \cdot 10^{-2} f^2}{4100 + f^2} + 3.0 \cdot 10^{-7} f^2 \qquad (2.7)$$

where α is in dB/m and the frequency f is in kHz. The formula applies for a salinity of 35ppt, a temperature of 4°, pH of 8.0 and depth of about 1000m. The attenuation is illustrated in Fig. 2.3. Shear and volume viscosity is the reason for attenuation in fresh water. Due to different relaxation processes, the attenuation in sea water is considerably higher than that of fresh water. The relaxation processes are mainly with boric acid ($B(OH)_3$) and magnesium sulphate ($MgSO_4$), parts 2 and 3 of Eq. (2.7).

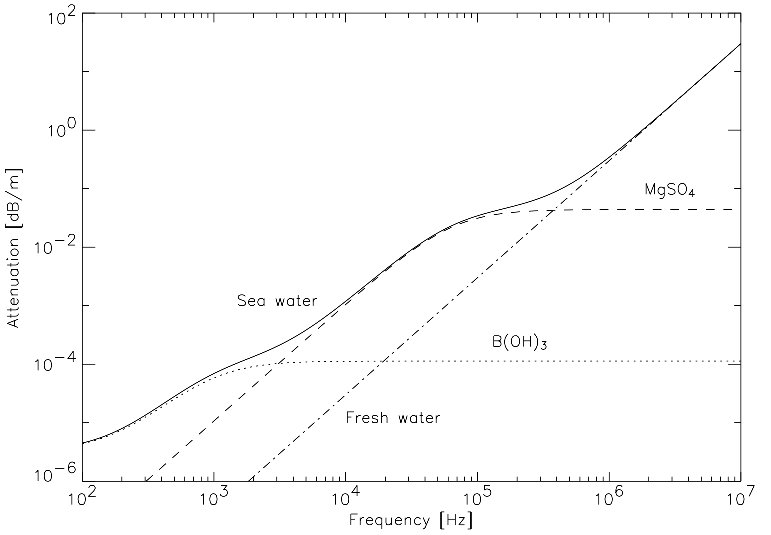

Figure 2.3: *Attenuation in sea water, as a function of frequency. The attenuation in fresh water is also shown, as well as the contributions from the relaxation processes of boric acid (*$B(OH)_3$*) and magnesium sulphate (*$MgSO_4$*).*

Example: For a transmission range of 200m, the attenuation will be about [0.014, 0.24, 0.83, 6.9, 69]dB for the frequencies [1, 10, 20, 100, 1000]kHz. The parametric sonar used in this study has a maximum frequency of less than 20kHz, and thus for this instrument the attenuation in sea water can be neglected for shallow waters.

2.3 Bottom loss

Sound waves in a solid can propagate as compressional and/or shear waves. Sediments are often modeled as fluids, which do not support shear waves. This is often a good approximation as the rigidity of sediments is often low. The ocean basement on the other hand, consisting of rocks like chalk, limestone or basalt, should be modeled as an elastic medium, supporting shear waves.

The wave attenuation in bottom materials is three-to-four orders of magnitude larger than that of sea water ([39]), and is usually considered to be proportional to frequency. It is therefore often given with the dimension of dB per wavelength, and typical values can be 0.1-1dB/λ_p, where λ_p denotes the compressional wavelength.

Example: A sediment attenuation coefficient of $0.5dB/\lambda_p$ and a sound speed of 1700m/s will give an attenuation of about [0.29, 2.9, 5.9, 29.4, 294.1]dB/m for the frequencies [1, 10, 20, 100, 1000]kHz. The parametric sonar used in this study has a frequency range of about 2-15kHz, and the sediment attenuation is thus significant even for a fairly short penetration into the volume.

From the example above it is clear that for obtaining any significant penetration into seafloor sediments one needs to use a fairly low-frequency sonar. The attenuation in a sediment can in principle be found by either looking at the signal strength as a function of penetration into the volume or by looking at the relation between high- and low-frequency content in the signal as a function of penetration depth (using the fact that the attenuation is proportional to frequency).

Strong additional scatterers in the sediments, as e.g. gas bubbles, are not considered in the above discussion on attenuation. Such scatterers may give a very strong reflection and significantly reduce the energy penetrating further into the sediment. This may be seen when e.g. using sub-bottom profilers on a gassy seabed. A strong reflection is obtained from the layer containing gas, and very little signal from the underlying sediments.

2.4 Scattering at rough surfaces

A rough surface, e.g. the seafloor, will lead to imperfect reflection and partial scattering of incident acoustic or electromagnetic wave fields. The main effects of scattering at rough surfaces depend on the RMS roughness compared to the wavelength of the incident wave field. Thus, a surface may look reasonably smooth when probing it with a long wavelength signal and very rough when the signal has a short wavelength. The incidence and reflection angles do also contribute. The Rayleigh criterion is a measure of this 'apparent roughness', and will be described below.

A theoretical description of the scattering at rough surfaces is necessary in order to understand and being able to model the influence of the roughness on a signal. Different approaches may be used. Theoretical work may be divided into two categories([47]): 1) Approximate but tractable, such as perturbation theory and Kirchhoff theory, or 2) more rigorous but predominantly formal. Examples of the last category are integral equation techniques, variational methods and Green's function approaches.

In the development of characterization techniques, theory from the first category seems most appropriate, assuming a sufficient accuracy can be obtained. The Kirchhoff theory is the most widely used theory in the study of scattering from rough surfaces, due to understandability and its practical usefulness. It will be described following [47].

2.4.1 The Rayleigh criterion

The scattered signal from a rough surface is dependent upon the surface roughness as well as the incident wave length and inclination angles. Simple considerations of phase differences between two parallel rays scattered on a rough surface ([47, page 3]) lead to the so-called *Rayleigh criterion* for determining the degree of roughness of a surface. The Rayleigh criterion is a measure of the 'apparent roughness', as seen by the incident acoustic field.

For specular scattering the phase difference becomes

$$\Delta\phi = 2k\Delta h \cos\theta_1$$

where k is the wave number of the incoming wave field, Δh is the height difference between the points where the rays hit the surface and θ_1 the incident angle (relative to vertical). The interference between the rays depends on the magnitude of the phase difference compared with π. The Rayleigh criterion states that if $\Delta\phi < \pi/2$ then the surface is 'smooth', otherwise is is 'rough'. For a surface this expression may be averaged and Δh be replaced by σ, the surface RMS deviation from smooth. The criterion (for 'smoothness') then becomes

$$R_a < \frac{\pi}{4} \tag{2.8}$$

where the *Rayleigh parameter* R_a is given by $R_a = k\sigma\cos\theta_1$, and θ_1 is the angle relative to the z-direction of the incident wave.

The RMS roughness σ is defined as

$$\sigma = \sqrt{\langle h^2 \rangle_s}$$

where $h(\mathbf{r})$ is the local surface height and it is assumed that $\langle h \rangle_s = 0$

Example: For frequencies of e.g. 1kHz, 5kHz, 10kHz, 100kHz, and normal incidence the Rayleigh criterion for 'smoothness' will be $\sigma <$ 19cm, 3.75cm, 1.9cm, 0.19cm, respectively.

2.4.2 Coherent and diffuse fields

From the Rayleigh criterion (Sec. 2.4.1) we have that the 'apparent roughness' of a surface is also dependent upon frequency and angle of the incident wave. Short incident wavelengths and small incidence angles make surfaces look more rough.

The 'apparent roughness' determines the field scattered from the surface. For a smooth surface (i.e. low 'apparent roughness') we get coherent scattering in the specular direction only (for an infinite extent surface; finite extent leads to scattering also around the specular direction), while a rougher surface has less of the specular scattering and more scattering away from the specular direction, called diffuse (or incoherent) scattering. This is illustrated in Fig. 2.4.

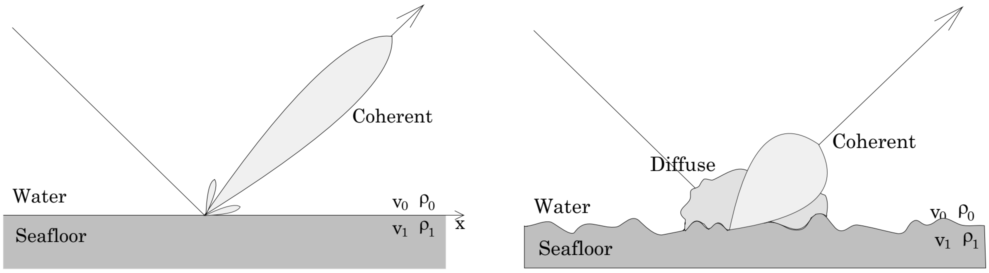

Figure 2.4: *Scattering at smooth and rough surfaces. At a rough surface, the coherent scattering is reduced and we get diffuse, or incoherent, scattering.*

When averaging fields from many different randomly rough surfaces ('stacking') the diffuse (incoherent) field will be reduced, due to random phase, while the coherent field is retained. The diffuse field may however be maintained by averaging the field intensity, thus neglecting phase information. Stacking requires careful alignment of the traces to reduce phase errors; see Sec. 4.2.1.

2.4.3 Description of rough surfaces

In order to be able to formulate theories for scattering of rough surfaces, a description of the surface is needed. This section briefly treats different ways of describing the properties of a rough surface. The treatment mainly follows Ogilvy [47].

We are mostly concerned about random rough surfaces, as e.g. the sea surface and, for the most part, the seafloor surface. Such surfaces must be described statistically, and the description must, in one way or another, contain:

- The height distribution, often referred to a reference surface (as e.g. a smooth seafloor)
- Variation of the heights along the surface. This can be described by e.g. correlation functions or structure functions.

Description of rough surfaces by height distributions and correlation functions

The height distribution, $p(h)$, describes the distribution of $h(\mathbf{r})$, the deviation from a smooth surface. The direction to a given point is $\mathbf{r}$. $\mathbf{R}$ will later be used to denote another similar point[1]. The height distribution is often considered to be Gaussian, with probability density

$$p(h) = \frac{1}{\sigma\sqrt{2\pi}} \exp\left(-\frac{h^2}{2\sigma^2}\right) \tag{2.9}$$

This is often considered a good assumption for surfaces made by natural processes (such as the seafloor surface), although other distributions are sometimes considered better.

The Fourier transform of the probability density function of a rough surface is called the one-dimensional characteristic function:

$$\chi(s) = \int_{-\infty}^{\infty} p(h) e^{\mathrm{i}sh} \mathrm{d}h \tag{2.10}$$

It provides a measure of the phase modulation of a wave at a rough surface ([47]), but contains no more information than $p(h)$.

---

[1] Vectors are shown in **bold**, lengths are shown in *slanted* fonts.

The variation of heights along the surface may be specified by correlation functions, defined as

$$C(\mathbf{R}) = \frac{\langle h(\mathbf{r})h(\mathbf{r}+\mathbf{R})\rangle_s}{\sigma^2} \tag{2.11}$$

Such correlation functions often include a correlation length, λ_0, that says something about over which length scale height changes occur along the surface ([47]). Most correlation functions decay to zero as $\mathbf{R}$ increases. This is only correct for truly random surfaces. For isotropic surfaces[2], Gaussian correlation functions are often assumed:

$$C(R) = \exp\left(-\frac{R^2}{\lambda_0^2}\right) \tag{2.12}$$

Exponential correlation functions are also used, and are often found to give a better fit to experimental data ([32], [51], [61]):

$$C(R) = \exp\left(-\frac{|R|}{\lambda_0}\right) \tag{2.13}$$

Other correlation functions are also used, as e.g. combining a Gaussian form near the origin but changing to an exponential shape for large R.

An alternative to the correlation function is the surface structure function, which is formally equivalent to the correlation function for stationary surfaces, but is independent of the reference surface from which the heights $h(\mathbf{r})$ are measured. See, e.g., [56] for a description of correlation functions.

Description of rough surfaces by power spectra

Another way of specifying a rough surface is by using a power spectrum. The power spectrum does in fact both specify the height distribution and the variation along the surface. It is usually defined as the Fourier transform of the un-normalized correlation function ([47]):

$$P(\mathbf{k}) = \frac{\sigma^2}{(2\pi)^2}\int_{-\infty}^{\infty} C(\mathbf{R})e^{\mathrm{i}\mathbf{k}\cdot\mathbf{R}}\mathrm{d}\mathbf{R} \tag{2.14}$$

The RMS roughness is found to be

$$\sigma = \sqrt{\int_{-\infty}^{\infty} P(\mathbf{k})\mathrm{d}\mathbf{k}} \tag{2.15}$$

---

[2] The properties of an isotropic surface is not dependent upon direction

The power spectrum for a surface with a Gaussian correlation function and a correlation length of λ_0 will itself be Gaussian with a standard deviation of $\sqrt{2}/\lambda_0$. A surface with an exponential correlation function will have a power spectrum in the form of a Lorentzian function, which is crudely similar to a Gaussian shape but has a longer tail, indicating higher frequency components.

Description of rough surfaces by fractal theory

Surfaces can also be described by fractals. Mandelbrot ([44]) defined a fractal to be any curve or surface that is independent of scale (self-similarity). A coast-line can be considered a fractal; its length is dependent upon the scale of the measurements (by using a larger scale map the length would appear longer, and by measuring in the real world it would appear even longer when all the small fjords etc. are included). A rough curve does seem to cover a two-dimensional area, and the rougher the curve the more area it seems to cover. Thus, this fractal curve is said to have a dimension between 1 and 2; not being a straight line but not covering completely an area either. It is similar for a rough surface; it is said to have a dimension between 2 and 3.

Fractal surfaces can be described by using a power spectrum. It may be written as

$$P(k) \sim \frac{1}{k^{\nu'}} \tag{2.16}$$

The dimensionality of such a surface is given by

$$D = \frac{(5-\nu')}{2} \tag{2.17}$$

so that $1 < \nu' < 3$. We also use another notation in this report, $\nu = \nu' + 1$. This is consistent with the notation of the numerical model BORIS.

In practice, to avoid infinite height correlation functions and RMS roughness when using a power spectrum as in Eq. (2.16), a band-pass filter is often applied: $k_1 < k < k_2$. This is also consistent with measuring technique. The longest wavelength that can be determined by a given measuring technique is dependent upon the sample length (or area) used. The shortest wavelength is determined by both the sampling interval and the instrument resolution (or, in the case of acoustic sampling, the probing wavelength).

The numerical model BORIS uses a power spectrum similar to Eq. (2.16) for describing the rough seafloor surface (see Sec. 2.5).

2.4.4 Kirchhoff theory for scattering at rough surfaces

The Kirchhoff theory, also known as the tangent-plane or physical optics theory, is the most used theory in the study of scattering from rough surfaces. It has an easily understandable physical basis and leads to relatively simple analytical expressions for scattered field amplitudes. Unfortunately, its accuracy is not easily quantifiable.

The theory is based on the Kirchhoff or tangent plane approximation, treating each point on the surface as a part of an infinite plane, parallel to the local surface tangent. Multiple scattering and shadowing are normally ignored, the far field approximation is used and the reflection coefficient is assumed to be constant along the surface. This is further described later in this section.

The accuracy of the Kirchhoff approximation is usually said to be dependent primarily upon the ratio λ_0/λ, but also λ_0/σ, which both should be above unity (see, e.g., [47]). λ_0 is the correlation length of the surface, λ the wave-length of the acoustic signal and σ the RMS roughness of the surface. Essentially this means that the wave length of the incoming field must be smaller than the surface correlation length and that the surface must be sufficiently smooth (i.e. the surface radius of curvature must not be too small). It is however not quite correct to say that the Kirchhoff approximation is a high frequency approximation. It is limited by the local surface approximation, which improves with higher frequencies, but is also limited by global effects across the surface (multiple scattering and shadowing), which are often more dominant with increasing frequency (or surface roughness).

Angles of incidence must be small enough to ensure that grazing of the surface does not occur. For e.g. exponential correlation functions, containing more high-frequency roughness than Gaussian correlation functions, the regimes of validity might be lower.

Basic Kirchhoff theory

The following gives a brief presentation of the Kirchhoff theory. It mainly follows Ogilvy [47]. The theory, as presented here, may be used on either acoustic or electromagnetic waves, as long as there is no coupling between different wave polarisations. This section covers the basic formulation of Kirchhoff theory and determination of moments of the scattered field, which gives information about the coherent and diffuse scattered field.

The total field ψ at a point $\mathbf{r}$ is described as the sum of the incoming field, ψ^{inc}, and scattered field, ψ^{sc}.

$$\psi(\mathbf{r}) = \psi^{inc}(\mathbf{r}) + \psi^{sc}(\mathbf{r}) \tag{2.18}$$

The total field at any point is given by the Helmholtz interior or exterior scattering formula (see, e.g., [49]), assuming the surface S_0 (with surface normal $\mathbf{n}_0$) is closed[3]

$$\psi(\mathbf{r}) = \psi^{inc}(\mathbf{r}) + \int_{S_0} \left[\psi^{sc}(\mathbf{r}_0) \frac{\partial G(\mathbf{r},\mathbf{r}_0)}{\partial n_0} - G(\mathbf{r},\mathbf{r}_0) \frac{\partial \psi^{sc}(\mathbf{r}_0)}{\partial n_0} \right] \mathrm{d}\mathbf{S}_0 \tag{2.19}$$

The full-space Greens function (normally used for scattering from surfaces of finite dimensions) is given by

$$G(\mathbf{r},\mathbf{r_o}) = \frac{\exp(\mathrm{i}k|\mathbf{r}-\mathbf{r_o}|)}{4\pi|\mathbf{r}-\mathbf{r_o}|} \tag{2.20}$$

where $\mathbf{r}_0$ is on the scatterer and $\mathbf{r}$ some distance away.

The scattered field $\psi^{sc}(\mathbf{r}_0)$ within Eq. (2.19) is interchangeable with the total field, $\psi(\mathbf{r}_0)$, as long as the surface S_0 is closed. Using Eq. (2.19), and following [5], the field scattered from the surface can therefore be written as

$$\begin{aligned} \psi^{sc}(\mathbf{r}) &= \psi(\mathbf{r}) - \psi^{inc}(\mathbf{r}) \\ &= \int_{S_0} \left[\psi(\mathbf{r}_0) \frac{\partial G(\mathbf{r},\mathbf{r}_0)}{\partial n_0} - G(\mathbf{r},\mathbf{r}_0) \frac{\partial \psi(\mathbf{r}_0)}{\partial n_0} \right] \mathrm{d}\mathbf{S}_0 \end{aligned} \tag{2.21}$$

The field ψ and its derivative on the surface are the only unknown parameters in Eq. (2.21). The Kirchhoff approximation is used for the field

$$\psi(\mathbf{r}_0) = [1 + \mathcal{R}(\mathbf{r}_0)]\, \psi^{inc}(\mathbf{r}_0) \tag{2.22}$$

where $\mathcal{R}$ is the reflection coefficient for plane waves incident onto a plane surface (Eq. (2.6)). Assuming a monochromatic incoming wave, $\psi^{inc}(\mathbf{r}) = \exp(\mathrm{i}\mathbf{k}_{inc} \cdot \mathbf{r})$, the derivative of the field can be found ([47]) to be

$$\frac{\partial \psi(\mathbf{r}_0)}{\partial n} = \mathrm{i}[1 - \mathcal{R}(\mathbf{r}_0)](\mathbf{k}_{inc} \cdot \mathbf{n}_0)\psi^{inc}(\mathbf{r}_0) \tag{2.23}$$

---

[3] The surface may always be closed for mathematical purposes.

A finite surface is assumed. The far-field approximation, $r \gg r_0$, is then applied. The integration over the rough surface S_0 is then converted to an integration over the mean plane of the surface, S_M (see [47]).

Equation (2.21) can then be written in the general form

$$\begin{aligned}\psi^{sc}(\mathbf{r}) &= \frac{\mathrm{i}k\mathrm{e}^{\mathrm{i}kr}}{4\pi r}\int_{S_M}(a\partial h/\partial x_0 + b\partial h/\partial y_0 - cc) \\ &\quad \times \exp\{\mathrm{i}k[Ax_0 + By_0 + Ch(x_0,y_0)]\}\mathrm{d}x_0\mathrm{d}y_0 \qquad (2.24)\end{aligned}$$

where the constants A, B and C are given by the x, y and z components of the change of the unit wavevector:

$$\begin{aligned}A &= \hat{k}_x^- = \sin\theta_1 - \sin\theta_2\cos\theta_3 \\ B &= \hat{k}_y^- = -\sin\theta_2\sin\theta_3 \qquad (2.25)\\ C &= \hat{k}_z^- = -(\cos\theta_1 + \cos\theta_2)\end{aligned}$$

and the constants a, b and cc are given by

$$\begin{aligned}a &= (\hat{k}^+ - \mathcal{R}\hat{k}^-)_x = \sin\theta_1(1-\mathcal{R}) + \sin\theta_2\cos\theta_3(1+\mathcal{R}) \\ b &= (\hat{k}^+ - \mathcal{R}\hat{k}^-)_y = \sin\theta_2\sin\theta_3(1+\mathcal{R}) \qquad (2.26)\\ cc &= (\hat{k}^+ - \mathcal{R}\hat{k}^-)_z = \cos\theta_2(1+\mathcal{R}) - \cos\theta_1(1-\mathcal{R})\end{aligned}$$

and the angles θ_1, θ_2 and θ_3 are defined as follows: θ_1 is incident angle, relative to z direction; θ_2 is scattered angle, relative to z direction; θ_3 is scattered angle, out of the plane of incidence. The surface is defined to extend over $-X \leq x_0 \leq X$, $-Y \leq y_0 \leq Y$.

Equation (2.24) is the general result arising from applying Kirchhoff theory to scalar wave scattering from rough surfaces. The assumptions taken, in addition to the Kirchhoff approximation, are observations in the far-field, harmonic and planar incoming wave, no points of the surface have infinite gradient.

It is interesting to note the physical interpretation of Eq. (2.24): The integration is done over spherically spreading secondary 'sources' covering the surface. Each of these sources has an amplitude determined by the local surface gradient and a phase determined by the local surface height. It is also worth noticing that diffraction effects, which occur when integrating over a finite area, are not explicitly included in the expressions.

Equation (2.24) is not easy to further analyze analytically. The next step is therefore to assume constant reflection coefficient ($\mathcal{R}$) along the surface. This is reasonable when the scattered surface divides two regions of very different acoustic (or dielectric) properties, or/and the surface gradients are very small ([47]), or/and $\mathcal{R}$ is constant or varies slowly over the surface element (particularly true near vertical incidence) ([45]). The dependence of surface gradients is then removed from the equation.

The general result for the scattered field is then found to be given by

$$\psi^{sc}(\mathbf{r}) = \frac{-\mathrm{i}ke^{\mathrm{i}kr}}{4\pi r} 2F(\theta_1, \theta_2, \theta_3) \int_{S_M} \exp\left\{\mathrm{i}k\phi(x_0, y_0)\right\} \mathrm{d}x_0 \mathrm{d}y_0 + \psi_e \tag{2.27}$$

where the phase function $\phi(x_0, y_0)$ is given by

$$\phi(x_0, y_0) = Ax_0 + By_0 + Ch(x_0, y_0) \tag{2.28}$$

the angular factor $F(\theta_1, \theta_2, \theta_3)$ is given by

$$F(\theta_1, \theta_2, \theta_3) = \frac{1}{2}\left(\frac{Aa}{C} + \frac{Bb}{C} + cc\right)$$

and the 'edge effects' ψ_e are given by

$$\begin{aligned} \psi_e \quad = \quad & \frac{-\mathrm{i}k\mathrm{e}^{\mathrm{i}kr}}{4\pi r}\left[\frac{\mathrm{i}a}{kC}\int\left(\exp\left\{\mathrm{i}k\phi(X, y_0)\right\} - \exp\left\{\mathrm{i}k\phi(-X, y_0)\right\}\right)\mathrm{d}y_0\right. \\ & \left. + \frac{\mathrm{i}b}{kC}\int\left(\exp\left\{\mathrm{i}k\phi(x_0, Y)\right\} - \exp\left\{\mathrm{i}k\phi(x_0, -Y)\right\}\right)\mathrm{d}x_0\right] \end{aligned} \tag{2.29}$$

In practice the 'edge effects' are only negligible close to specular direction ([47]), for other directions they must be included.

Equation (2.27) is extensively used in the literature on problems of wave scattering from rough surfaces. The assumptions made are repeated below[4]:

1. Kirchhoff theory is a valid approximation for the scattering.
2. Observation in the far field.
3. Planar and monochromatic incident wave.
4. No points on the surface has infinite gradient.
5. The reflection coefficient is constant across the surface.

---

[4] The first four assumptions where taken to obtain Eq. (2.24).

Moments of the scattered field, general roughness

In this section, the amplitude and intensity of the scattered field are determined. This provides information about both the coherent and the diffuse field.

The average amplitude of the field contains only the coherent field, as the diffuse field has random phase. Using Eq. (2.27), the following expression may be obtained

$$\begin{aligned} \langle \psi^{sc} \rangle &= \frac{-\mathrm{i}k\mathrm{e}^{\mathrm{i}kr}}{4\pi r} A_M \, c\, \chi(kC) \left(\frac{\sin kAX}{kAX} \right) \left(\frac{\sin kBY}{kBY} \right) \\ &= \chi(kC) \psi_0^{sc} \end{aligned} \tag{2.30}$$

where ψ_0^{sc} is the scattered field from the surface if it was perfectly flat. c is the sound speed. $\chi(kC)$ is the one-dimensional characteristic function of the surface, where k is the wave number of the incident acoustic wave and $C = -(\cos\theta_1 + \cos\theta_2)$, where θ_1 and θ_2 are incident and scattered angles relative to the z-direction, respectively. The function $\chi(kC)$ is the Fourier transform of the height probability density function of the surface. A_M is the area of the mean plane of the surface, and the rough surface has been assumed to be rectangular with $-X \leq x_0 \leq X$, $-Y \leq y_0 \leq Y$.

The mean intensity of the diffuse scattered field[5] may (from Eq. (2.27)) be found to be

$$\begin{aligned} \langle I_d \rangle &= \frac{k^2 F^2}{2\pi r^2} A_M \int_0^\infty J_0 \left(kR\sqrt{A^2 + B^2} \right) \\ &\quad \times \left[\chi_2(kC_1 - kC_1 R) - \chi(kC)\bar{\chi}(kC) \right] RdR \end{aligned} \tag{2.31}$$

where $J_0(x)$ is the zeroth-order Bessel function of the first kind and $\chi_2(s_1, s_2, R)$ is the two-dimensional characteristic function. $F(\theta_1, \theta_2, \theta_3)$ is given in Eq. (2.27) and the constants a, b, c, A, B and C are given in Eq. (2.25) and Eq. (2.26).

Some further assumptions, in addition to those mentioned in the previous section, have been made in order to obtain Eq. 2.31:

6. The surface dimensions are much greater than the correlation length of the surface

7. The surface statistics are isotropic (direction-independent; making possible the conversion to spherical coordinates for the surface integration).

---

[5] The diffuse field amplitude averages to zero, thus the mean intensity must be considered

8. The 'edge effects' may be approximated by their non-stochastic values, thus giving no contribution to the diffuse field.

Moments of the scattered field, Gaussian roughness

When the surface has Gaussian roughness, and since the characteristic function is analytic, analytic expressions for the moments of the scattered field (Eq. (2.30) and (2.31)) may be found. The coherent scattered field for a harmonic incident wave is then

$$\langle \psi^{sc} \rangle = \psi_0^{sc} \chi(kC) = \psi_0^{sc} e^{-g/2} \tag{2.32}$$

where

$$g = k^2 \sigma^2 \left(\cos\theta_1 + \cos\theta_2\right)^2 \tag{2.33}$$

The coherent scattered field from a rough surface is thus given as the scattered field from a similar smooth surface, ψ_0^{sc} , multiplied with a factor $e^{-g/2}$. The factor g contains the RMS roughness σ, the wave number k, and incident and reflected angles, θ_1, θ_2.

In this expression, the effects of the impedance and roughness are separated. ψ_0^{sc} is dependent upon the acoustic impedance while the exponential term is dependent upon the surface roughness. This is essential for the estimation technique (which is described in Chapter 4).

These expressions were first published in 1953, by Eckart ([29]) and Ament ([1]), for respectively acoustic and electromagnetic waves.

Equation (2.31) gives the expression for the mean intensity of the diffuse field. The two-dimensional characteristic function for a Gaussian surface is ([47]) given by

$$\chi_2(kC, -kC, R) = \exp(-k^2 C^2 \sigma^2 [1 - C(R)]) \tag{2.34}$$

The surface correlation function $C(R)$ is assumed to be Gaussian

$$C(R) = e^{-R^2/\lambda_0^2} \tag{2.35}$$

The average diffuse field intensity for a harmonic incident wave and a Gaussian surface is then (by using Eq. (2.31)) given by

$$\langle I_d \rangle = \frac{k^2 F^2 \lambda_0^2 e^{-g}}{4\pi r^2} A_M \sum_{n=1}^{\infty} \frac{g^n}{n!n} \exp\left(-\frac{k^2 (A^2 + B^2) \lambda_0^2}{4n}\right) \tag{2.36}$$

The diffuse field thus depends on σ, k, θ_1, θ_2, θ_3, A_M, as the coherent field, but also on λ_0, the surface correlation length.

The intensity of the total field can ([47]) be written as

$$\langle I \rangle = I_0 e^{-g} + \langle I_d \rangle \tag{2.37}$$

where I_0 is the energy scattered from a smooth surface and $\langle I_d \rangle$ is given by Eq. (2.36). One additional assumption has been taken:

9. The surface has a Gaussian height distribution and a Gaussian correlation function.

For a multi-frequency or broad-band wave field we need to generalize the given equations. For the coherent scattering we get the following expression (by using Eq. (2.32))

$$\langle \psi^{sc}(\sigma) \rangle = \int_{f=0}^{\infty} \psi_0^{sc}(f) \cdot e^{-g(f,\sigma)/2} df \tag{2.38}$$

The same generalization may be done with Eq. (2.36), to obtain the diffuse field.

Example: For normal incidence backscattering, the exponential factor in Eq. 2.32 will be $exp\left\{-2 \cdot k^2\sigma^2\right\}$. Figure 2.5 shows the exponential term as a function of signal frequency and for different values of the seafloor roughness. As seen in the figure, the coherent field as a function of frequency can be used to estimate the roughness σ when the roughness is not too large in comparison with the transmitted signal wavelength.

2.4.5 Potential for characterization

The previous sections reveal some interesting possibilities for characterization.

A rough seafloor leads to a lower coherently scattered amplitude, as shown. A lower impedance contrast between the water and sediment have the same effect, lowering the amplitude. This looks like a ambiguity between roughness and impedance estimation. However, this may be solved by using the fact that a rough surface looks less rough for lower frequencies, and vice versa, as shown in Eq. (2.38). We notice that for a broad-band pulse a change in the

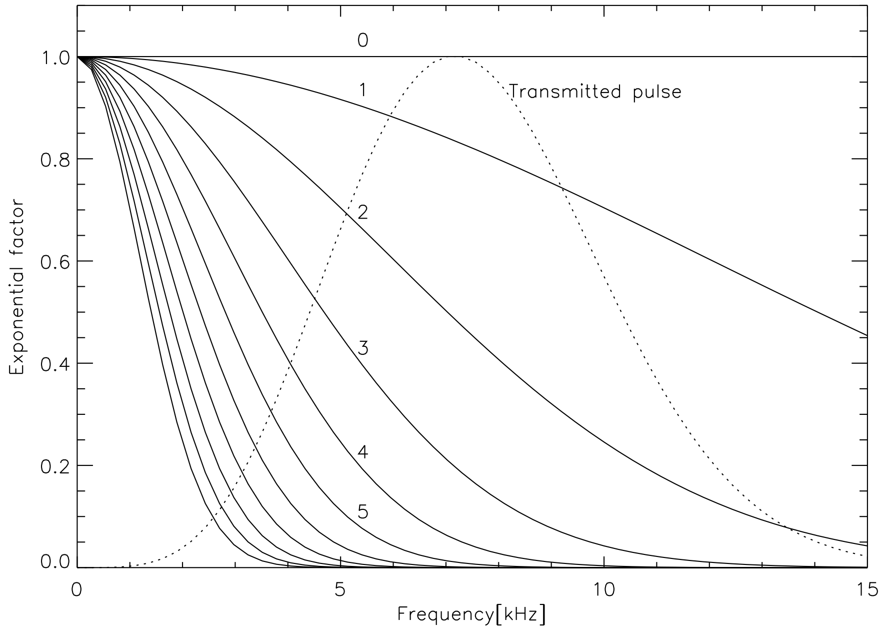

Figure 2.5: *The value of the factor exp* $\left\{-2 \cdot k^2\sigma^2\right\}$*, as a function of frequency, for different values of* σ*. This factor equals* $\langle\psi^{sc}\rangle/\psi_0^{sc}$*, for normal incidence backscattering. The values of* σ *are 0 to 10cm, in steps of 1cm (some of them are labeled in the plot). The power spectrum of a typical transmitted pulse (TOPAS@8kHz) is included for reference.*

roughness will give an apparent frequency shift in the data, and also influence the amplitude and thereby energy. A change in the impedance will only affect the signal amplitude and energy.

From the treatment of Kirchhoff theory, some potential approaches seem suitable for characterization of the seafloor:

1. Using the frequency-shift of the average coherent signal for finding the RMS roughness σ. After the roughness is estimated, the impedance can be estimated by using the energy and the roughness estimate, Eq. (2.38).
2. Using the average diffuse field dependency of the product $\lambda_0^2 e^{-g}$ for finding λ_0, after σ has been found by the method described above.

The first approach, using the coherently scattered signal to estimate seafloor roughness and impedance, is the basis of the estimation method presented in Chapter 4 of this report.

The effect of roughness is illustrated in Figs. 2.6 and 2.7. A harmonic source and normal incidence backscattering are assumed.

Figure 2.6 shows the amplitude of a signal backscattered from a rough seafloor, as a function of RMS roughness divided by the incoming wavelength. As seen, the amplitude decreases significantly even at a moderate roughness-to-wavelength ratio. Thus even a low roughness can highly influence the backscattering process.

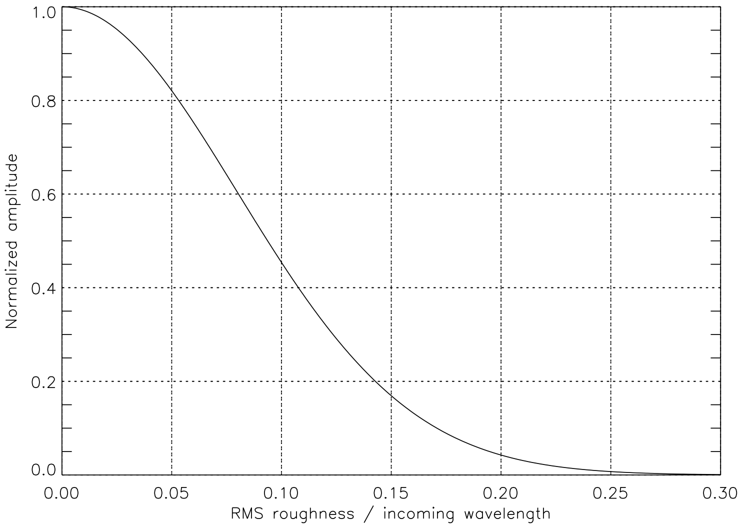

Figure 2.6: *Normalized backscattered amplitude from a rough seafloor, as a function of RMS roughness divided by the incoming wavelength. Normal incidence is assumed.*

Figure 2.7 shows the estimated impedance, based only on received energy and not corrected for roughness, as a function of RMS roughness divided by the incoming wavelength. The calculation is based on reflection from a smooth interface (Sec. 2.1) and only coherent reflection is included. Not correcting for roughness leads to an underestimated impedance. As seen, correcting for roughness is important even at low roughness, in order to get a good impedance estimate. Without roughness correction, an RMS roughness of only 10% of the incoming wavelength will lead to an impedance estimate of a 'typical' sandy seafloor being in the range of a 'typical' clay sediment (see Fig. 2.7).

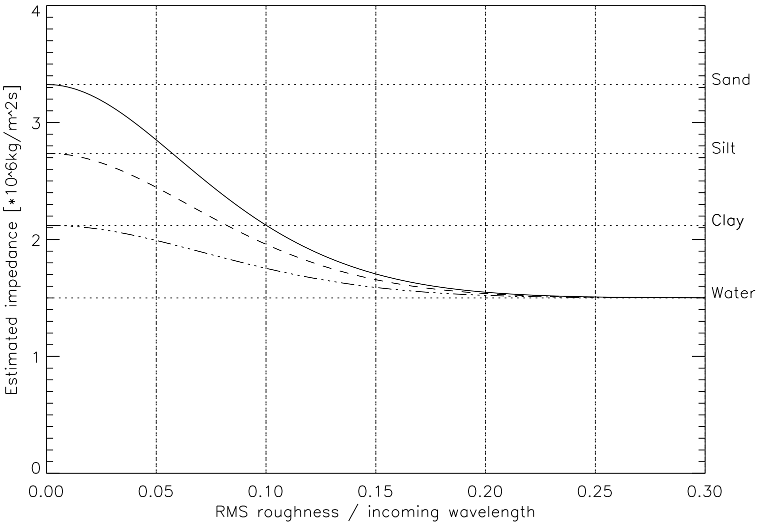

Figure 2.7: *Estimated impedance of a rough seafloor, only considering the backscattered energy. The impedance is shown as a function of RMS roughness divided by the incoming wavelength.*

2.5 Numerical implementation – BORIS

The Kirchhoff theory can be implemented numerically, and one such implementation is described here. Analytic expressions of the contributions from each surface and volume element of the seafloor are obtained and will be studied, together with the process for generating stochastic seafloor surfaces and volumes.

The numerical model BORIS – BOttom Response from Inhomogeneities and Surface – has for this report been used to generate input to the estimation technique, by calculating the reflection from a flat seafloor. It has also been used in the sensitivity analysis and to generate synthetic data for validating the algorithms.

BORIS has been developed at SACLANTCEN, by Pouliquen, Bergem, Canepa and Pace ([50], [9], [25]). The BORIS model is a 3-D model for calculating time-series signals backscattered from the seafloor (both surface and volume), by combining analytical expressions of the seafloor surface and volume response with a stochastic description of the seafloor. The expression for backscattered pressure from an elementary seafloor surface is based on the

Kirchhoff approximation and the expression for backscattered pressure from an elementary volume is based on small perturbation theory.

Figure 2.8 shows a block diagram of the model. Input to the model is a generated stochastic realization of seafloor surface and volume, transmitted pulse (as a function of time) and beam pattern[6] as well as the physical parameters of the seafloor. The beam pattern can be rotated and positioned. The parameters of the model are further presented in the sensitivity analysis, Sec. 5.1.1 (page 70).

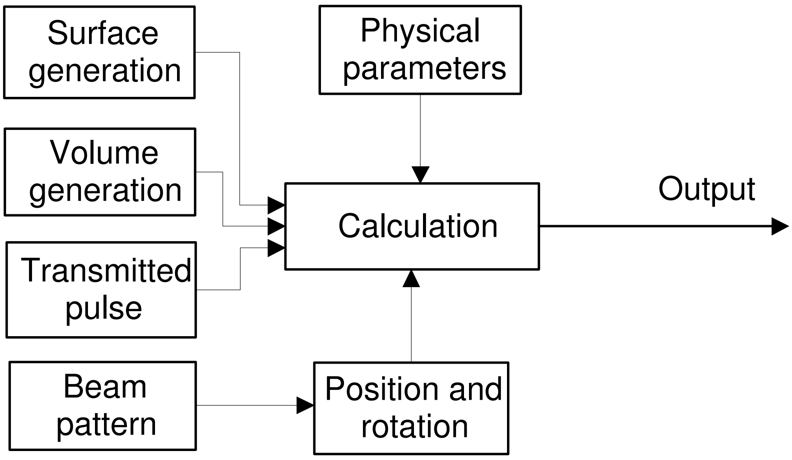

Figure 2.8: *Block diagram of the BORIS model, showing the main parts.*

The BORIS model has been tested against analytical solutions (the image solution, for a flat surface) and field data in [9], in order to verify the algorithm. In Section 5.2, a sensitivity analysis of the numerical parameters of BORIS (as sampling intervals etc.) is presented. This was mainly done in order to establish a set of parameters for use in the simulations.

In the following, a brief description of the theory behind BORIS will be presented, following [50] and [9]. We use the notation that $\mathbf{r}$ is the vector from the origin on the seafloor surface to a point on this surface, and $\mathbf{R}$ is the vector from the acoustic source to this point[7]. The following integral ([50]) forms the basis of the model:

---

[6] The beam pattern is given as signal strength as function of direction (but not distance)

[7] This is not the same notation as in [50]. The geometry is illustrated in Fig. 3.1 (page 47), in the case of a flat seafloor.

$$\begin{aligned} p(\mathbf{P},t) &= p_s(\mathbf{P},t) + p_v(\mathbf{P},t) \\ &= \int_S dp_s(\mathbf{P},t) + \int_V dp_v(\mathbf{P},t) \end{aligned} \tag{2.39}$$

This integral express that the pressure field received at the source position **P** from the seafloor is the sum of the elementary pressure fields over the seafloor surface (S) and the seafloor volume (V).

2.5.1 Seafloor surface contribution

The Kirchhoff approximation is used for the seafloor surface scattering. For a monostatic configuration with directivity patterns D_i and D_r (for incident and received beam, respectively), the seafloor surface contribution is given ([50]) by

$$\begin{aligned} dp_s(\mathbf{P},t) &= \frac{\cos(\gamma(\mathbf{R},\mathbf{n}))}{2\pi\overline{c_0}R^2}p_0 \\ &\quad \times (D_i(\mathbf{R})D_r(\mathbf{R})) \times \mathcal{R}_{01}(\mathbf{R},\mathbf{n}) \times e^{'}(t-\frac{2R}{\overline{c_0}}) \times d\mathbf{S_r} \end{aligned} \tag{2.40}$$

where $\mathcal{R}_{01}(\mathbf{R},\mathbf{n})$ is the local water-sediment plane wave reflection coefficient at the point $\mathbf{r}$, $\overline{c_0}$ is the average sound speed in water, $\gamma(\mathbf{R},\mathbf{n})$ is the angle between the incident direction and the vector $\mathbf{n}$ normal to the surface at $\mathbf{r}$ and p_0 is the source level. $e^{'}(t)$ is the time derivative of the transmitted pulse $e(t)$.

In Eq. 2.40, the first factor[8] contains the two-way transmission loss. The second factor is the transmitting and receiving directivity of the sonar, the third factor is the reflection coefficient for the water/seafloor interface and the last factor is the derivative of the transmitted pulse.

The water depth is fairly easy to determine from the measured data (using bottom detection and time-of-flight calculations), and the pulse shape and directivity patterns may be known from calibration of the system. The inclination angle of the beam with the seafloor, $\gamma(\mathbf{r},\mathbf{n})$, is dependent upon the roll, pitch and yaw of the vessel and the bathymetry of the seafloor surface, as well as the local surface gradient. The roll and pitch are usually recorded

---

[8] The different factors are separated by ×

and are in many cases sufficient in order to obtain the *mean* inclination angle, although the bathymetry of the seafloor surface might have to be accounted for in some cases. This can, e.g., be done from bathymetry data (e.g. from multibeam sonars). The local surface gradient is determined by the actual surface realization.

The main factor of Eq. 2.40 that is usually unknown is therefore the reflection coefficient, and we have the proportionality

$$dp_s(\mathbf{P},t) \propto \mathcal{R}_{01}(\mathbf{r}) = \frac{Z_1 - Z_0}{Z_1 + Z_0} \tag{2.41}$$

We would expect the mean total surface contribution to follow this proportionality for a fixed depth and a flat or fixed seafloor. This is in accordance with Sec. 2.1.

Equation 2.39 describes the integration over the surface. The integration is done over the actual surface realization, which is dependent upon the statistical description of the surface. This is further described in the sensitivity analysis, Sec. 5.4. The shape of the surface inflicts $\gamma(\mathbf{r},\mathbf{n})$ and $\mathcal{R}_{01}(\mathbf{R},\mathbf{n})$ in Eq. 2.40, and also $\mathbf{r}$ and $\mathbf{R}$. The changes in $\mathbf{r}$ and $\mathbf{R}$ are small, so the main effect is from phase differences and not the amplitudes. One very important parameter for the surface generation is the surface RMS roughness, σ. The effect of the surface roughness, both the RMS height and the other statistical parameters, are described in the theory (Sec. 2.4) and the sensitivity analysis (Sec. 5.4).

2.5.2 Volume contribution

The analytical expression for the volume contribution is based on Small Perturbation theory (see, e.g., [62]). The volume contribution is then ([50]) given by

$$\begin{aligned}
dp_v(\mathbf{P},t) \quad &= \frac{-n_1^2(\mathbf{r}^{'})}{2\pi R^2 \overline{c_0}^2} p_0 \cdot \mu(\mathbf{r}^{'}) \\
\times \quad & D_i(\mathbf{R}) D_r(\mathbf{R}) \times \mathcal{T}_{01}(\mathbf{R},\mathbf{n}) \mathcal{T}_{10}(\mathbf{R}_1,-\mathbf{n}) \\
\times \quad & \left(\frac{1}{\pi} \frac{\frac{\alpha R_1}{2\pi}}{(\frac{\alpha R_1}{2\pi})^2 + t^2} * e^{"} \left(t - 2 \left(\frac{\overline{n_1} R_1 + R}{\overline{c_0}} \right) \right) \right) \\
\times \quad & d\mathbf{V}_{\mathbf{r}}
\end{aligned} \tag{2.42}$$

In this expression, $\overline{n_1}$ is the average refractive index in the first few meters of the bottom, n_1 is the local refractive index at the location $\mathbf{r}^{'}$ of the volume element, and R_1 is the distance of penetration into the sediment (measured from point $\mathbf{r}$, such that $\mathbf{r}^{'} = \mathbf{r}+\mathbf{R_1}$). μ is the volume inhomogeneity coefficient, α is the attenuation coefficient, $\mathcal{T}_{01}(\mathbf{R}, \mathbf{n})$ and $\mathcal{T}_{10}(\mathbf{R}_1, -\mathbf{n})$ are the plane wave transmission coefficients. The double time derivative of the transmitted pulse $e(t)$ is denoted by $e^{''}(t)$.

Equation 2.42 describes the contribution from a volume element. The first factor is the two-way transmission loss multiplied with the volume inhomogeneities coefficient, the second factor is the directivity for transmitting and receiving, the third factor is the two-way boundary transmission loss. The final factor is a convolution involving the attenuation and the double time derivative of the transmitted pulse.

We see that we have the following proportionality

$$dp_v(\mathbf{P}, t) \propto \mu(\mathbf{r}^{'}) \times \mathcal{T}_{01}(\mathbf{R}, \mathbf{n})\mathcal{T}_{10}(\mathbf{R}_1, -\mathbf{n}) = \mu(\mathbf{r}^{'}) \times \frac{4 \cdot Z_1 Z_0}{(Z_1 + Z_0)^2} \qquad (2.43)$$

The influence of the convolution factor is on the attenuation of the volume signal with time, determined by the value of the attenuation coefficient α. The greater the value of α, the more attenuated the last part of the volume contribution will be. The frequency content will also be changed, since the higher frequencies are more attenuated than the lower ones.

The surface roughness σ will also influence the volume contribution, through $\mathcal{T}_{01}(\mathbf{R}, \mathbf{n})$, $\mathcal{T}_{10}(\mathbf{R}_1, -\mathbf{n})$, $\mathbf{r}$, $\mathbf{R}_1$ and $\mathbf{n}$. The scattering contributions from different volume elements will add incoherently, so presumably the transmission coefficients will be the most important.

2.5.3 Generation of seafloor surface and volume

The previous sections derived the analytical expressions for the backscattered pressure for surface (Eq. (2.40)) and volume (Eq. (2.42)) from elementary surfaces and volumes. The integration is done over a stochastic realization of the seafloor and volume (Eq. (2.39)).

The seafloor is generated in BORIS by using a Fourier algorithm, starting from a random spectrum. Fourier filtering generates a noisy power spectrum which is converted to spatial space by a Fourier transform (see [4] for details).

A band-passed power law spectrum W_s is used

$$\begin{aligned} W_s(\mathbf{K}) &= \eta \mathbf{K}^{-\nu} && \mathit{if} \quad K_{hp} < K < K_{lp} \\ &= 0 && \mathit{if} \quad K \leq K_{hp} \\ &= 0 && \mathit{if} \quad K \geq K_{lp} \end{aligned} \tag{2.44}$$

where $\mathbf{K}$ is a two-dimensional wave vector with magnitude equal to the wave number K. K_{hp} and K_{lp} are the high-pass and low-pass wave-numbers, respectively, η is a normalization factor and ν is related to the fractal dimension of the spectrum $(2 < \nu < 4)$. See Sec. 2.4.3 for further details on description of rough surfaces.

An exponential correlation function was chosen for generation of the volume, for which the corresponding power spectrum (i.e. the Fourier transform of the correlation function) is given by ([10]):

$$W_v(\mathbf{K}) = \mu^2(\mathbf{r}') \left(\frac{l_v}{\pi(1 + K_{z_1}^2 l_v^2)} \cdot \frac{l_h^2}{2\pi(1 + K_{r_1}^2 l_h^2)^{3/2}} \right) \tag{2.45}$$

where l_v and l_h are the vertical and horizontal correlation lengths and $\mathbf{K} = \mathbf{K}_{\mathbf{z}_1} + \mathbf{K}_{\mathbf{r}_1}$. Layering is often found in sediments, and this corresponds to a larger horizontal than vertical correlation length. Gensane [31] found that for some typical seabeds, $l_h \sim 5 \cdot l_v$. The volume is generated by Fourier filtering, as for the seafloor.

2.6 The parametric sonar

In this section, the parametric sonar will be described. The basic principles will be described first. The properties of the specific sonar that has been used for the sea trials of ISACS will then be described, including calibration data.

2.6.1 Properties of the parametric sonar

Water has non-linear properties; the change of density caused by a change in pressure is not linearly proportional to the change in pressure (see, e.g., [59]). This non-linearity leads to non-linear acoustic propagation where a variety of additional frequencies in water are found to be generated. The acoustic non-linearity in water only appears at high sound levels.

The parametric sonar utilizes the non-linear sound propagation in water. By emitting two primary beams at frequencies close to each other, a secondary beam at the difference frequency, as well as one at the sum frequency, will be generated in the water column. The sonar thus works as a virtual end-fire array with considerably larger dimensions than the physical size of the sonar. The difference frequency beam has several appealing properties [59]:

1. No side-lobes at the difference frequency.
2. A narrower beam than can be achieved by direct generation of the difference frequency at the same physical size of the antenna. This beam width is comparable with the beam width at the primary frequencies.
3. Very broad bandwidth is possible. This is because a large proportional change in the difference frequency can be achieved by making only a small proportional change in (one or both of) the primary frequencies.
4. The beam width is nearly constant over a broad frequency band.
5. Projector cavitation is not a problem (due to the transmission at high frequencies).

The main disadvantage of the parametric sonar is the poor efficiency, since only a small part of the transmitted energy appears at the difference frequency (which the system is designed to be used at).

These properties of the parametric sonar makes it a suitable instrument for use with the proposed characterization technique. The most important factors are that the frequency band is in the kHz range and that the bandwidth is wide.

2.6.2 Description of the parametric sonar Simrad TOPAS PS040

The parametric sonar that has been used in this work is the bottom penetrating sonar Simrad Topas PS040. The sonar provides broad band pulses; Burst, Ricker or Chirp (FM sweep), centered at 1-10kHz. The primary operating frequency is around 42kHz. The primary source level is about 240dB$//\mu Pa@1m$, while the secondary source level is typically 204dB$//\mu Pa@1m$ (6kHz). The sampling frequencies used in the ISACS sea trials were 50kHz and 100kHz.

A further description of the sonar TOPAS PS040 can be found in the product manual [54]. Most of the following calibration information is taken from [54], [7] and the actual data files from the calibration.

The source level, in dB relative to the intensity of a plane wave of pressure equal to $1 \mu Pa$, is shown in table 2.1[9] [7].

Pulse	PL (%)	Primary SL (dB)	Secondary SL (dB)
R 10 kHz	100	202.4	235.5
R 10 kHz	50	191.4	229.2
R 8 kHz	100	203.9	236.3
R 8 kHz	50	193.3	230.4
R 5 kHz	100	206.2	238.9
R 5 kHz	50	195.5	233.1

Table 2.1: *Source level, for a Ricker pulse at 50 or 100% effect, in dB relative to the intensity of a plane wave of pressure equal to* $1 \mu Pa$. *The measurement was done at a distance of 50.4m. The calculation assumes* $20 \log r$ *spreading.*

The measured beam pattern is shown in Fig. 2.9, when a pulse with center frequency of 8kHz is used. It is also shown in Fig. 5.30 (page 100), together with Gaussian shaped beam patterns. As seen, the beam pattern is not fully axi-symmetric. The beam pattern measured for a 10kHz center frequency pulse is slightly narrower, but just slightly (see [7] for details).

The shape and power spectrum of the utilized Ricker pulse are shown in Fig. 2.10 and Fig. 2.11. The shape and power spectrum of the utilized Burst pulses are shown in Fig. 2.12 and Fig. 2.13. The Ricker pulse has a more regular shape and power spectrum, but the Burst is sometimes utilized because it puts out a larger amount of energy into the water, and the penetration into the sediments is a little better. The source pulse level as a function of distance is shown in Fig. 2.14, clearly showing the long-ranging near-field effects of a parametric source (∼35m in the case of the PS040), due to the generation of the difference frequency in the water column itself. The parametric source acts like a long end-fire array in the water column [57].

---

[9] The values are corrected, i.e. 6dB lower than the (wrong) values in the report ([7]).

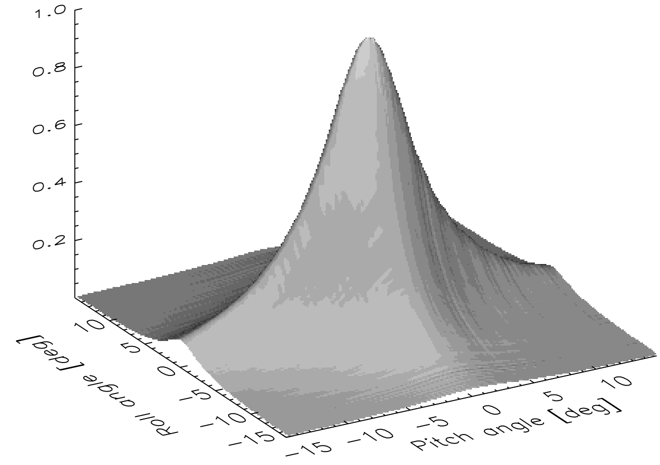

Figure 2.9: *Beam pattern of the TOPAS PS040. As seen, it is not fully axi-symmetric.*

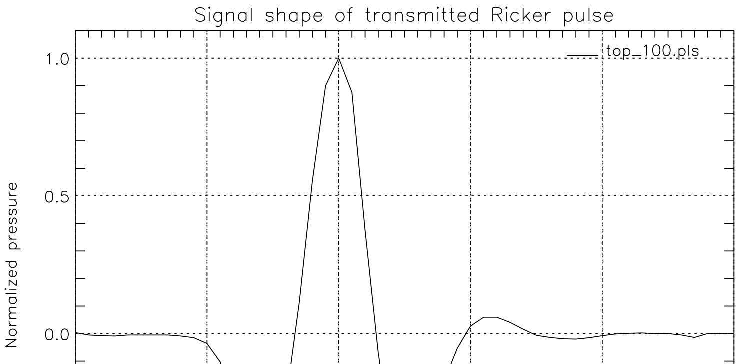

Figure 2.10: *The shape of the recorded TOPAS Ricker pulse, when centered around 8kHz.*

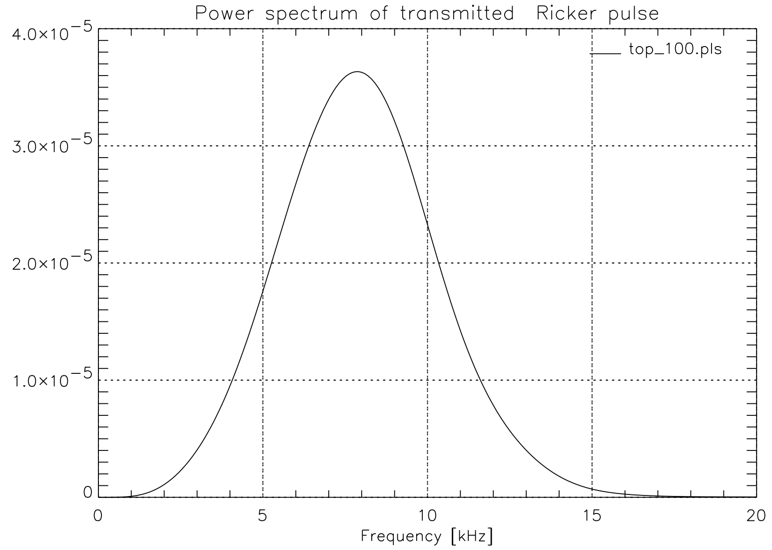

Figure 2.11: *Power spectrum of the recorded TOPAS Ricker pulse, when centered around 8kHz.*

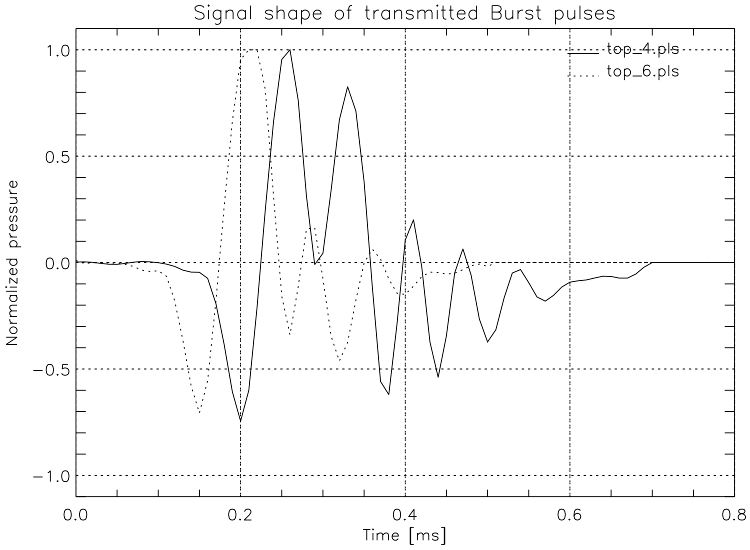

Figure 2.12: *The shape of the recorded TOPAS Burst pulses, when centered around respectively 4 and 6kHz.*

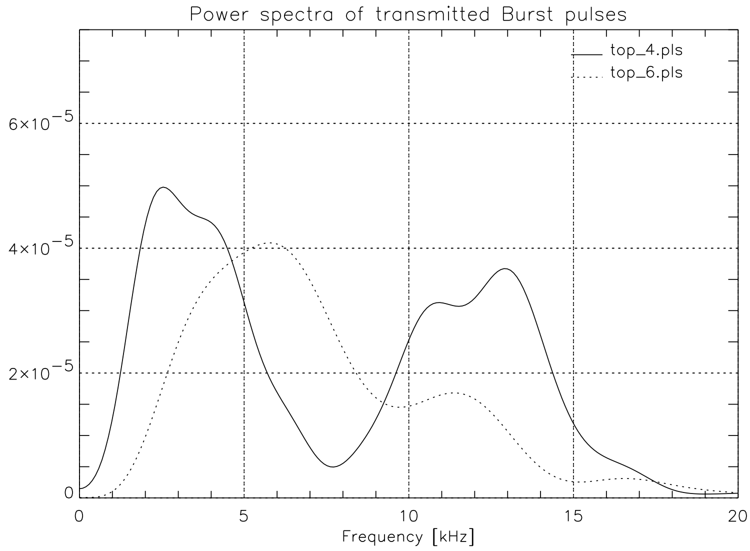

Figure 2.13: *Power spectrum of the recorded TOPAS Burst pulses, when centered around respectively 4 and 6kHz.*

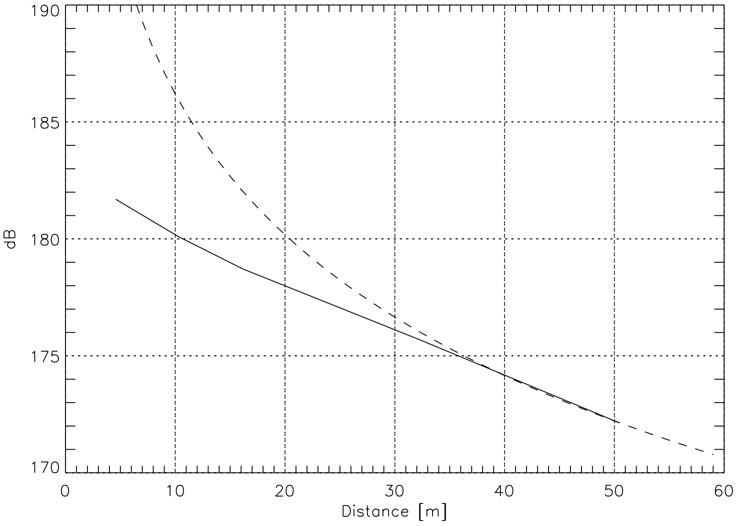

Figure 2.14: *Measured source pulse level, as a function of distance from the source, when using a Ricker pulse. Spherical spreading (*$\propto 20 \log r$*) is shown as a dashed line.*

2.7 Seafloor class definition

A characterization/estimation technique should be able to characterize a wide variety of seafloors. If an accurate characterization is not possible, it is certainly an advantage if these situations are detected such that a faulty characterization is avoided.

In order to be able to test the developed estimation technique on representable seafloors, a set of predefined seafloor classes has been used. The chosen set contains 19 classes, which are listed with their respective parameters in Table 2.2.

Class	Description	Sound vel. c_1 $[m/s]$	Density ρ_1 $[\frac{g}{cm^3}]$	Surf.rms σ $[m]$	Vol.inho. μ	Att. β $[\frac{dB}{m}]$	Att. $\alpha[\frac{dB}{m\cdot kHz}]$	Impedance Z $[\frac{kg}{m^2 s}]$
A1	Rock	4000	2.0	0.080	0.010	0.01	0.002	$8.00\cdot10^6$
B1	Gravel	2200	2.0	0.040	0.020	0.60	0.069	$4.40\cdot10^6$
B2	Coarse sand	1830	2.0	0.030	0.020	0.80	0.092	$3.66\cdot10^6$
B3	Coarse sand	1830	2.0	0.015	0.020	0.80	0.092	$3.66\cdot10^6$
C1	Fine sand	1750	1.9	0.020	0.020	0.60	0.069	$3.33\cdot10^6$
C2	Fine sand	1750	1.9	0.010	0.020	0.60	0.069	$3.33\cdot10^6$
D1	Silty sand	1650	1.8	0.020	0.030	0.50	0.058	$2.97\cdot10^6$
D2	Silty sand	1650	1.8	0.010	0.030	0.50	0.058	$2.97\cdot10^6$
E1	Silt bio	1610	1.7	0.010	0.040	0.25	0.029	$2.74\cdot10^6$
E2	Silt	1610	1.7	0.010	0.020	0.25	0.029	$2.74\cdot10^6$
F1	Clay silt	1550	1.5	0.010	0.030	0.15	0.017	$2.33\cdot10^6$
F2	Clay silt	1550	1.5	0.010	0.050	0.15	0.017	$2.33\cdot10^6$
F3	Clay silt	1550	1.5	0.020	0.040	0.15	0.017	$2.33\cdot10^6$
G1	Clay bio	1515	1.4	0.010	0.040	0.15	0.017	$2.12\cdot10^6$
G2	Clay	1515	1.4	0.010	0.020	0.15	0.017	$2.12\cdot10^6$
H1	Clay bio fine	1490	1.4	0.010	0.040	0.10	0.012	$2.09\cdot10^6$
H2	Clay fine	1490	1.4	0.010	0.010	0.10	0.012	$2.09\cdot10^6$
I1	Sand weed	1830	2.0	0.060	0.010	0.95	0.109	$3.66\cdot10^6$
I2	Sand pose.	1830	2.0	0.080	0.010	0.95	0.109	$3.66\cdot10^6$

Table 2.2: *The parameter values for the predefined classes. The calculated specific acoustic impedance is also included.*

These predefined classes were defined at SACLANTCEN in 1996, mainly by E. Pouliquen and O. Bergem. One purpose of their work was to use it for BORIS simulations. It has been used in, e.g., a preliminary study of seafloor characterization using BORIS simulations by Berntsen [11].

Typical values of sound speed, density and attenuation are taken from Hamilton ([34], [33], [35]). The utilized numerical model BORIS treats the attenuation as proportional to frequency, but in the input files to BORIS the attenuation, β, is given in dB/m at a frequency of 8686Hz ([25, page 61]). Both this value and the attenuation in $dB/m/kHz$, denoted as α, are therefore given in Table 2.2. Given the high variability of roughness and volume inhomogeneities for the seafloor, values are chosen to cover a wide range. The surface exponential factor is set to $\nu = 4$. The correlation lengths that have been used for the seabed volume are $l_h = 0.3$m and $l_v = 0.06$m, for all classes. These values have been determined in discussions between E. Pouliquen, O. Bergem and B. Berntsen, and are further investigated in the sensitivity analysis (Chap. 5).

Chapter 3

Description and analysis of a monostatic sonar system

This chapter takes a closer look at sonar systems for use in characterization and/or classification of the seafloor. The entire measurement system and propagation medium is treated, from the transmission of the signal until it is recorded. Only monostatic systems are considered, but the main parts of the analysis might as well be applied to bi-static systems. For a monostatic system, the source and receiver are at the (approximately) same position[1].

For a bi-static or multi-static system, the source(s) and receiver(s) are separated in space. This might e.g. be done by having an array with one or several receivers (collected in one or more streamers) towed behind the survey vessel, with the source(s) on the vessel itself or being towed behind.

This report primarily concerns use of single beam transmitters/receivers, and beam forming will not be issued here.

3.1 The main processes

The main processes of the sound transmission, propagation, scattering and reception are summarized below. Also included are important factors to consider in the analysis.

---

[1] The same transducer is often used for both transmission and reception.

1. **Transmission** of the signal from a source. Important factors are source level, pulse shape (and frequency spectrum), beam pattern and transmission position and angles (including roll, heave, pitch).
2. **Propagation** of sound in the water column, including ray bending, spreading loss, absorption, scattering from inhomogeneities (e.g. fish) and nonlinear effects.
3. **Scattering from the seafloor surface.** Factors to consider are water properties (speed of sound, density), bottom properties (speed of sound, both for pressure and shear waves, density) and seafloor shape (roughness spectrum), angles of incidence and possible objects.
4. **Scattering from the volume.** Bottom properties (changes and fluctuations in density and/or speed of sound, e.g. layering and inhomogeneities) and objects influence the volume scattering.
5. **Propagation** of sound in the water (backpropagation, from scattering back to the receiver(/transmitter)); see above
6. **Reception** of the signal. Factors to consider are the position and movements of the boat (including roll, heave, pitch), noise from the boat itself (propeller, machine noise), other boats, wind and waves. Local reflection effects etc. around the receiver and properties of the receiving hydrophone itself might also be important. Properties of the receiver chain (frequency response of the electronics etc.) might also have to be accounted for.

The source level, pulse shape (and frequency content) and beam pattern all need to be considered when analyzing the system. The construction and dimensions of the sonar set some limits on these factors (see, e.g., [59]). From a calibration of the system, the source level and beam pattern can be found with a good accuracy, although the source level might change slightly with changing water properties[2]. The pulse (as a function of time) can be recorded during transmission, as well as the position and heading of the boat. Some sonar systems can correct for e.g. rolling angle when transmitting, so that the transmission direction is independent of the roll. If the roll values are small, they might be neglected in calculations.

Propagation in the water column may, if the speed-of-sound in the water is (nearly) constant as a function of depth or the inclination angle is near

---

[2] This is the case for e.g. a parametric sonar

vertical, be considered as following a straight path without ray bending. The spreading loss for a point source in free space is inversely proportional to the distance, $p(r) = \frac{p_0}{r}$, and this relationship might be used in the far field for other sources as well. In the near field, the characteristics of the specific sonar must be used. The near field for a parametric sonar is rather large ($\sim 40m$, see [8]), since much of the pulse is generated in the water due to the nonlinear interaction between acoustic signals in water (Sec. 2.6). This must be accounted for in the analysis. Inhomogeneities in the water column, as e.g. fish or schools of fish, can introduce unwanted scattering (when the purpose is seafloor characterization or classification). The effect of this can be reduced by omitting the first part of the time series, and by filtering. The attenuation of sound waves in the kHz range in sea water is fairly low (Sec. 2.2). Corrections for attenuation are quite straight-forward to implement, but are often not necessary, at least for vertical-looking sonars used in relatively shallow water.

The reflection and refraction on most real-life seafloors is a complex process with several parameters. Empirical models can be used to describe the process, but physical models might give more knowledge about the process itself and the relative importance of the different determining parameters, thus facilitating a classification/characterization process. Some important parameters are the impedance contrast (water/seafloor), relative seafloor roughness (compared to signal wave length), the roughness spectrum and the real grazing angle[3]. On real seafloor surfaces, rocks, shells and other objects might highly influence the backscattered signal. The scattering from a rough seafloor is further treated in Sec. 3.2.

The sound that penetrates the seafloor surface is refracted and scattered in the volume due to changes in the sound speed and densities, both at small inhomogeneities and on larger scales. Multiple scattering within the volume occurs, but might be neglected when the scattering level is low compared to the incoming sound level. The volume scattering level is often considerably smaller than the seafloor surface contribution, but might still contain important information. Volume scattering might be modeled by 'large-scale' sound speed and density profiles and statistical variations in these, although for a real seafloor rocks and other objects, life (shells etc.), bioturbation etc. contributes to the scattering. The two-way penetration through the seafloor surface is important for the resulting volume scattering contribution. Section 3.2 treats this further.

---

[3] By 'real grazing angle' we mean the angle between the acoustic beam and the local part of the seafloor, not between the beam and the mean sea surface

Reception of the backscattered signal might be influenced by several factors, as local reflections near/around the hydrophone/transducer (this might be modeled by a transfer function, found by calculations and/or calibration) and noise from the ship itself, other ships, wind and waves. The position and movement (roll, pitch, etc.) of the boat are also important factors, as well as the transducer and receiving/recording system properties; beam width, sensitivity (perhaps frequency dependent), sampling rate. Aliasing problems are avoided by using a low-pass filter. Both low- and high-pass filtering are commonly used for reducing noise.

3.2 Reflection and refraction on and in the seabed

The reflection and refraction on and in the seabed is the most important, and difficult, part of the analysis. If the structure and parameters of the bottom were known in detail, the resulting time series could be calculated very accurately. What we want to do, however, is to classify or characterize an unknown seabed from acoustic measurements. Several combinations of seafloor shapes and parameters could yield the same measurement results, thus what we need is to identify a smaller set of parameters that allows a reasonable modeling of the seafloor that also can (partly) be extracted from the measured data.

Kirchhoff theory is selected to model the surface scattering (see Sec. 2.4.4). For the volume, the Small Scale Perturbation theory has been chosen (see Sec. 2.5). However, the emphasis has been on the surface return and the estimation of parameters determining the surface return.

3.3 Geometrical considerations

This section studies the influence of the geometry of a sonar on the backscattered signal, including scattering from both seafloor surface and volume.

3.3.1 Fresnel zones

We are considering reflection of spherical waves from a plane surface (without roughness), which is relevant for, e.g., monostatic sonar systems illuminating the seafloor. Phase considerations lead to so-called *Fresnel zones*, or *phase zones*. See e.g. [26, page 49-].

Sound is transmitted from a spherical source and reflected at a plane surface. By summing all the wavelets reflected from the surface we get an expression for the received signal (at the same position as the transmitter). This signal is highly dependent on the phase-shift between the different reflecting elements of the surface. Essentially, we get positive contributions from a circle close to normal incidence, where the phase shift $\Delta\Phi$ is less than π, then negative (or canceling) contributions from a ring where the phase-shift is $\pi \leq \Delta\Phi \leq 2\pi$. And so on. By letting $\Delta\Phi = n\pi$, where n denotes the n'th Fresnel zone, the phase changes sign at radii

$$r_n = \left(\frac{\lambda h}{2}\right)^{1/2} n^{1/2} \tag{3.1}$$

The radius r_n limits the n'th Fresnel zone and h is the depth. Thus a signal reflected from a disk with radius r_1 has the maximum possible amplitude, then the reflected signal is decreased as the radius approaches r_2. The amplitude then follows an undulating (but decreasing) pattern as the radius increases and the disk includes more and more Fresnel zones. For a perfectly reflecting disk with infinite radius the reflected signal ([10]) will be given by

$$-\frac{e(t - 2h/c_0)}{2h}$$

where $e(t)$ is the transmitted pulse and c_0 the speed of sound in water. This is called the image solution.

For a broad-band pulse and a narrow beam, the Fresnel zones might introduce an apparent frequency shift as the depth increases. This happens when e.g. one Fresnel zone is covered for the frequencies in the lower part of the spectrum, while several zones are covered for the high-frequency components. As the depth then increases, more Fresnel zones are included and the relative amplitude of the low and high frequencies are changed. This effect will be studied in the sensitivity analysis (Chapter 5).

Example: Table 3.1 shows the limiting radius of the first Fresnel zone, for some values of frequencies and depths. As seen, for quite shallow water and frequencies typical for e.g. the TOPAS system, the reflections will all be from within the first Fresnel zone.

f	h=15m	h=30m	h=60m
1kHz	3.4	4.7	6.7
5kHz	1.5	2.1	3.0
10kHz	1.1	1.5	2.1

Table 3.1: *The radius of the first Fresnel zone, as a function of frequency f and water depth h, in meters. As a comparison, a 3.5-degree half-width beam (e.g. the TOPAS system) will have 0.9m, 1.8m and 3.7m radius at 15m, 30m and 60m water depth, respectively.*

3.3.2 The geometry of a monostatic sonar

Figure 3.1 illustrates the geometry of a vertical-looking sonar illuminating the seafloor surface and subsurface. From the figure, we have that R is given by $R = \frac{h}{\cos\theta}$ and $\Delta R = R - h = h(\frac{1-\cos\theta}{\cos\theta})$. The pulse length can alternatively be noted by its duration, $\Delta t_{pulse} = \frac{l_{pulse}}{c}$. The following equation gives the time for when the pulse reaches the seafloor surface:

$$t = \frac{h}{c_0 \cos\theta} + \Delta t \tag{3.2}$$

where c_0 is the speed of sound in water and Δt is a given time delay.

We can then specify some characteristic points in time:

- The first part of the pulse reaches the seafloor at: $t_0^{\theta=0} = \frac{h}{c_0}$
- The last part of the pulse reaches the seafloor at: $t_1^{\theta=0} = \frac{h}{c_0} + \Delta t_{pulse}$
- The first part of the pulse reaches the seafloor at the maximum beam angle at: $t_0^{\theta=\theta_{max}} = \frac{h}{c_0 \cos\theta_{max}}$
- The last part of the pulse reaches the seafloor at the maximum beam angle at: $t_1^{\theta=\theta_{max}} = \frac{h}{c_0 \cos\theta_{max}} + \Delta t_{pulse}$

The effect of roughness can also be included, as a time-delay $\Delta t_{rough} \sim l_{rough}/c_0$, where l_{rough} is a characteristic scale of the roughness, e.g. the RMS roughness. A roughness of [1,2,4]cm corresponds to Δt_{rough}=[7,13,27]μs, i.e. 10% or less of a typical pulse length ($\sim$ 250μs, Sec. 2.6). This means that the time window used for extracting the surface contribution from the total return needs only to be a little larger to compensate for roughness effects.

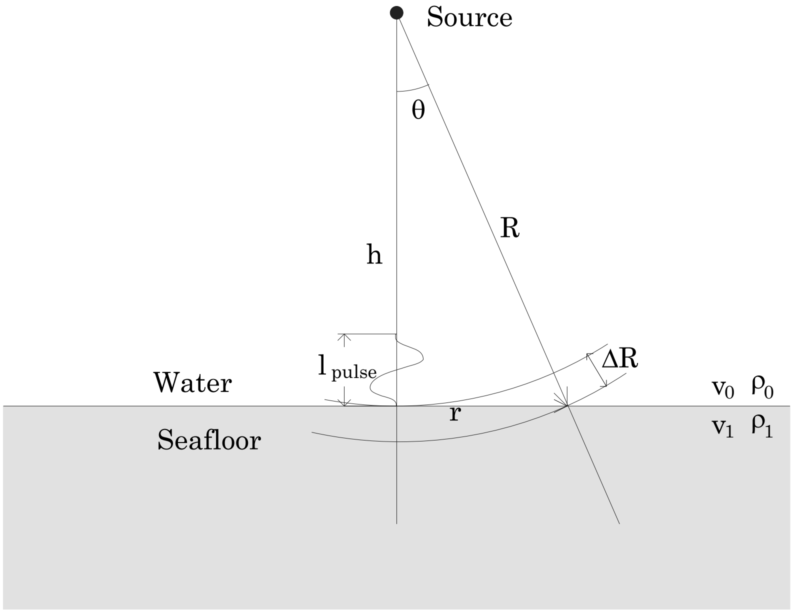

Figure 3.1: *Geometry of a sonar.*

The total length of the returned signal can be expressed as a function of depth, beam pattern, pulse length and roughness. The time delays from beam pattern and roughness must then be multiplied with two, since the rays travel both ways. The following expression is then obtained

$$\Delta t_{SurfReturn} = \frac{2h}{c_0} \cdot \frac{1-\cos\theta_{max}}{\cos\theta_{max}} + \Delta t_{pulse} + \frac{2l_{rough}}{c_0} \tag{3.3}$$

This length is used when specifying a window for extracting the surface contribution (Sec. 4.3.2).

Table 3.2 shows the relative length of the pulse, compared to $2\Delta R$, the increase in two-way travel distance due to angle. The length of a Ricker pulse centered at 8kHz is about 0.25ms, which has been used to produce the table. Typical depths and angles are used. As seen in the table, for a narrow beam and moderate depths, a typical pulse length is much larger than the delay caused by the beam pattern width, and the return can be considered to come from an area limited only by the beam pattern. When the beam is wide or the depth large, however, only parts of the area limited by the beam pattern will contribute to the scattering at a specific time. Section 3.3.1 considers Fresnel zones, which also should be taken into consideration.

θ	h=15m	h=30m	h=60m
4°	5.119	2.559	1.280
8°	1.272	0.636	0.318
16°	0.310	0.155	0.078
32°	0.070	0.035	0.017

Table 3.2: *The length of the pulse divided on the two-way distance increase due to angle:* $l_{pulse}/(2\Delta R)$*, as a function of depth and angle. The angle can be compared to the half beam width of beam patterns. A TOPAS system has a half beam width of about 3.5°.*

Generally, the transmitted pulse will first hit the seafloor at $\theta = 0$, then for larger angles. Thus, the illuminated surface area will increase with time until the beam width limiting angle is reached. The illuminated area will then decrease when the end of the pulse is reached. The illuminated volume will become larger and larger with time. First, a development like for the surface takes place; the covered volume quickly increases until the beam width limiting angle is reached. Afterwards, the covered volume has essentially the shape of a spherical shell with the solid angle determined by the beam width. The thickness of the shell increases with time until it is limited by the pulse length.

The illuminated volume, assuming a narrow beam and moderate depth, increases nearly linearly with time until the whole pulse is within the volume. After that, it increases slower with time, as the thickness is limited. However, the effects of spherical spreading and attenuation cause the backscattered volume return to diminish with time.

The surface scattering is proportional to scattering area within the first Fresnel zone, and almost independent of area when several Fresnel zones are covered. The volume return is proportional to the illuminated volume which depends on both scattering area and penetration into the volume (which also increases when the beam pattern width increases). This means that the relative volume contribution (compared to surface scattering) is smaller for a narrow beam. This is an argument for using a narrow beam, if one wants to extract the surface return.

The next section will give a quantitative analysis of what has been qualitatively treated in the current section.

3.3.3 Calculation of illuminated area and volume

This section calculates the illuminated area and volume for a monostatic sonar, as a function of time. This will give an impression of the importance of the surface and volume scattering, as a function of time, for different water depths, beam widths and pulse lengths.

The illuminated area of the seafloor, with the shape of a two-dimensional torus, is given by

$$A = \int_{r_1}^{r_2} 2\pi r \mathrm{d}r = \pi(r_2^2 - r_1^2) \tag{3.4}$$

where r is the radius and r_1, r_2 are the inner and outer radii of the torus.

Alternatively, a shape function $F(r)$ (e.g. a beam pattern) can be incorporated, and the area will then be given by $A = \int_{r_1}^{r_2} F(r) \cdot 2\pi r \mathrm{d}r$.

Using that $\cos^2\theta = \frac{h^2}{R^2} = \frac{h^2}{r^2+h^2}$ (Fig. 3.1), we can find the radii of such a torus

$$\begin{aligned} r_2 &= \sqrt{t^2 c_0^2 - h^2} \times I\left\{h/c_0 < t < \sqrt{r_{max}^2 + h^2}/c_0\right\} \\ r_1 &= \sqrt{(t - \Delta t_{pulse})^2 c_0^2 - h^2} \\ &\quad \times I\left\{h/c_0 + \Delta t_{pulse} < t < \sqrt{r_{max}^2 + h^2}/c_0 + \Delta t_{pulse}\right\} \end{aligned} \tag{3.5}$$

where $I\{expression\}$ is the indicator function[4]. Eq. (3.4) can then be used to find the illuminated surface area as a function of time, depth, beam width and pulse length.

The illuminated volume is found by using that the volume of solid of revolution of the curve $y = f(x)$ about the x-axis between $x = a$ and $x = b$ is equal to $\pi \int_a^b y^2 \mathrm{d}x$ (see, e.g., [3]), which can be used for both finding a formula for a part of a sphere and a cone. Generally, the illuminated volume has the shape of a spherical shell with the solid angle determined by the beam width, and the shape of the illuminated volume can be approximated by two spherical shapes (V_1 and V_3 below) limited by the pulse length, and with a conical shape (V_2) in between. Ray bending effects have not been included in the analysis.

The volume contributions are given by:

---

[4] The indicator function $I\{expression\}$ is 1 if the expression is true, 0 otherwise.

$$\begin{aligned}
V_1 &= \left(2/3\pi R^3 - \pi h R^2 + 1/3\pi h^3\right) \times I\left\{t > h/c_0\right\} \\
&\quad \times I\left\{t \leq (h/c_0 + h/(c_1 \cos(\theta_{beam})) - h/c_1))\right\} \\
&+ \pi R^3 \left(2/3 - \cos(\theta_{beam}) + 1/3 \cos(\theta_{beam})^3\right) \\
&\quad \times I\left\{t > (h/c_0 + h/(c_1 \cos(\theta_{beam})) - h/c_1)\right\} \\
V_2 &= (1/3\pi \cos(\theta_{beam}) \sin(\theta_{beam})^2)(R^3 - (h/\cos(\theta_{beam}))^3) \\
&\quad \times I\left\{(R - l_{pulse}) \cos(\theta_{beam}) < h\right\} \\
&\quad \times I\left\{t > (h/c_0 + h/(c_1 \cos(\theta_{beam})) - h/c_1)\right\} \qquad (3.6) \\
&+ (1/3\pi \cos(\theta_{beam}) \sin(\theta_{beam})^2)(R^3 - (R - l_{pulse})^3) \\
&\quad \times I\left\{(R - l_{pulse}) \cos(\theta_{beam}) \geq h\right\} \\
&\quad \times I\left\{t > (h/c_0 + h/(c_1 \cos(\theta_{beam})) - h/c_1)\right\}
\end{aligned}$$

$$\begin{aligned}
V_3 &= \left(2/3\pi (R - l_{pulse})^3 - \pi h (R - l_{pulse})^2 + 1/3\pi h^3\right) \\
&\quad \times I\left\{t \leq (h/c_0 + h/(c_1 \cos(\theta_{beam})) - (h - l_{pulse})/c_1))\right\} \\
&\quad \times I\left\{t \geq (h/c_0 + l_{pulse}/c_1)\right\} \\
&+ \pi (R - l_{pulse})^3 (2/3 - \cos(\theta_{beam}) + 1/3 \cos(\theta_{beam})^3) \\
&\quad \times I\left\{t > (h/c_0 + h/(c_1 \cos(\theta_{beam})) - (h - l_{pulse})/c_1)\right\} \\
&\quad \times I\left\{t \geq (h/c_0 + l_{pulse}/c_1)\right\}
\end{aligned}$$

where c_1 is the speed of sound in the sediment, θ_{beam} the half beam width and R is the radius of the front of the pulse, $R = c_1(t - h/c_0) + h$.

The total illuminated volume can then, by using Eq. (3.6), be calculated from

$$Volume(t) = V_1(t) + V_2(t) - V_3(t) \qquad (3.7)$$

Figure 3.2 shows an example of illuminated seafloor area and volume, as a function of time. The scattering from the surface is approximately proportional to the illuminated surface area (not including the effect of tapering beam pattern, and not valid for coherent scattering when several Fresnel zones are covered). The scattering from the volume is approximately proportional to the illuminated volume, before accounting for spreading loss and attenuation.

The inclination of the first and last part of the surface area (the trapezoidal graph) is determined by the depth, and the total length in time for the surface contribution is determined by the depth, beam width and pulse length. In

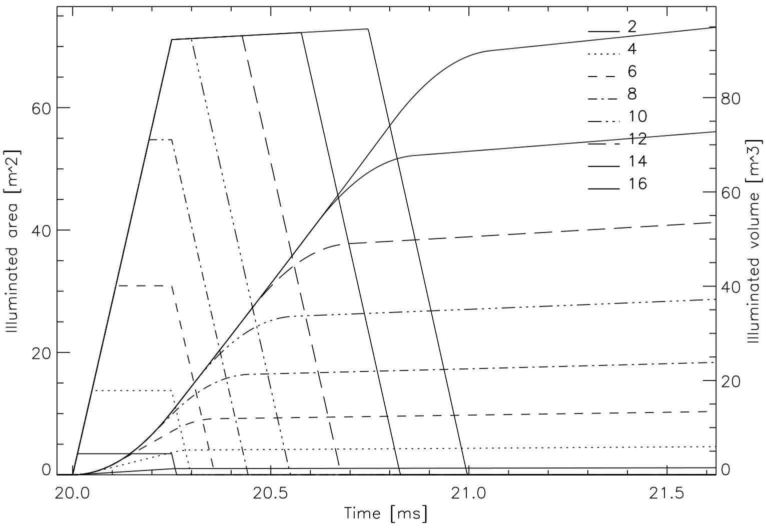

Figure 3.2: *Illuminated seafloor area and volume as a function of time, for different half beam widths (see legend; [degrees]). The trapezoid shaped graphs are the areas. The smaller beam widths cover less area/volume. The depth is 30m and the pulse length 0.25ms.*

this example, for angles above about 9° half width, the coverage of the area is limited by the pulse length so that the whole area within the beam width is never covered completely (the almost flat top of the curves of beam widths above 9°).

The illuminated volume increases slower when the whole pulse is into the volume (which, as seen in the figure, happens earlier for narrow beams). When the pulse is completely within the volume, the illuminated volume increases nearly linearly with time. However, the backscattered signal from the volume will most of the time decrease with time, when we include the effects of spherical spreading and attenuation.

From Fig. 3.2 one may see that the relation between total volume scattering divided on total surface scattering, integrated over a time window covering the complete surface contribution, is larger for larger beam widths. Such a time window is also used in the surface parameters estimation. Actual numbers are shown in Table 3.3. This favors the use of narrow beams, as only the surface contribution is used in the surface parameter estimation.

Half beam width	2	4	6	8
Vol./Surf. [m]	0.20	0.23	0.27	0.34
Half beam width	10	12	14	16
Vol./Surf. [m]	0.42	0.52	0.64	0.77

Table 3.3: *Illuminated volume divided on illuminated area for a sonar, indicating the relative relation between total volume scattering divided on total surface scattering. Integration over a time window covering the complete surface return has been used.*

3.4 Summary and conclusions

This chapter has treated monostatic sonar systems, in the scope of characterization or classification of the seafloor. The main processes have been identified, and important issues clarified. Some conclusions are summarized below.

- The propagation of sound in water can be considered as following straight lines, as long as the beam is nearly vertical.
- Scattering from objects in the water column, e.g. fish, can often be removed by using a time window on the backscattered signal. The scattering from fish does not seem to be a problem from analysis of field data (Chapter 6).
- Local effects caused by e.g. the mounting of the sonar (reflection from the sea surface and/or vessel, noise etc.) and the acquisition system might in some cases have to be taken into account. This can be done by calculating a transfer function from a calibration of the system and using this to reduce the effects.
- The most important factors are the scattering processes themselves. The physical properties of the seafloor (sound speed, density, roughness, attenuation, volume inhomogeneities) are important, but also variables like the water depth, beam pattern and pulse length.
- Spherical spreading is usually valid in the far field from a source. In the near field, the specific properties of the utilized sonar must be used. The near-field of a parametric sonar might be large ($\sim 40m$, see [8]).

- Wide beams illuminate more Fresnel zones, which means the backscattered coherent energy is less dependent upon the exact beam pattern, and thus the accuracy of the calibration of the system is somewhat less important.

- Within a time window determined by the length of the surface contribution, the volume contribution is lower (also compared to the surface contribution) for narrow beams, which is preferred in the estimation process since only the surface contribution is used for estimating surface parameters.

- The length of the surface return, and thereby the size of the time window used for extracting the surface return, is dependent upon water depth, beam pattern, pulse length and the seafloor surface roughness. Water depth and beam pattern width are usually the most important factors.

- Using a non-normal incidence beam, or illuminating a sloping surface, will lead to a longer surface scattering contribution.

- The frequency distribution of the transmitted signal is important in the scattering process. From theory (Chap. 2) it is seen that using the coherent part of the backscattered signal seems to be a suitable approach to characterization. This was chosen as the approach for the work presented (Sec. 1.1). For this, a broad band signal is necessary, with a suitable center frequency. A center frequency of a few kHz seems reasonable, giving a sufficiently coherent return which still is being affected by typical seafloor roughness.

Chapter 4

Estimation of seafloor parameters

This chapter describes the seafloor characterization method that has been developed. It is called FARIM – Frequency Analysis based Roughness and Impedance estimation Method. Currently, seafloor RMS roughness and impedance are estimated. Further development should include estimation of volume inhomogeneities factor and volume attenuation coefficient.

The chapter will start with an overview of FARIM, and then go into the details. Evaluation of the algorithm for synthetic data will be presented. Possible limitations of the technique will also be discussed.

4.1 Overview of the estimation technique

The basis of the estimation technique is Eq. (2.38), repeated below:

$$\langle \psi^{sc}(\sigma) \rangle = \int_{f=0}^{\infty} \psi_0^{sc}(f) \cdot e^{-g(f,\sigma)/2} df$$

where $\langle \psi^{sc}(\sigma) \rangle$ is the coherent scattering, $\psi_0^{sc}(f)$ the scattering from a similar but perfectly flat surface and $g = k^2\sigma^2 (\cos\theta_1 + \cos\theta_2)^2$.

Equation (2.38) is based on Kirchhoff theory and the assumptions of Gaussian height distribution and Gaussian correlation functions for the surface. The equation says that for a rough surface, high-frequency waves will be less coherently scattered than low-frequency ones. Consequently, less energy will be backscattered for high-frequency waves. Assuming a broad-band or multi-frequency transmitted signal, we get an apparent frequency shift towards lower frequencies as the roughness increases. This was illustrated in Fig. 2.5 (page 26) and can be further studied in e.g. Fig. 5.3 (page 78). The impedance is only appearing in the equation as a constant, contained in $\psi_0^{sc}(f)$, and will not influence the apparent frequency shift.

The apparent frequency shift can be used to determine the roughness of the surface. The backscattered return from a flat surface ($\psi_0^{sc}(f)$) is needed, and the numerical model BORIS has been used for the calculation of this.

The backscattered energy from a surface is determined by both the impedance contrast between the water and sediment, and the surface roughness. Both a lower impedance and a higher roughness will reduce the energy in the coherent part of the scattering. This might be considered as an ambiguity. However, as said above, the apparent frequency shift can be used to estimate the roughness, and then also the amount of energy that would be scattered from a similar but flat seafloor can be found. The reflection coefficient is defined as the scattered pressure divided on the incoming pressure, and can thus also be calculated. The relation between the reflection coefficient and the impedance contrast, for scattering from a flat surface, is given by Eq. (2.6). By taking roughness into account in this way, a more correct impedance estimate is obtained than when only the backscattered energy from a possibly rough surface (and Eq. (2.6)) is used for estimating the impedance.

Figure 4.1 shows a simplified block diagram of the estimation technique. First, some preprocessing is done to the data (Sec. 4.2). Then the apparent frequency shift is found (see below). The energy of the return is also found. From this, roughness and impedance are estimated (Sec. 4.3).

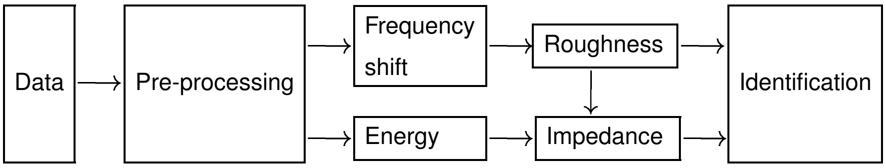

Figure 4.1: *Simplified diagram of the FARIM estimation technique. The estimated roughness is used to obtain a more correct impedance estimate.*

The apparent frequency shift in the data is found by taking the center-of-gravity (CofG) of the power spectrum of the return. As an alternative to the

CofG-method, finding the frequency having equal area on both sides (in the power spectrum) have been tested, but with less success than the CofG. The apparent frequency shift (GofG shift) will later in this report also be denoted the *center frequency shift*.

The details of the estimation technique are described in the next sections. The algorithm is implemented in IDL – Interactive Data Language ([52]).

The implementation is divided into two steps: First the preprocessing of the field data is done separately, and the preprocessed data is stored in a much more convenient and less space-demanding format than the raw-data format[1]. Then the second step is to read the preprocessed data, do calculations, then do the estimation itself, and in the end plot the results in graphs.

4.2 Preprocessing of input data

Some preprocessing is necessary before the field data can be evaluated by the estimation technique.

The raw-data formats that can currently be read by the FARIM software are the TOPAS raw-data format ([53]) and the ADAM format ([6], [24]). In both formats, several pings[2] are stored in one file (usually one file for one survey track), with some information about each ping[3] and then the digitized ping itself.

The different parts of the preprocessing are briefly described in the following list, with some elaboration of important items below.

- The ping headers[3] (information about the pings themselves) are loaded. The pings with an angle less than a 'critical angle' (e.g. 2°) are chosen as 'good' pings. These 'good' pings are loaded into memory.
- A fairly wide bandpass filter is applied to the data (i.e. the 'good' pings). This is just to get rid of some possible noise at very high or low frequencies and avoid aliasing. More filtering is done later in the estimation.
- A bottom detection is done. This is further described in Sec. 4.2.1.

---

[1] The size of the data file is reduced by about a factor 6

[2] A ping is the time response from one transmitted pulse

[3] The structure definitions of the TOPAS raw-data file format are listed in App. B

- A part of each ping (usually 1024 points, out of e.g. 8000) is extracted, around the detected bottom. The extracted part contains more of the trace beyond than before the bottom position, e.g. 100 points before and 924 after.
- The pings (reduced in size) are stored in a binary file, with a supplementary file containing ping-header information, the bottom detections and some other information.

4.2.1 Bottom detection

The bottom detection is done in order to determine the water depth, as well as to obtain reference points so that the traces can be aligned and the stacking be done correctly. The detection needs to be very accurate in order to obtain a coherent and good stacking (typically, an accuracy of a few percent of the characteristic incoming wavelength is needed).

As the roughness increases, the shape of the returned signal is distorted. This needs to be considered in the detection algorithm. Also the transmitted signal shape is of importance. The local conditions of the sea trial can also influence the preferences for a detection method.

The following method has proven to work well with the given field data from the different sites. A faulty detection method is usually easily detected by either inconsistent depth estimates or bad roughness estimates.

1. The first position where the amplitude is higher than a certain percentage (e.g. 20% or 30%) of the maximum amplitude in the trace is detected. This is called *threshold* or *level* detection. A certain time delay can be used before the search is started, in order to avoid e.g. ringing connected to the transmittance of the primary pulse.
2. If wanted, the position of the maximum amplitude within a time-window starting at the first detected position can be found and used as the bottom position. A window width of 1ms is found suitable (the source pulse is typically less than 0.6ms long).
3. For very difficult or distorted data, a median filter can be used in order to get rid of faulty bottom detections.

For a Ricker pulse (Fig. 2.10), steps number 1 and 2 have been used. For a Burst pulse (Fig. 2.12), a better result has been obtained when only step

1 is applied (with a 30% or 40% detection threshold). This is due to the different shapes; a Burst pulse is more easily distorted in a way that reduces the amplitude of the originally highest peak to a level below another peak. The seafloor properties might also influence the choice of detection method.

Step 3 was applied to the Baltic data, where the impedance contrast was very low, the noise high and layering penetrated the surface (see Sec. 6.1.3).

4.3 The estimation process

The estimation process consists of several steps, which will be further described below: First a set of reference data is prepared, using synthetic data and results from theory (Chap. 2). Then further processing of the field data is done, with filtering, stacking, use of a window function to extract the surface return and then calculating center-of-gravity (CofG) and energy. The final step is the estimation of seafloor roughness and impedance, using the reference data set to take into account effects of depth, inclination angle, pulse shape, beam pattern and non-spherical spreading. The different steps are summarized below, with elaborations where necessary.

The creation of reference data is described first. This has to be done only once for a certain vessel or instrument, and only has to be repeated when the system is changed in some way (being recalibrated, new pulse shape is being used, changes to the measurement chain etc.).

- Load synthetic data for scattering from a flat surface, for a range of depths. These synthetic data have been created separately, by running BORIS.

- If necessary, use a transfer function on the synthetic data to simulate the effects the measurement system will have on the field data. This was done during analysis of field data from the MOSAIC cruise (Sec. 6.1.1), where the parametric system was mounted on a buoy.

- Correct for the non-spherical spreading of a parametric source (Fig. 2.14), and the source level of the system, to obtain correct levels.

- Filter the data with a high-pass or band-pass filter. The same filter as applied to the field data is used (see below).

- Calculate reference values for CofG and energy, as a function of depth and roughness, using results from Kirchhoff theory. This is further described in Sec. 4.3.1.

The estimation method itself, including preparation of field data and the necessary pre-processing not done previously, consists of the following:

- Load preprocessed field data, with appropriate information.
- Correct for the hydrophone sensitivity, amplification etc., in order to transfer the data from Volt to Pascal.
- Calculate sailed distance, from the vessel speed and GPS information. The calculation takes into account possible errors in the GPS information. The sailed distance is supplied as a part of the results, and is used as the abscissa in the plots.
- The water depth is calculated, from estimated travel times and speed of sound in water.
- Filter the data with a high-pass (e.g. at 1500Hz) or band-pass filter[4]. For a Burst pulse, using only a part of the spectrum (8-14kHz) was found to give the best results. The same filter is applied to the synthetic reference data.
- Stacking (averaging the aligned time series, at each time step) is then done. A stacking of 5 or 11 time traces has been successfully used.
- A window is applied to the time series, in order to extract the surface part of the return. See Sec. 4.3.2. The exact size of the window is found not to be critical.
- The power spectrum is calculated, and the energy found using Eq. (4.3).
- The CofG (center frequency) of the traces are found, using Eq. (4.2).
- The roughness can then be estimated, by comparing the found CofG with the reference CofG (at the correct depth). The lowest roughness that matches the reference data CofG with the field data CofG is used, such that the roughness might be slightly underestimated but likely not overestimated.

---

[4] A non-recursive digital filter was used, with a filter size of 20 terms and the size of Gibbs phenomena wiggles set to -50dB. Edge-wrapping was applied.

- The impedance is estimated, by comparing the field energy with the reference energy, for the estimated depth *and roughness.* The reference energy might also be corrected for inclination angle[5]. See Sec. 4.3.3.

- The estimated impedance and roughness is presented in the form of plots, either along a survey line (as a function of sailed distance) or in a two-dimensional plot over the survey area with a color code indicating the estimated values.

The computational load involved in the estimation technique is rather limited, and the computations can be done in real time[6]. This is clearly an advantage, since the estimates would be immediately available during a cruise and corrective actions could be taken immediately, if necessary.

4.3.1 Reference values for center-of-gravity and energy

Synthetic data calculated for a smooth surface, and for different depths, are used in the calculation of reference values. First, the power spectrum for the smooth surface, $P^0(d)$, is calculated. Using Eq. (2.32) and Eq. (2.33), the following relation can be found for the theoretical power spectrum, corrected for roughness

$$P_{ijk}(d_j,\sigma_k) = P_i^0(d_j)\cdot \exp\left(-16\pi^2 \frac{f_s^2}{N^2 v_0^2}\cdot \sigma_k^2 \cdot i^2\right) \tag{4.1}$$

where i, j, k are counters for the frequency bin, depth and roughness bin, P_i^0 is the content in frequency bin number i of the power spectrum for a smooth surface, N the number of samples in the time series, v_0 the speed of sound in water, f_s the sampling frequency and σ_k the roughness of bin k. Equation (4.1) is then used for finding $P_{ijk}(d_j,\sigma_k)$.

The center-of-gravity (CofG) frequency, f^{CofG}, can then be found from

$$f_{jk}^{CofG}(d_j,\sigma_k) = \Delta f \cdot \frac{\sum_{i=1}^{N} P_{ijk}\cdot i}{\sum_{i=1}^{N} P_{ijk}} \tag{4.2}$$

---

[5] Angle corrections where done in the analysis of the Horten data.

[6] Currently the estimations, excluding filtering and alignment (which is done separately), takes about 45s for 860 traces, i.e. 0.05s per trace, in an IDL program running on a 200MHz Pentium PC

and the reference energy, $E_{ref}(d, \sigma)$, can be found from

$$E^{jk}_{ref}(d_j, \sigma_k) = 2\frac{N}{f_s}\sum_{i=1}^{N} P_{ijk} \tag{4.3}$$

Equations (4.2) and (4.3) are also used for finding the CofG and energy of the field data.

The reference values are calculated for discrete depths and roughness. The roughness steps are very small, so no further interpolation is done. For the depth-dependence of energy, a 4-coefficient polynomial fit is used to obtain interpolation for the depths estimated from the field data.

4.3.2 Seafloor surface extraction

The part of the time series that stems from the seafloor surface is extracted by use of a discrete window function, which is multiplied with the time series. The window function is a combination of a rectangular window and sinusoidal edges. The window function, $W[n]$, is defined as:

$$W[n] = \begin{cases} 0 & n < 0 \text{ or } n \geq N \\ \frac{1}{2}\left(1 - \cos(\pi\frac{n}{\varepsilon N})\right) & 0 \leq n < \varepsilon N \\ 1 & \varepsilon N \leq n \leq (1-\varepsilon)N \\ \frac{1}{2}\left(1 - \cos(\pi\frac{N-n}{\varepsilon N})\right) & (1-\varepsilon)N < n < N \end{cases} \tag{4.4}$$

where N is the width of the window (in number of samples) and ε is the amount of smoothing. A rectangular window has $\varepsilon = 0$ while a purely sinusoidal window has $\varepsilon = 0.5$. The window is centered around the detected bottom position.

Equation (3.3) (page47) shows the theoretical width of the time window. This equation was used as a starting point for a test of different values. The exact values of the parameters for the window were however found not to be critical. The following values were found suitable and have been used, for a sampling frequency of 100kHz (when a transmitted Ricker pulse is typically less than 30 samples long): $N = 55$, $\varepsilon = 0.2$.

An example of application of the window to field data is shown in Fig. 4.2.

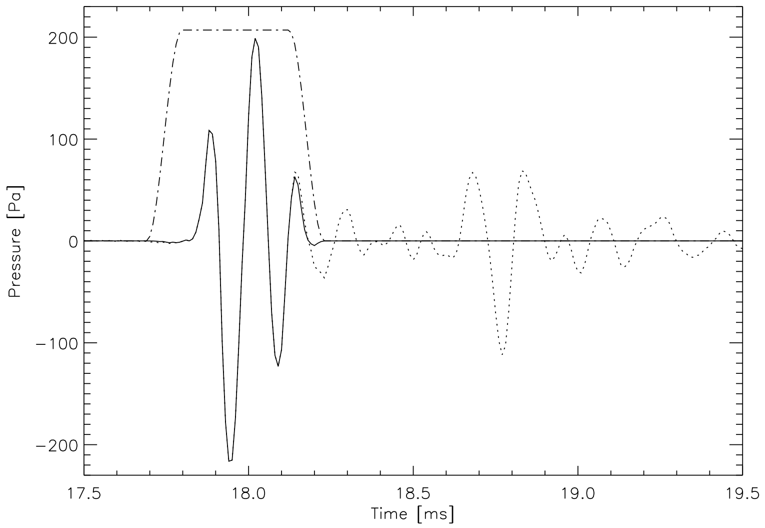

Figure 4.2: *Extraction of the surface part of the signal, by use of a window function. The smoothed window has been applied to field data from a sandy seafloor at Tellaro, in the Mediterranean. The solid line shows the trace after the window has been applied, the broken line shows the original trace. The shape of the window is also shown. The window parameters are:* $N = 55$, $\varepsilon = 0.2$.

4.3.3 Impedance estimation

When estimating impedance, the energy contrast between the energy of the field data, E_{field}, and the reference energy for the estimated depth and roughness[7], $E_{ref}(d, \sigma)$, is used. The impedance is then calculated by

$$Z_{field} = Z_{ref} \cdot \frac{1 + \frac{E_{field}}{E_{ref}} \cdot \mathcal{R}_{ref}}{1 - \frac{E_{field}}{E_{ref}} \cdot \mathcal{R}_{ref}} \tag{4.5}$$

where Z_{field} is the estimated impedance of the field data, Z_{ref} is the reference impedance and $\mathcal{R}_{ref}$ is the reflection coefficient calculated from the parameter values for the reference data set. Equation (4.5) is developed from Eq. (2.6) and assumes plane wave reflection at a plane surface.

---

[7] The reference energy may also be corrected for inclination angle.

4.4 Evaluation for synthetic data

The estimation method has been validated in different ways. In this section the validation for synthetic data is shown. This is done to validate the algorithm and the theoretical approach, as well as studying the accuracy of the approach. Further evaluation is done by sensitivity analysis (Chapter 5) and applying the method to the analysis of field data (Chapter 6).

The synthetic data was generated by BORIS for 15m depth, using beam pattern and pulse shape (Ricker, centered at 8kHz) from the calibration of TOPAS (Sec. 2.6.2, [7]). Table 2.2 (page 39), and corresponding text, give the parameter values for the predefined classes that were used in the simulations.

Figures 4.3-4.4 show the estimated roughness for the predefined classes. 30 traces (from independent simulations with new seafloor and volume realizations) have been used for each mean and standard deviation value for the single traces, while 6 mean-of-5 traces[8] were used for the stacked signals. The figures show that the estimates are good up to a roughness of about 3-4cm, as predicted in section 5.4.1. For a roughness less than 3cm, the mean standard deviation is 15%. It is clearly seen that stacking improves the results. The estimates are closer to the correct values and the standard deviations are smaller. A stacking of 5 traces gives a mean standard deviation of about 5% (for roughness less than 3cm).

Figures 4.5-4.6 show the estimated impedance for the predefined classes, for single and stacked traces. The impedance estimates are in good agreement with correct values, as long as the roughness is well estimated. The standard deviation is 2.3% when the roughness is less than 3cm, and a stacking of 5 traces lowers the standard deviation to about 1%. The sensitivity of the impedance estimates on a correct roughness estimate is clearly seen. E.g, for the classes B1 and B2, the roughness is slightly underestimated while the impedance is more underestimated.

For the classes with a very high roughness, A1, I1 and I2, both the roughness and impedance are heavily underestimated. Note that the standard deviations of the roughness estimates give a very good indication on whether the estimates are good; a high standard deviation clearly indicates an underestimated roughness. This will be further studied in the sensitivity analysis (Chapter 5).

---

[8] By 'mean-of-5' we mean the resulting trace after stacking 5 single traces.

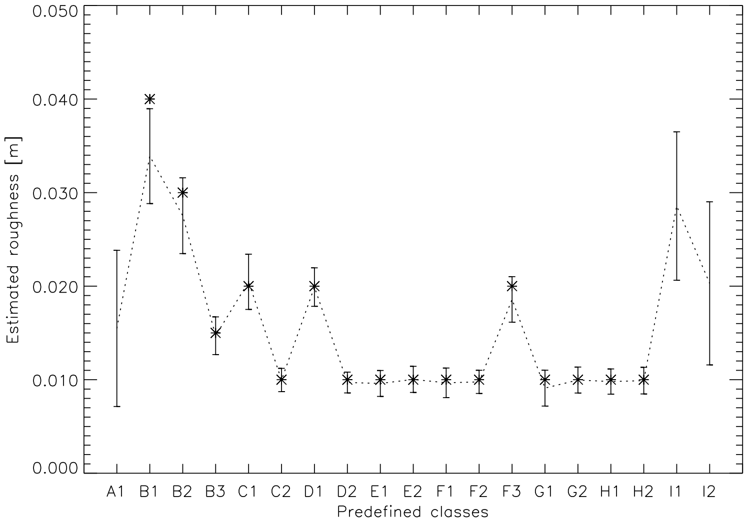

Figure 4.3: *Estimates of the roughness of the predefined classes, using single traces. The error bars denote the standard deviation. The crosses show the correct roughness values. Correct values for classes A1, I1, I2 are [8,6,8]cm.*

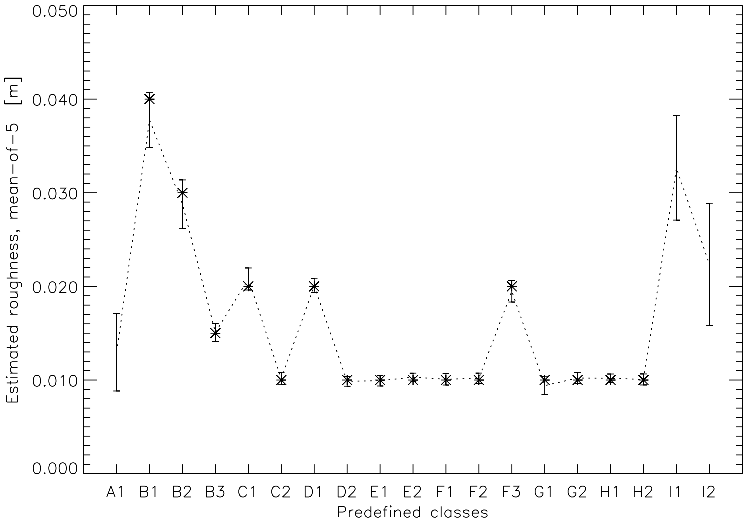

Figure 4.4: *Estimates of the roughness of the predefined classes, using mean-of-5 traces. The error bars denote the standard deviation. The crosses show the correct roughness values. Correct values for classes A1, I1, I2 are [8,6,8]cm.*

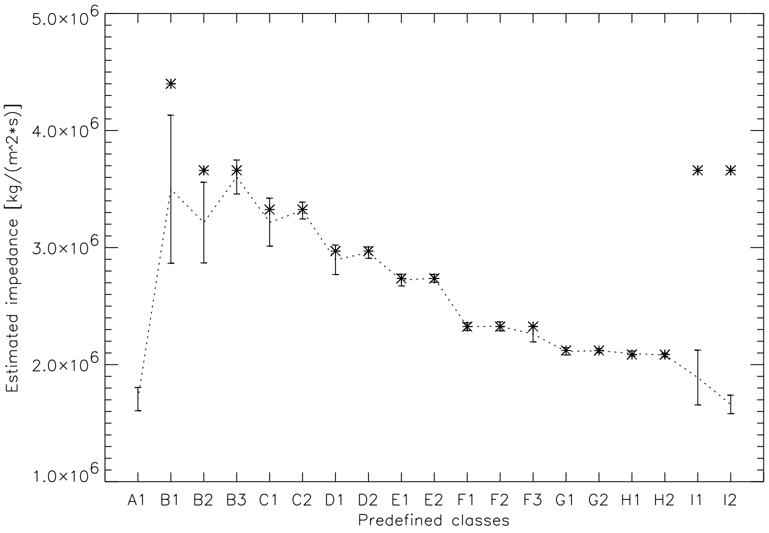

Figure 4.5: *Estimates of the impedance of the predefined classes, using single traces. The error bars denote the standard deviation. The crosses show the correct roughness values. The correct value for class A1 is* $8 \cdot 10^6 kg/(m^2 s)$.

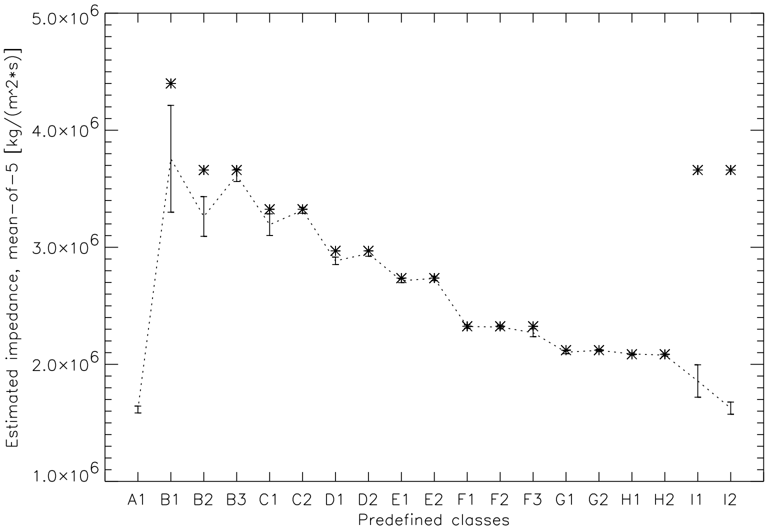

Figure 4.6: *Estimates of the impedance of the predefined classes, using mean-of-5 traces. The error bars denote the standard deviation. The crosses show the correct roughness values. The correct value for class A1 is* $8 \cdot 10^6 kg/(m^2 s)$.

4.5 Limitations of the estimation technique

The limitations of the estimation method are related to the geometry of the problem. The signal needs to be relatively low-frequency (a few kHz is suitable for seafloor roughness of a few cm.), since the method works with the coherent scattered signal only. This also limits the method to near-normal incidence backscattering, although bistatic scattering may also be possible. These limitations might be reduced by including in the estimation technique the effects of the diffuse scattering (Sec. 2.4.4). Another possibility is to use different parts of the frequency band for characterizing different seafloor roughness.

Since the difference in roughness sensitivity at different frequencies is utilized for the estimation, a wide-band pulse (or several frequency bands) is needed. The beam should preferably be relatively narrow so that the response from the volume and surface can be separated.

Bottom penetrating parametric sonars seem to satisfy these demands very well (Sec. 2.6), and currently seems to be the best instrument to use with this characterization technique.

Chapter 5

Sensitivity analysis

5.1 Introduction

The purpose of this chapter is to do a sensitivity analysis of the parameters of the mathematical model. This is done both analytically and numerically. The sensitivity analysis is expected to increase the understanding of the physical processes as well as to aid in the development of suitable classification/characterization algorithms. The accuracy and validity regimes of the algorithms will also be investigated.

One advantage of doing a sensitivity analysis on a mathematical model instead of using experiments is that it is much easier to isolate the effects of the different parameters. It may also be a lot cheaper and less time-consuming. Disturbing elements like uncertainty in parameter values, noise etc., are eliminated. Of course, the numerical model itself has to be verified against the real world. Such a verification has been done in [10] and [9], which concludes that the numerical model BORIS appears to predict well the scattering from the seafloor interface and volume. Doing a sensitivity analysis through experiments would be beneficial, but has not been prioritized in this report.

The method that has been used for the sensitivity analysis is to change one parameter value at a time while running the model. The numerical model being used to provide synthetic data has been BORIS (Sec. 2.5). The morphological parameter surface RMS height, σ, is important, and the effect of changing it is not easily predictable, so the model has usually been run for several values of the RMS roughness for each parameter to be studied. The results are usually presented through the following features:

- Shape of the echo return (i.e. pressure as a function of time).
- Shape of the power spectrum.
- Apparent frequency shift, shown as Center-of-gravity (CofG) of the power spectrum, as a function of seafloor surface RMS height.
- Energy of the return, as a function of seafloor surface RMS height.

The shapes of echo return and power spectra are only shown in some occasions. The choice of these features was based on knowledge of the physical processes (Chapter 2). These features should be well suited to represent the changes in the calculated return due to changes in the model parameters, and at the same time being insensitive to statistical variations. Emphasis has been put on the surface return (and not the volume contribution), as this is most important in the estimation technique. If nothing else is noted, the total signal (surface plus volume contribution) is used in the results presented.

The use of Kirchhoff theory for estimating the RMS roughness relies on the coherent part of the backscattering. The backscattered signal from a rough surface consists of both coherent and incoherent (diffuse) scattering, but the incoherent part may be reduced by stacking[1] of the data. In the figures, results from the use of both single and stacked data are presented. An impression of the strength of the diffuse field compared to the coherent field is then obtained, as well as an indication of how much stacking is necessary when using the estimation technique on field data.

5.1.1 Parameters of the model

The numerical model contains several parameters, described below. For convenience they have been grouped logically.

Geoacoustical parameters:

- Speed of sound in water and seafloor, v_0 and v_1 ($[m/s]$).
- Density of water and seafloor, ρ_0 and ρ_1 ($[g/cm^3]$).
- Pressure wave attenuation in the seafloor, β ($[dB/m]$).

---

[1] Averaging of aligned time series, at each time step. In the figures the stacked traces are denoted by e.g. 'Mean-of-10', when a stacking of 10 traces has been applied.

Morphological parameters:

- Surface RMS height, σ ($[m]$).
- Volume inhomogeneities factor, μ ($[-]$).
- Parameters determining the roughness field of the surface (see Sec. 5.4.2).
- Parameters determining the statistics of the variation of sound speed and density in the volume (see Sec. 5.4.2).

Geometrical parameters:

- Pulse shape (e.g. Burst, Ricker, FM; shape of spectrum, width and center frequency are important parameters) and source level.
- Beam pattern (shape and width).
- Water depth.
- Pitch, roll (and/or bottom slope), position.
- Sampling frequency.

Numerical parameters:

- Start and stop angle for roll and pitch (used when truncating the beam pattern).
- Surface patch length and sampling interval.
- Volume patch length and sampling interval, bottom penetration depth.
- The BORIS seed – for using the same realization of the seafloor for several runs of the model.

For a real seafloor, other parameters might be quite important as well. Seafloor slope and undulations, very high roughness, gas content and layering are a few examples. These effects have not been included in the sensitivity analysis, but are being discussed in several occasions throughout the report.

5.1.2 Outline of the chapter

The different sensitivity analysis are treated according to the above grouping, with figures and discussions in the sections. Summary and final conclusions are presented at the end of the chapter.

The starting point of most of the sensitivity analysis is a sandy seafloor, class C2 as defined in Table 2.7 (page 39). Normally the measured beam pattern and Ricker pulse (centered at 8kHz) of the SACLANTCEN TOPAS PS040 has been used as input (Sec. 2.6.2, [7]). The depth is usually fixed at 30m, small enough to be representative at shallow waters and large enough to avoid most near-field effects. Computing loads and memory demands increase with depth, this also contributed to the choice of depth.

The figures of traces and power spectra contain several traces or spectra in each figure, and the RMS roughness value for the respective curve is then often given on the right hand side of the figure. For the figures of energy and center frequency shift, error bars showing one standard deviation are commonly used[2].

5.2 Sensitivity to numerical parameters of BORIS

A sensitivity study of the numerical parameters of BORIS has been done. The purpose was to establish regimes of validity of the numerical parameters, such that numerical effects on the physical modeling would be minimized at the same time as computing time and memory demands were kept within reasonable limits. The parameters studied were the surface sampling interval, surface patch length, volume sampling interval, volume patch length and bottom penetration depth. The test involved running BORIS on the predefined class C2 (sand), while varying the numerical parameters, one at a time. This study is described in Appendix A.1.

The main reason for the study was, as mentioned, to determine suitable values for the numerical parameters so that possible numerical effects were minimized. This was achieved. The parameter sets gained from this sensitivity study were used when running the numerical model in the rest of the work described in this report.

---

[2] The standard deviation is usually calculated from 30 single values.

5.3 Sensitivity to geoacoustical parameters

The sensitivity of the numerical model to the geoacoustical parameters (v_0, v_1, ρ_0, ρ_1, β) can be found analytically. This is described in Chapter 2, from which some findings are repeated below.

The reflection strength from the seafloor surface was found to be proportional to the reflection coefficient, $\mathcal{R}_{01}$, which is dependent upon the impedance contrast (Z_1/Z_0) between sediment and water. The relation between impedance contrast and the reflection coefficient is however non-linear. See Fig. 2.2 (page 11). This means that impedance estimates should, in principle, be more accurate at low impedances. However, other factors could influence this. E.g., gas bubbles might be present in loose sediments (with low impedance) but is not included in Kirchhoff theory and could make the estimates less accurate.

The attenuation in the sediments leads to a decreasing field into the sediments, thus a weaker return as a function of time. The frequency content is also changed, as the higher end of the spectrum is more attenuated than the lower end in the sediments.

The numerical model has been tested for sensitivity to the geoacoustical parameters, and was found to conform well to the analytical evaluation. This was as expected.

5.4 Sensitivity to morphological parameters

The morphological parameters are the surface RMS height, σ, volume inhomogeneities factor, μ, the roughness field of the surface and the statistical parameters describing the changes in sound speed and density in the volume.

The surface RMS height is the most important parameter here, and will be discussed below. A sensitivity analysis of the parameters of the roughness field is also presented.

The amplitude of the volume return is proportional to the volume inhomogeneities factor μ (Chapter 2), and μ is therefore not further investigated here. The focus of the sensitivity analysis has been on the surface return, and the statistical parameters of the volume have therefore not been investigated. The volume return is mostly incoherent, so the phase information would probably not be as interesting as the amplitude and power spectrum. In addition, frequency as a function of time (using e.g. Short-Time Fourier analysis, wavelet analysis or Hilbert techniques ([41])) is interesting, as this can be useful in finding the attenuation of the sediments (Section 2.3).

5.4.1 Surface RMS height, σ, and the effect of stacking

The effect of surface RMS height is important, and will be studied in several contexts during the sensitivity analysis. In this section we discuss the main effects of the RMS height, while some details will be treated later, where appropriate. The effect of stacking will also be investigated.

Theory (Chapter 2) predicts the behavior of the coherent part of the signal as a function of RMS roughness. Essentially, with the chosen roughness distribution, the amplitude of the coherent signal will decrease exponentially with increasing roughness. The incoherent part of the return will increase as the roughness increases, and there will be a statistical variation in energy and power spectrum between different pings. This behavior, and the importance of it, is studied here. The volume contribution is mostly incoherent.

The incoherent part of the signal, for both surface and volume, might be significantly decreased by stacking. The coherent part is preserved and unchanged during this stacking. The reduction of the incoherent part of the signal is proportional to the degree of stacking, i.e. a stacking of 10 traces reduces the incoherent energy to 1/10. This has been confirmed numerically.

The synthetic data used for the surface RMS height sensitivity analysis were generated by BORIS at 30m depth, using the beam pattern and pulse shape from the calibration of TOPAS([7]).

Figure 5.1 shows traces from class C2, sand, as a function of RMS roughness, both for single and mean-of-10 traces (i.e. 10 traces are stacked). It should be noted that the traces are normalized[3], the amplitude does decrease rapidly with increasing roughness (see Fig. 5.5). The shapes of the traces are distorted when the roughness increases, but the mean-of-10 traces are less influenced, as expected.

Figure 5.2 shows power spectra of traces from the same class. The surface and volume return are shown separately (as opposed to showing the total signal, as in most other figures). The surface return, which is much stronger than the volume return, exhibits an apparent frequency shift towards lower frequencies as the roughness increases and the higher frequency components are more scattered away from specular direction. This is consistent with theory. The

---

[3] The traces are normalized with respect to maximum amplitude, to improve presentation

volume return is rather inconsistent and irregular. It does not show any apparent frequency shift or increased distortion as the RMS height increases. This is not surprising, since the volume return consists of incoherent scattering.

Figure 5.3 shows power spectra of traces from the same class as Fig. 5.2, but with total signals and stacked total signals. Again, the spectrum becomes very distorted when the roughness increases, but the stacked data is less influenced and the apparent frequency shift is much more obvious then for non-stacked data. The effect of stacking is very significant unless the roughness is very low and most of the return is coherent anyway.

Figure 5.4 shows the center-of-gravity (CofG) for power spectra of both single and mean-of-10 traces, as a function of RMS roughness. The total signal and the volume contribution is shown separately. The similar plot for only the surface signal looks almost exactly like the one for the total signal. The theoretical return from a rough surface (only considering the coherent part of the return) is also included in the figure. The theoretical curve fits well with the simulated data at low roughness, where most of the return is from the coherent scattering. At higher roughness the relative importance of incoherent return increases, leading to a higher CofG than predicted by theory. These results indicate that, at least for stacked data, the proposed estimation method is accurate up to a few centimeter of RMS roughness, assuming that a broadband pulse with a center frequency of a few kHz is used (as for the Simrad TOPAS PS040).

The CofG in the volume is seen in Fig. 5.4 to always be higher than the CofG in the surface, and decreases less as a function of roughness. The energy of the volume is also decreasing less than the energy of the surface as a function of roughness ($\Delta E_{volume}^{\sigma:0\rightarrow 10cm} \sim -15dB$, $\Delta E_{surface}^{\sigma:0\rightarrow 10cm} \sim -25dB$). This means that the volume contribution 'lifts' the total CofG, especially at high roughness. This may lead to underestimated RMS roughness and impedance. This is more important when the volume return is relatively high compared to the surface return, and the effect is expected not to be significant in most cases.

Figure 5.5 shows the energy of the total return, for varying seafloor RMS roughness, both for single and mean-of-10 traces. The curves for mean-of-10 are very close to the theoretical curve, showing that at this amount of stacking very little of the energy comes from the incoherent contribution. The energy from the volume is low for sand (class C2) and does not contribute much to the total energy. These figures suggest that the impedance estimates have a good accuracy for a wide range of roughness, assuming, of course, that the RMS roughness estimates used for the impedance estimation are accurate.

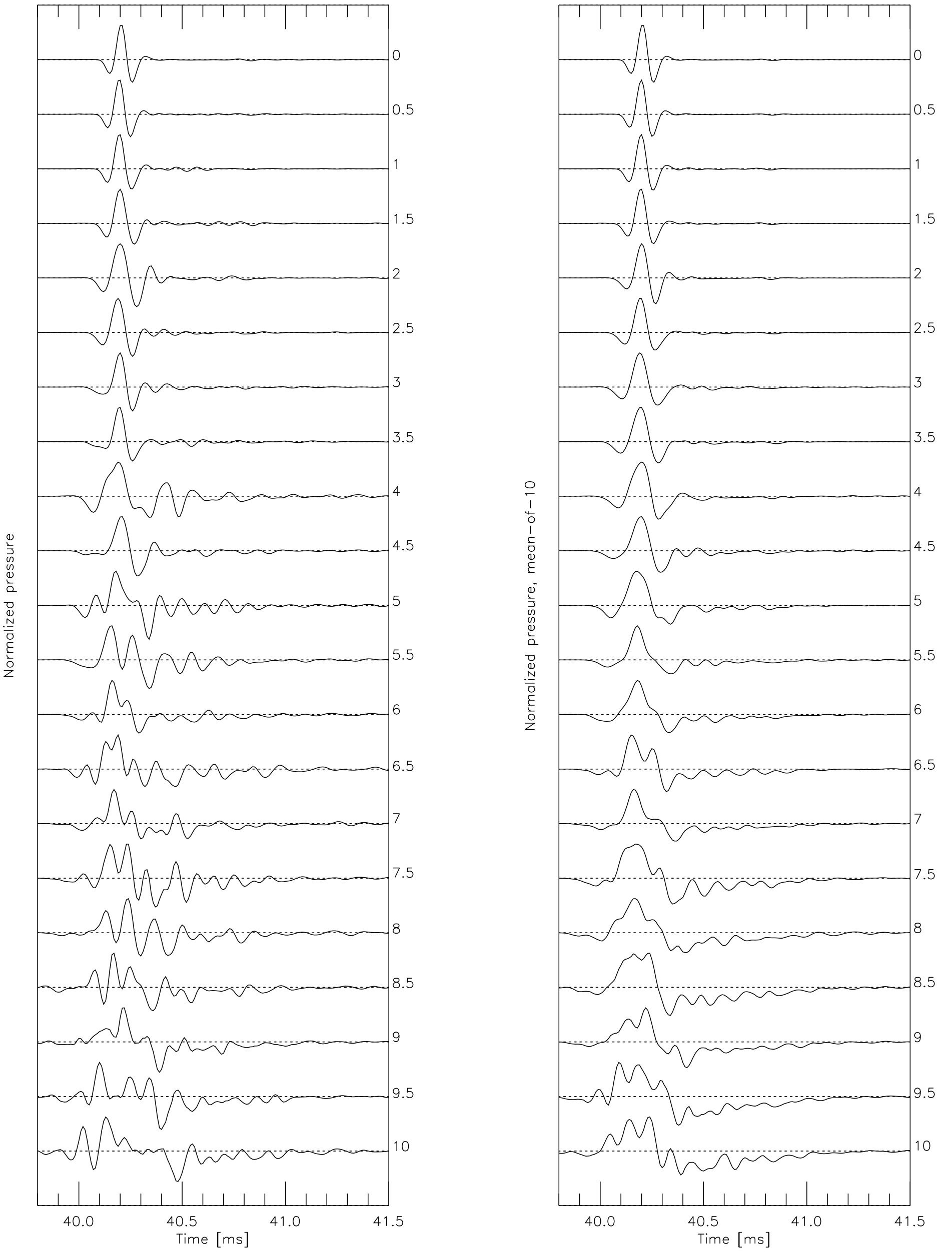

Figure 5.1: *Normalized traces from class C2, shown for different values of RMS roughness [cm]. The left figure shows single traces while the right one shows mean-of-10 traces.*

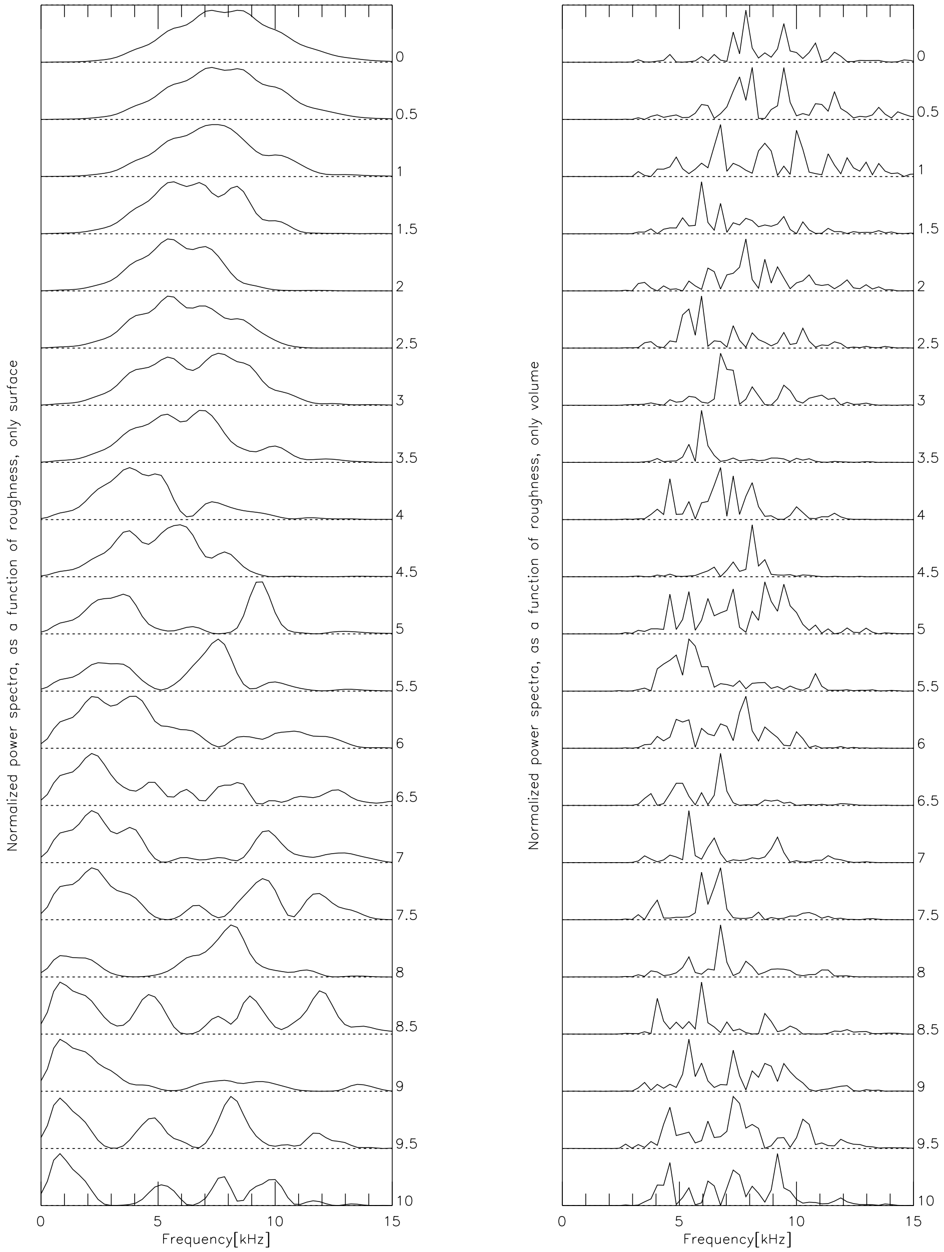

Figure 5.2: *Normalized power spectra from class C2, shown for different values of RMS roughness [cm]. The left figure shows the surface response, the right one shows the volume response.*

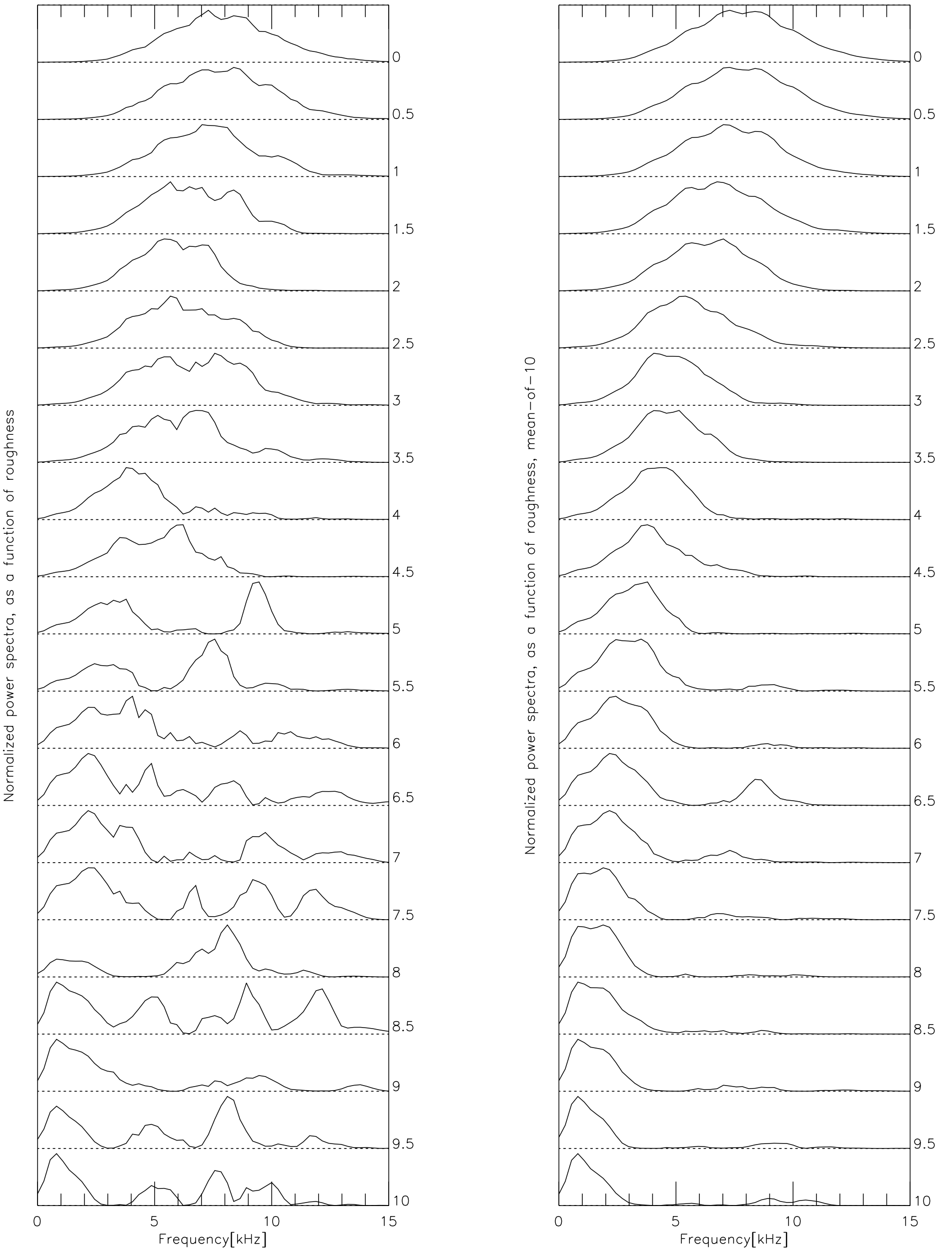

Figure 5.3: *Normalized power spectra from class C2, shown for different values of RMS roughness [cm]. The left figure shows single traces while the right one shows mean-of-10 traces.*

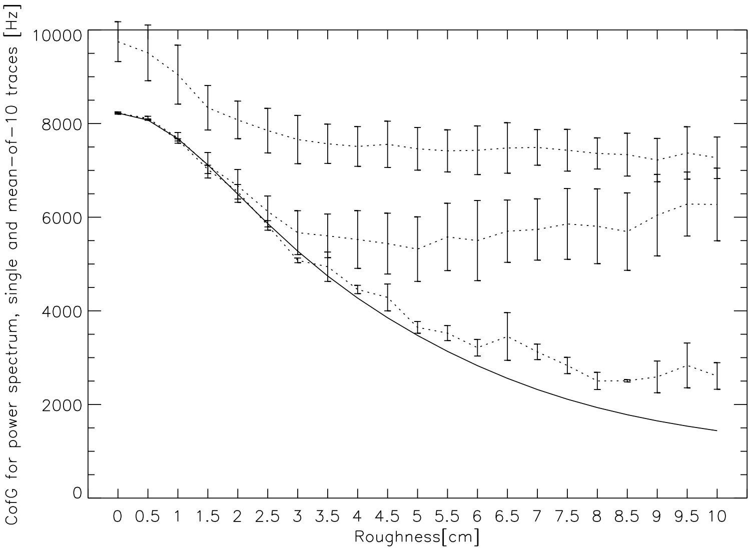

Figure 5.4: *Center of gravity for power spectra, in frequency, as a function of RMS roughness. Single and mean-of-10 traces (lowest dotted line). The volume contribution (single traces) is shown in the uppermost curve. Theoretical CofG is shown as a solid line. The error bars denote the standard deviation.*

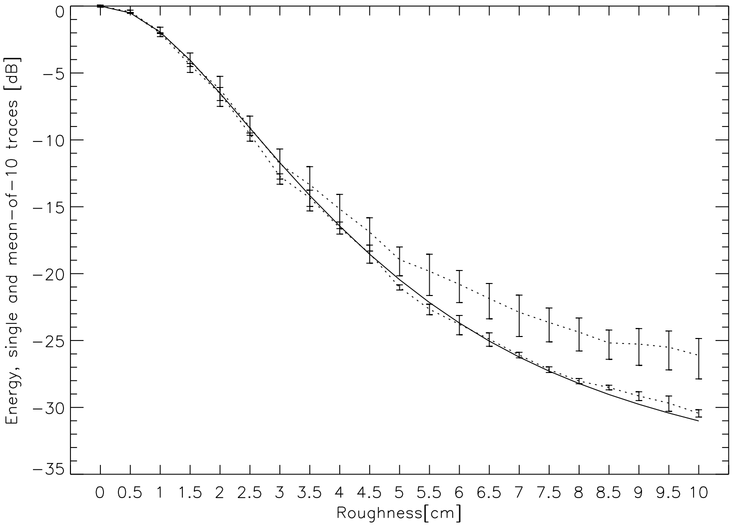

Figure 5.5: *Energy of class C2 (sand), as a function of RMS roughness. Single and mean-of-10 traces (lowest dotted line). Theoretical energy is shown as a solid line. The error bars denote the standard deviation.*

This section has verified that the effect of roughness is significant. The study indicates that RMS roughness can be well estimated if it is not too large compared to the transmitted wavelength. RMS roughness up to a few centimeters can be estimated when using a Ricker pulse centered at 8kHz, with no or limited stacking. Energy, and thereby seafloor impedance, can be estimated with a high accuracy if the RMS roughness estimates are accurate. Stacking significantly improve the estimates of both RMS roughness and impedance, at least for moderate or high roughness. Stacking also increases the maximum roughness that can be estimated.

5.4.2 The surface height spectrum

Introduction

The effects of the parameters determining the generation of the surface roughness field of the seafloor are investigated here. Section 2.4.4 showed that, according to Kirchhoff theory and the assumptions taken, only the roughness RMS height σ influences the coherent scattering, while for the diffuse scattering also the horizontal correlation length λ_0 matters. This assumes specification of the roughness spectrum through a Gaussian correlation function. BORIS uses a power law for the wave number instead, but also here the horizontal variation of the surface will influence the diffuse scattering.

The seafloor generation in BORIS is described in Sec. 2.5.3. A band-passed power law spectrum is used (Eq. 2.44) and is repeated below:

$$\begin{aligned} W_s(\mathbf{K}) &= \eta \mathbf{K}^{-\nu} && if \quad K_{hp} < K < K_{lp} \\ &= 0 && if \quad K \leq K_{hp} \\ &= 0 && if \quad K \geq K_{lp} \end{aligned}$$

K is a two-dimensional wave vector with magnitude equal to the wave number K. K_{hp} and K_{lp} are the high-pass and low-pass wave-numbers, respectively, η is a normalization factor and ν is related to the fractal dimension of the spectrum ($2 < \nu < 4$, Sec. 2.4.3).

In practice, the upper limit of the wave vector is ultimately determined by the limits of resolution and sampling interval of the measurement method [47, page 28]. The lower limit is determined by the sample size taken; wavelengths longer than the sample size will never be measurable. E.g., an illuminated circle with a radius of 3m (e.g. a TOPAS beam at 50m depth) would give a lower limit of $K_{hp} \sim 1 rad/m$ (where $K = 2\pi/\lambda$).

Table 5.1 shows the parameter values that have been used in this study, together with the name tag used in the plots and the file tag used in the saved files (including plot files). In the study, each of the parameters have been changed, one at a time, to isolate their effects. The reference values have been used for all other generation of synthetic data in this report.

Name	Filter values (surface)			Comment	File
tag	ν [1]	K_{hp} $[rad/m]$	K_{lp} $[rad/m]$		tag
Reference	4.0	10	30	Reference	1030
HP1	4.0	1	30	K_{hp} changed	130
HP5	4.0	5	30	K_{hp} changed	530
LP100	4.0	10	100	K_{lp} changed	10100
Exp3	3.0	10	30	ν changed	3

Table 5.1: *Filter values (surface)*

Results and observations

Figures 5.6-5.10 show the energy of the traces, as a function of RMS roughness, for the different sets of parameters. Both single and mean-of-10 traces are shown. The energy in the curves are normalized by adding 39dB to the energy. Figures 5.11-5.15 show the center frequency shift (in the way of center-of-gravity (CofG)), as a function of RMS roughness, for the different sets of parameters. Figures 5.16-5.21 compare CofG and energy for the different parameter sets.

Some observations have been done from these figures, and are presented below:

The surface:

- The effect of changing the exponential factor, ν, which accounts for the decay of the power spectrum, is very small. (Cf. Fig. 5.6 vs. Fig. 5.10, Fig. 5.11 vs. Fig. 5.15, see Figs. 5.16-5.21.)
- A change in the high pass filter wave number, K_{hp}, has a significant effect on the energy and center frequency shift. A lower K_{hp} leads to less decrease in the CofG as roughness increases. For $K_{hp} = 1rad/m$ ($\equiv$ λ_{hp} =6.3m), the decrease is so small that an estimate of RMS roughness would be difficult to achieve. The energy decreases significantly less with roughness when K_{hp} is low, and this could easily influence the estimation of impedance. The standard deviation of both energy and CofG increases when K_{hp} is low. (Cf. Fig. 5.6 vs. Figs. 5.7-5.8, Fig. 5.11 vs. Figs. 5.12-5.13, see Figs. 5.16-5.21.)

  The sonar is not sensitive to very large roughness wavelengths. In practice, the limit is approximately when the roughness wavelength is comparable to the beam width. The width of the Topas beam at -3dB and 30m depth is 1.8m and the roughness wavelengths corresponding to $K_{hp} = [1, 5]$rad/m are $\lambda_{hp} = [6.3, 1.3]$m. The sonar will then not be sensitive to parts of the roughness spectrum, and the seafloor will look smoother than it actually is. This corresponds with the observations made above.
- A change in the low pass filter wave number K_{lp} gives only a small effect on the energy and center frequency shift, the effect being that both the energy and CofG decrease slightly more with increasing roughness, thus makes them follow the theoretical curve slightly better. Since the power law spectrum W_s is exponential, a change in K_{lp} does not influence the

total surface shape much, it just adds some high frequency components. This can explain the low sensitivity to changes in K_{lp}. (Cf. Fig. 5.6 vs. Fig. 5.9, Fig. 5.11 vs. Fig. 5.14, see Figs. 5.16-5.21.)

The volume:

- The energy in the volume return decreases ~15dB when the RMS roughness increases from 0 to 10cm, while the energy in the surface return decreases ~25dB (cf. Figs. 5.17 and 5.20). This means that a high volume return will influence the estimates more when the roughness is high.
- For zero roughness and a sandy seafloor (C2), the energy of the surface is 30dB higher than the volume. (cf. Figs. 5.17 and 5.20).
- For low K_{hp} the decrease of the energy in the volume is only $\sim 4 - 8$dB when the roughness increases from 0 to 10cm. When K_{hp} is low, there is a larger part of low frequencies in the surface spectrum, leading to less scattering away from specular direction. This cause the scattering from the volume (as from the surface) to decrease less as the roughness increases, as observed (cf. Figs. 5.20-5.21).
- The CofG of the volume is very little affected by a change in ν or K_{lp}. A low K_{hp} gives a smaller reduction of the CofG as the roughness increases (cf. Fig. 5.20). This seems reasonable since the surface scattering and consequently the transmission then is less influenced (due to a larger part of low frequencies in the surface spectrum) and the volume scattering is incoherent.
- The standard deviation for the CofG is about 500Hz, and for the energy it is about 2dB (cf. Figs. 5.20-5.21). The standard deviation is almost independent of RMS roughness and the surface parameters, although a low K_{hp} leads to slightly higher standard deviations. This seems reasonable, considering that the volume scattering is incoherent.

Conclusions

Sensitivity analysis of the parameters of the surface height spectrum has been studied in this section. The effects of changing the parameters K_{lp} and ν were found to be small, and negligible in many contexts. The effect of changing K_{hp} however are large, and might significantly affect the estimation of RMS roughness and impedance.

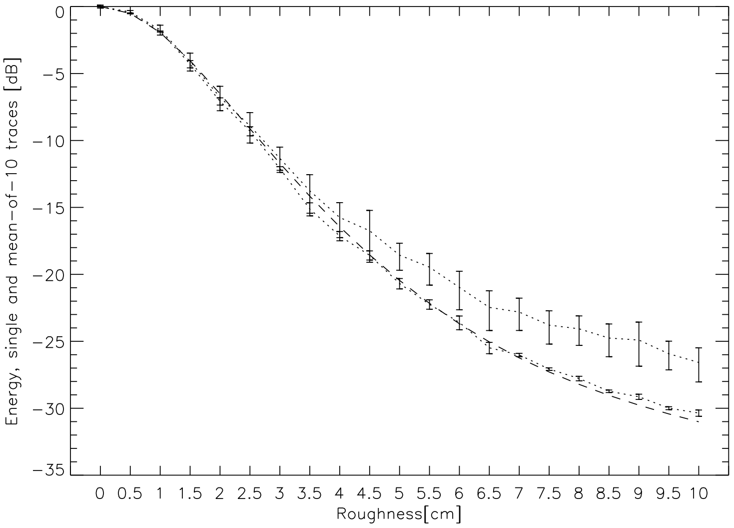

Figure 5.6: *Energy of class C2 (sand), as a function of RMS roughness. Single and mean-of-10 traces are shown. Theoretical energy is shown as a dashed line. Reference values, i.e.* $K_{hp} = 10 rad/m$, $K_{lp} = 30 rad/m$, $\nu = 4$.

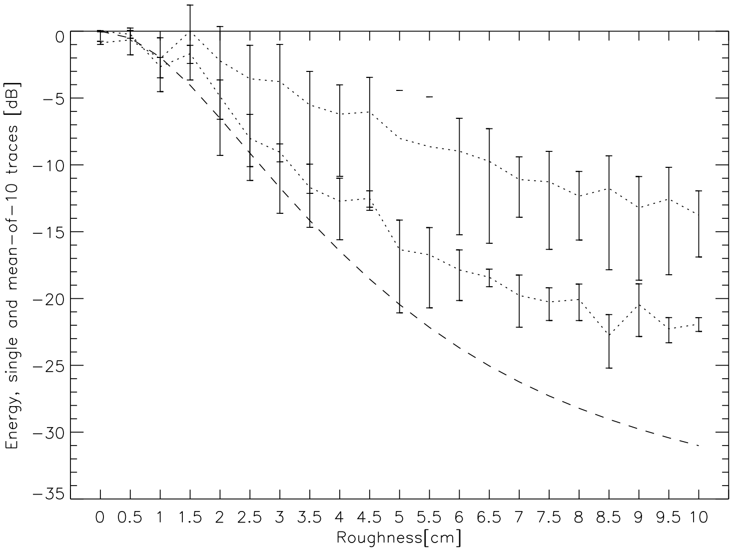

Figure 5.7: *Energy of class C2 (sand), as a function of RMS roughness. Single and mean-of-10 traces are shown in the upper and lower curves, with standard deviations. Theoretical energy is shown as a dashed line.* $K_{hp} = 1 rad/m$.

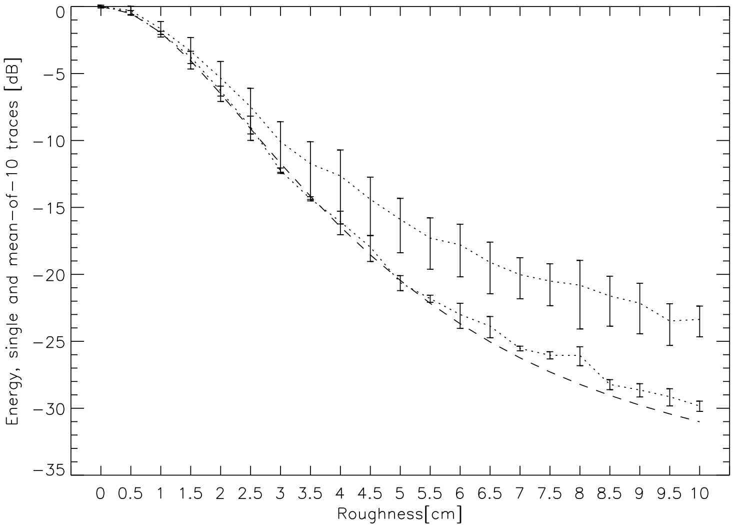

Figure 5.8: *Energy of class C2 (sand), as a function of RMS roughness. Single and mean-of-10 traces are shown in the upper and lower curves, with standard deviations. Theoretical energy is shown as a dashed line.* $K_{hp} = 5 rad/m$.

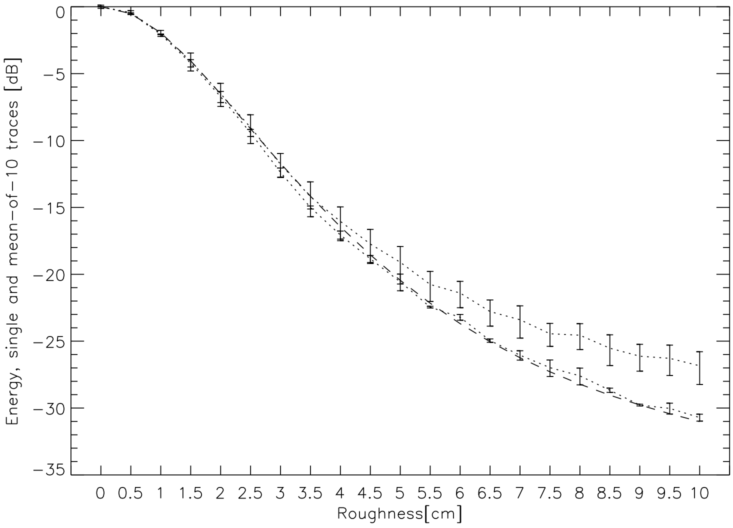

Figure 5.9: *Energy of class C2 (sand), as a function of RMS roughness. Single and mean-of-10 traces are shown in the upper and lower curves, with standard deviations. Theoretical energy is shown as a dashed line.* $K_{lp} = 100 rad/m$.

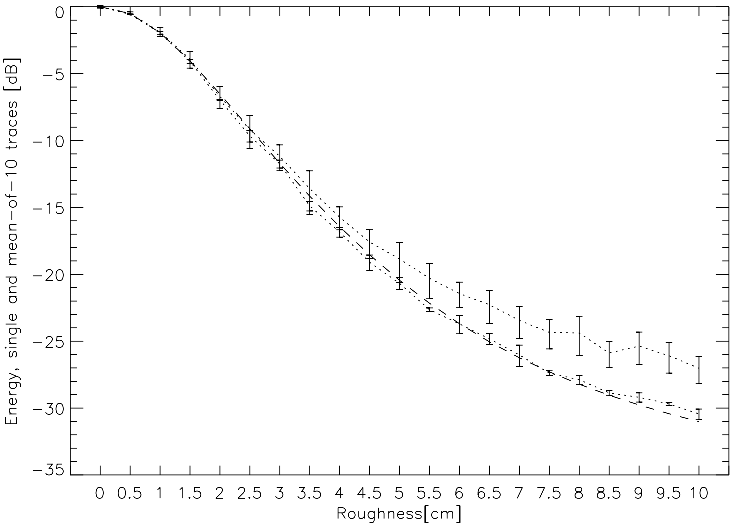

Figure 5.10: *Energy of class C2 (sand), as a function of RMS roughness. Single and mean-of-10 traces are shown in the upper and lower curves, with standard deviations. Theoretical energy is shown as a dashed line.* $\nu = 3$.

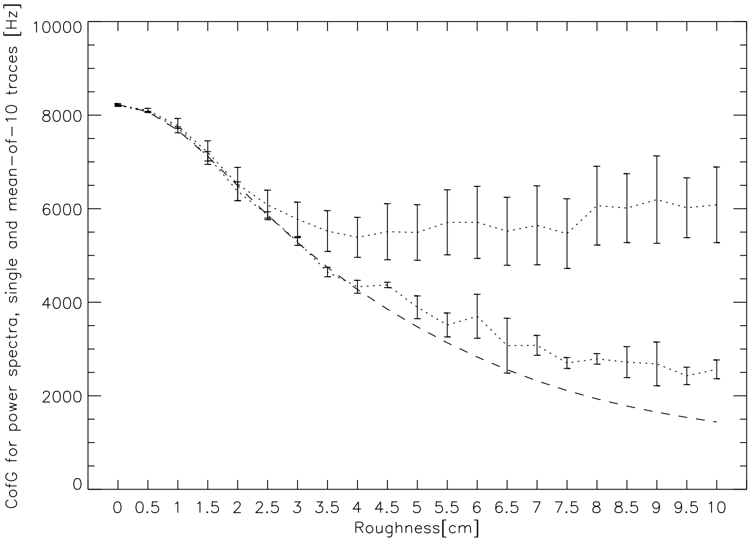

Figure 5.11: *Center of gravity for power spectra, in frequency, as a function of RMS roughness. Single and mean-of-10 traces. Theoretical CofG is shown as a dashed line. Reference values, i.e.* $K_{hp} = 10rad/m$, $K_{lp} = 30rad/m$, $\nu = 4$.

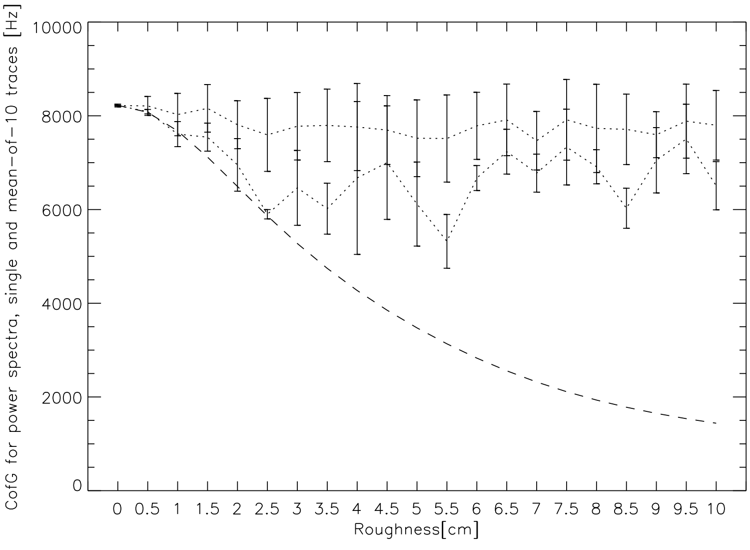

Figure 5.12: *Center of gravity for power spectra, in frequency, as a function of RMS roughness. Single and mean-of-10 traces. Theoretical CofG is shown as a dashed line.* $K_{hp} = 1rad/m$.

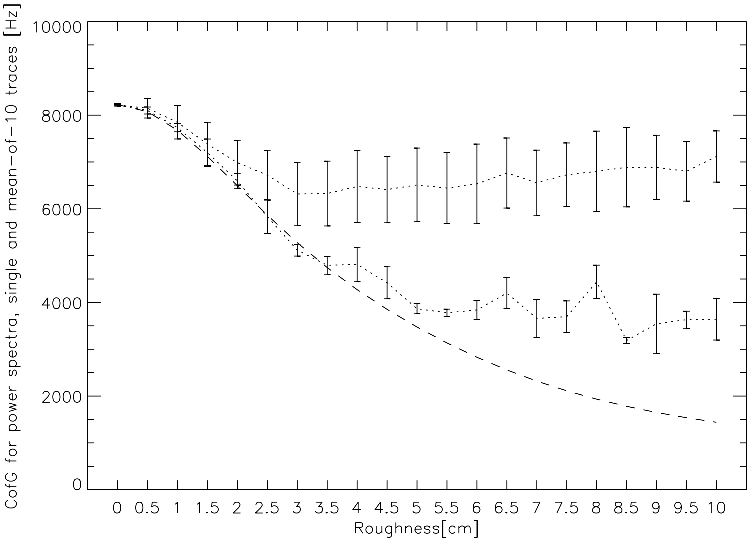

Figure 5.13: *Center of gravity for power spectra, in frequency, as a function of RMS roughness. Single and mean-of-10 traces. Theoretical CofG is shown as a dashed line.* $K_{hp} = 5rad/m$.

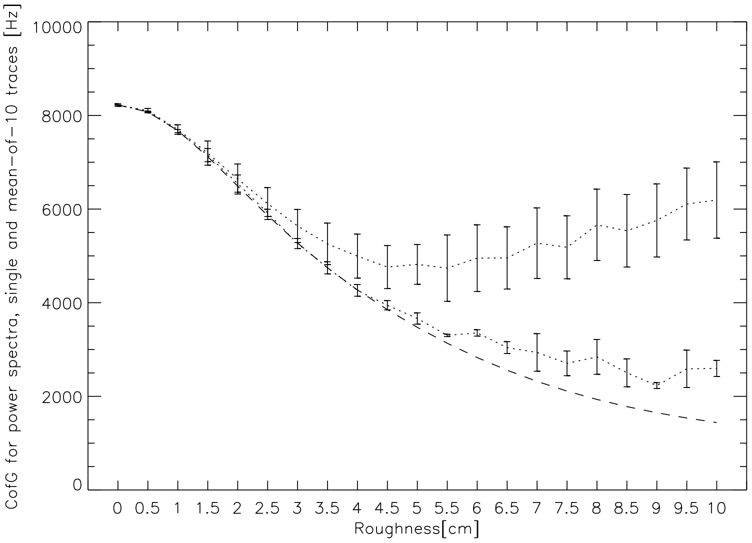

Figure 5.14: *Center of gravity for power spectra, in frequency, as a function of RMS roughness. Single and mean-of-10 traces. Theoretical CofG is shown as a dashed line.* $K_{lp} = 100 rad/m$.

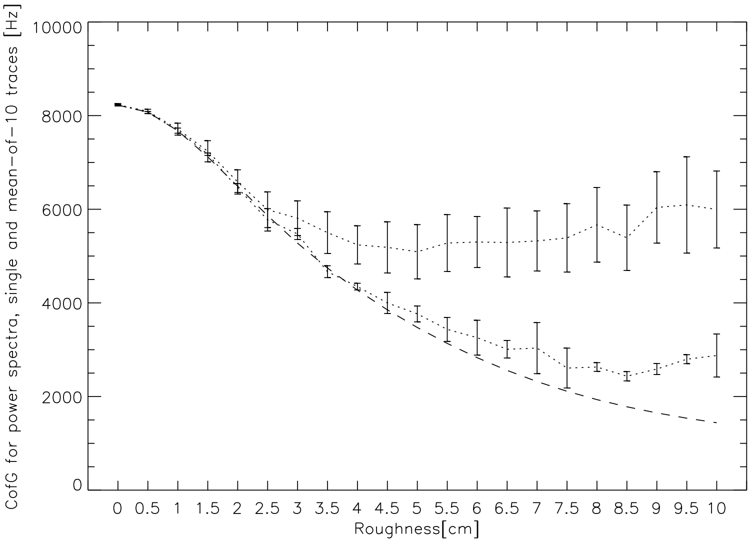

Figure 5.15: *Center of gravity for power spectra, in frequency, as a function of RMS roughness. Single and mean-of-10 traces. Theoretical CofG is shown as a dashed line.* $\nu = 3$.

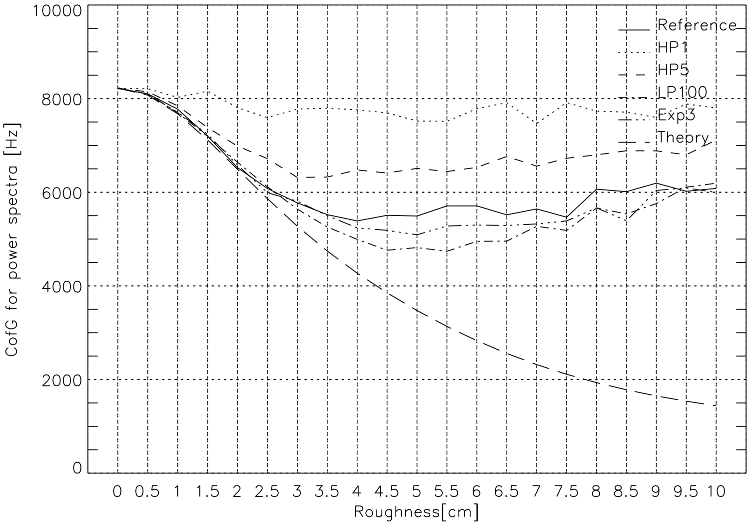

Figure 5.16: *Mean center of gravity for power spectra, in frequency, as a function of RMS roughness, for different parameters (see the legend, and Table 5.1 page 81). Single traces.*

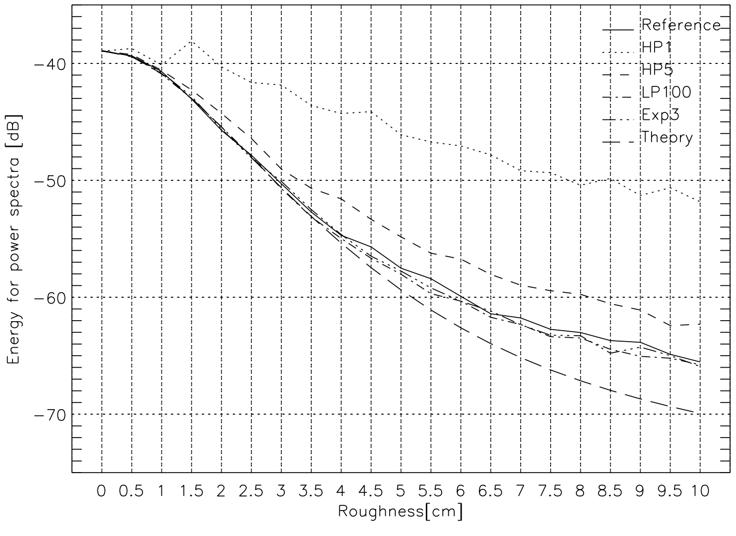

Figure 5.17: *Mean energy, as a function of RMS roughness, for different parameters (see the legend, and Table 5.1 page 81). Single traces.*

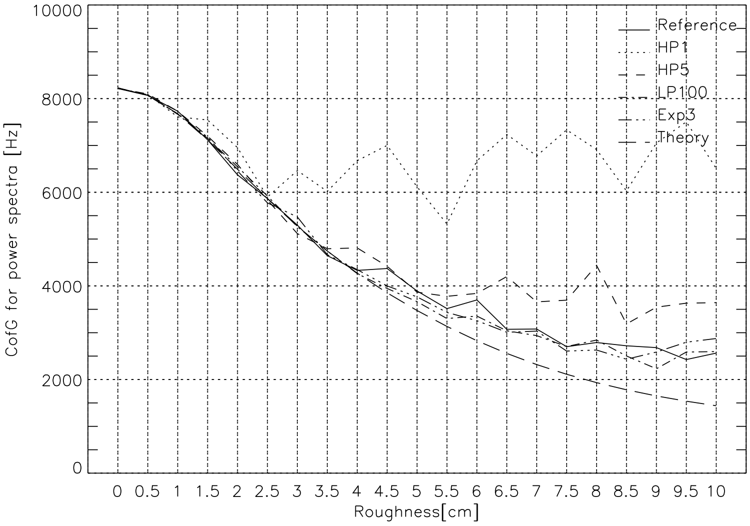

Figure 5.18: *Mean center of gravity for power spectra, in frequency, as a function of RMS roughness, for different parameters (see the legend, and Table 5.1 page 81). Mean-of-10 traces.*

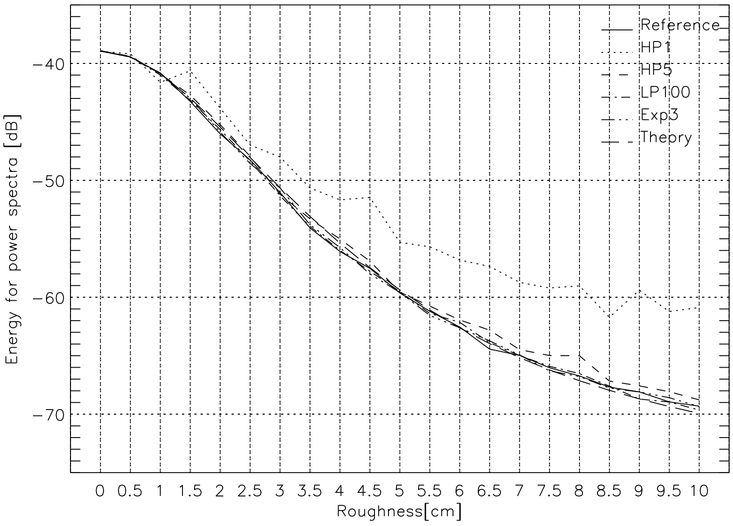

Figure 5.19: *Mean energy, as a function of RMS roughness, for different parameters (see the legend, and Table 5.1 page 81). Mean-of-10 traces.*

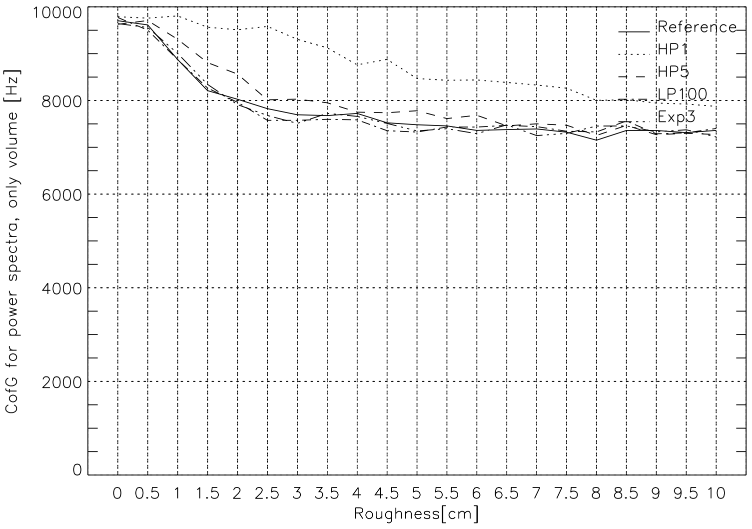

Figure 5.20: *Mean center of gravity for power spectra of the volume, in frequency, as a function of RMS roughness, for different parameters (see the legend, and Table 5.1 page 81). The standard deviations are all around 500Hz.*

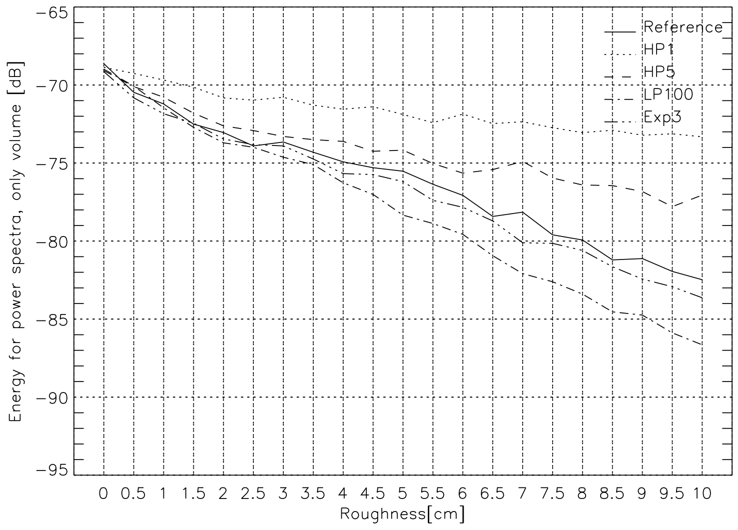

Figure 5.21: *Mean energy of the volume, as a function of RMS roughness, for different parameters (see the legend, and Table 5.1 page 81). The standard deviation varies from about 2-4dB.*

5.5 Sensitivity to geometrical parameters

The geometry of the measurements may significantly influence the results. In this section, the effects of depth, inclination angle (between incoming wave field and the seafloor) as well as the shape and width of the beam pattern will be studied.

5.5.1 Sensitivity to depth

The starting point for this analysis is a sandy seafloor, class C2 (Table 2.2, page 39). In order to simplify the study, the RMS roughness has been set to zero and there is no penetration into the volume. The beam pattern and pulse shape (Ricker@8kHz) are from the TOPAS calibration([7]), but Gaussian beam shapes (see Sec. 5.5.3) have also been used.

Figure 5.22 shows the traces and power spectra as a function of depth, for a flat seafloor. Changes in the echo shape as a function of depth are difficult to detect in the figure. The power spectra shapes get a little less smooth when depth increases, but look otherwise unchanged.

Figures 5.23 and 5.24 show the energy and CofG as function of depth, respectively, using a TOPAS beam pattern. Figures 5.25 and 5.26 show energy and CofG as a function of depth and for several beam widths, using a Gaussian beam.

The figures show that the energy loss for a narrow beam, as a function of depth, is less than spherical energy loss. This is because the footprint increases in size as the depth increases, covering a larger area and more Fresnel zones. When a few Fresnel zones are already covered, including more zones does not however change the energy content significantly (Chap. 2).

For shallow depths, the footprint radius of a narrow beam is smaller than the radius of the first Fresnel zone for a large part of the spectrum, see Table 5.2. This leads to a change in the backscattered signal shape as well as the frequency distribution towards lower frequencies as the depth increases and several Fresnel zones are inside the footprint for the higher frequencies. The more Fresnel zones inside the footprint[4], the less change in the frequency distribution. This is seen in the figures showing CofG as a function of depth (Figs. 5.24 and 5.26), where the CofG is more stable for larger depths.

---

[4] More Fresnel zones inside the beam may be caused by a wider beam or a larger depth.

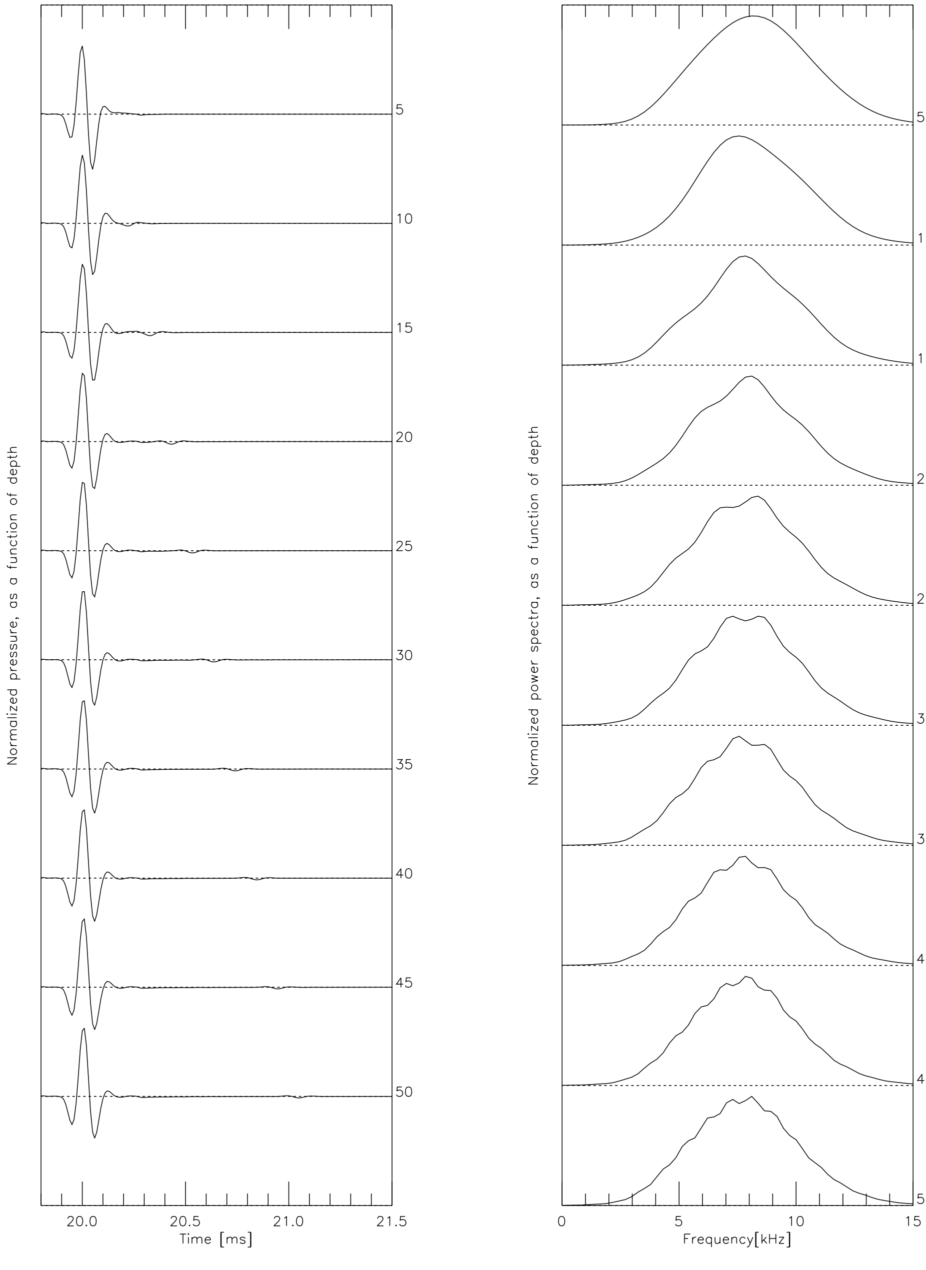

Figure 5.22: *Normalized traces (left) and power spectra (right) from class C2, as a function of depth. The roughness has been set to zero.*

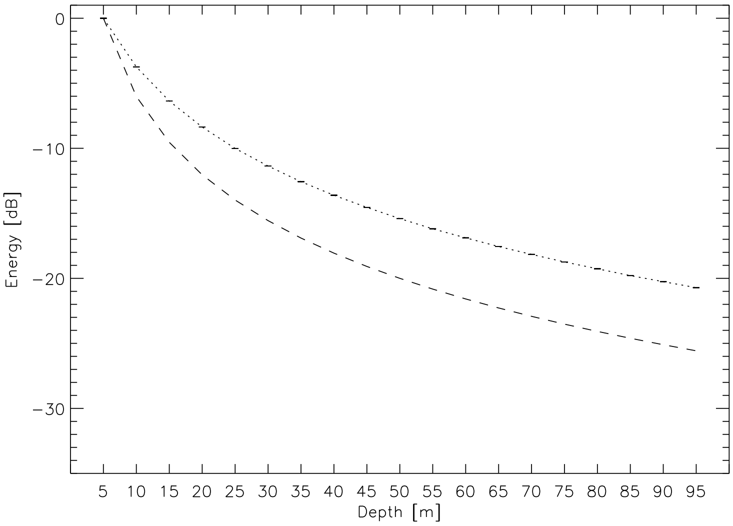

Figure 5.23: *Energy of class C2 (sand), as a function of depth. The roughness has been set to zero. For comparison, spherical energy loss is shown as a dashed line.*

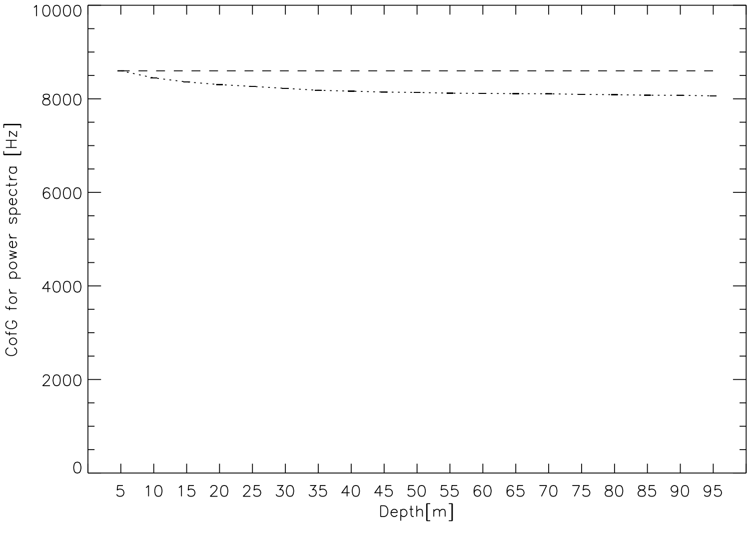

Figure 5.24: *Center of gravity for power spectra, in frequency, as a function of depth. First-order theoretical CofG is shown as a dashed line.*

f	h=15m	h=30m	h=60m
1kHz	3.4	4.7	6.7
5kHz	1.5	2.1	3.0
10kHz	1.1	1.5	2.1
3.5° beam footprint	0.9	1.8	3.7

Table 5.2: *The radius of the first Fresnel zone, in meters, as a function of frequency f and vertical depth h. For comparison, the radius of a 3.5-degree half-width beam (comparable to the TOPAS beam), at different depths, is included.*

This section has shown that the effect of depth, or rather the number of Fresnel zones inside the footprint, on both energy and CofG must be taken into consideration in the estimation technique. This is further described in Chapter 4.

5.5.2 Sensitivity to inclination angle

The starting point is class C2, but with the roughness set to zero and no penetration into the volume. The beam pattern and pulse shape (Ricker@8kHz) are from the TOPAS calibration([7]).

Figure 5.27 shows traces and power spectra for the sensitivity analysis of inclination angle. The tail of the echo shape is seen to become stronger as the inclination angle increases, due to the larger illuminated area of the seafloor which cause increased travel times. The power spectra get less smooth as the inclination angle increases.

Figure 5.28 shows energy as a function of inclination angle. The energy is seen to be reduced significantly with inclination angle. For comparison, the strength of the beam pattern at a direction normal to the surface is included in the figure. This will (except at zero inclination) be a slight underestimation of the total energy of the return, which in the figure is seen to be 0-4dB higher.

Figure 5.29 shows center-of-gravity (CofG) as a function of inclination angle. The CofG has a peculiar appearance. The undulating shape has not yet been well understood. It might be related to the coverage of Fresnel zones.

From this sensitivity study on inclination angle, we suggest that for angles above about 1.5 degrees (assuming the TOPAS applied beam width[5]), both

---

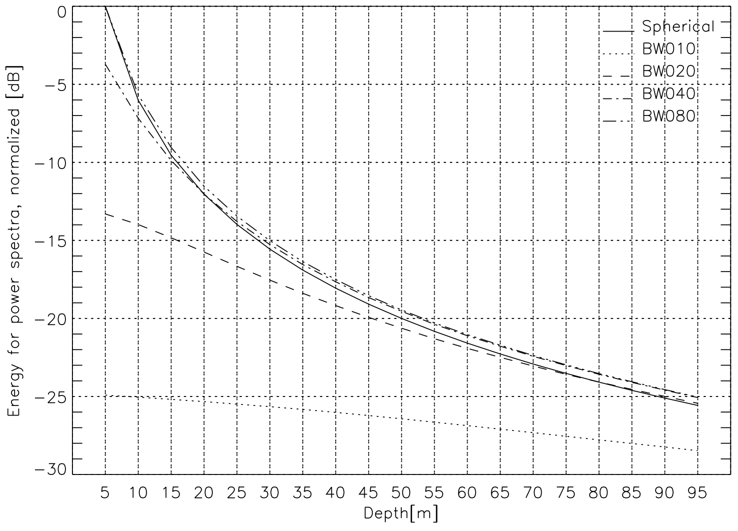

Figure 5.25: *Energy of class C2 (sand), as a function of depth, for different half beam widths (spherical, 1, 2, 4, 8 degrees, see legend). The roughness has been set to zero. The wider beams have close to spherical energy loss.*

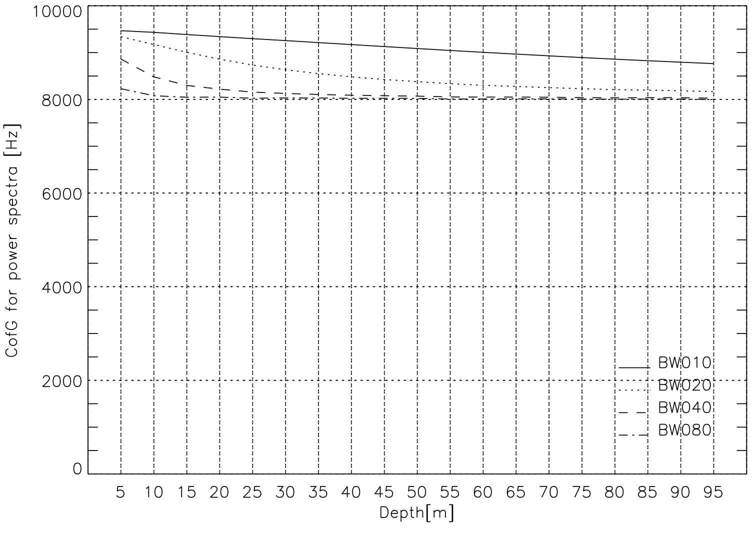

Figure 5.26: *Center of gravity for power spectra, in frequency, as a function of depth, for different half beam widths (1, 2, 4, 8 degrees, see legend).*

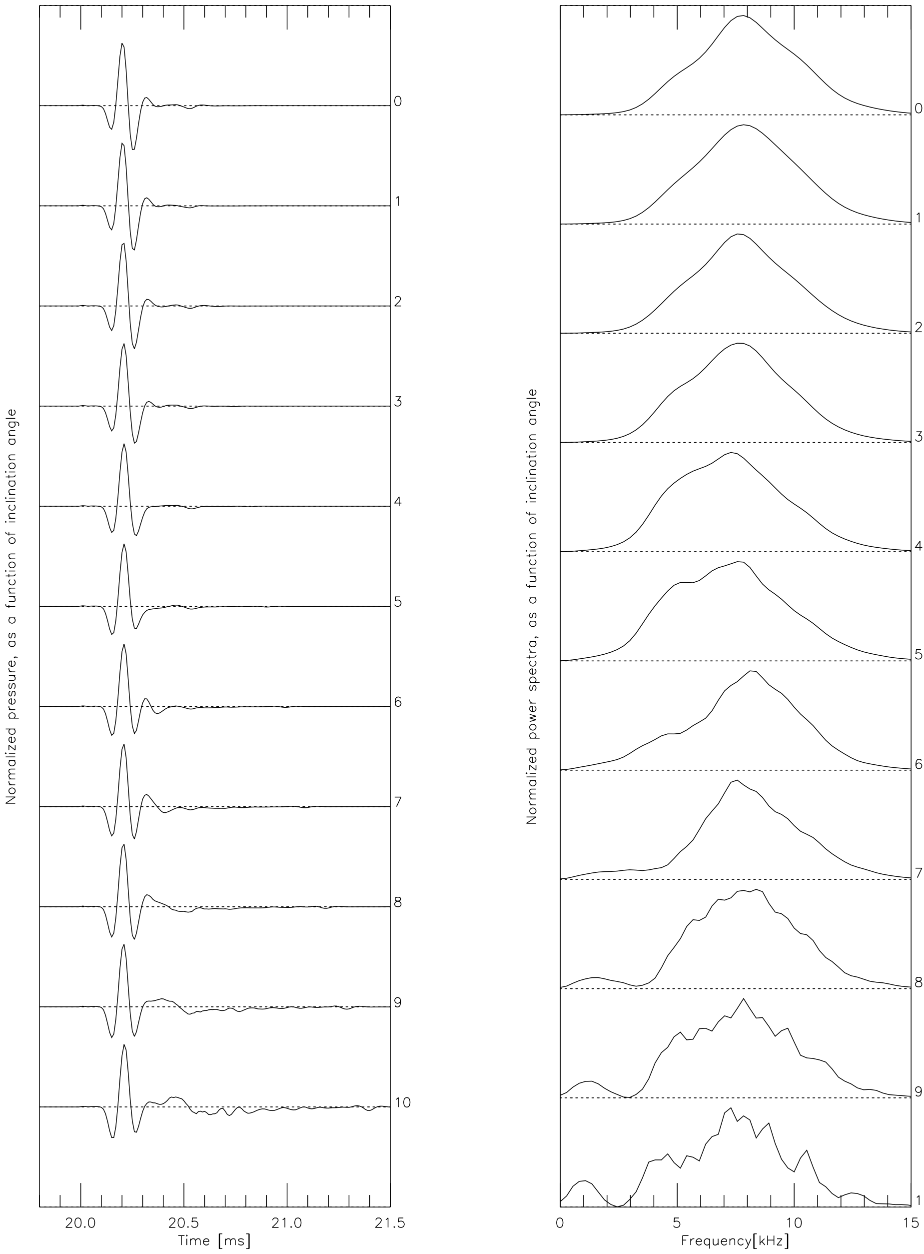

Figure 5.27: *Normalized traces (left) and power spectra (right) from class C2, as a function of inclination angle [degrees]. The roughness has been set to zero. 15m depth.*

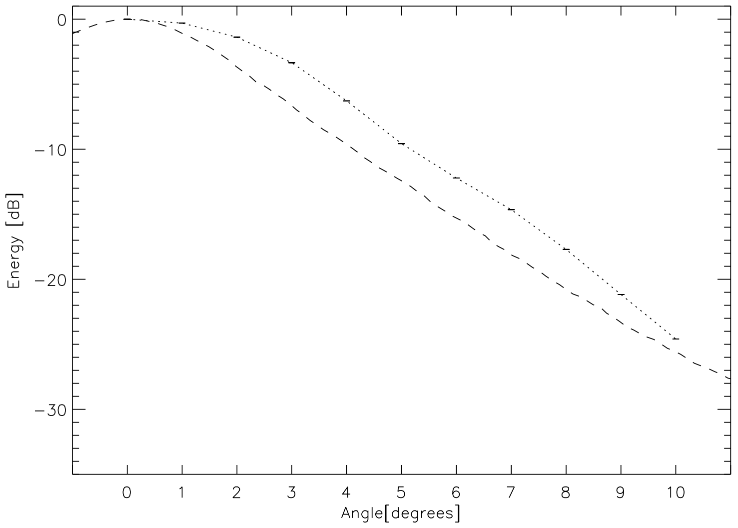

Figure 5.28: *Energy of class C2 (sand), as a function of inclination angle [degrees]. The roughness has been set to zero. 15m depth. First-order theoretical energy is shown as a dashed line.*

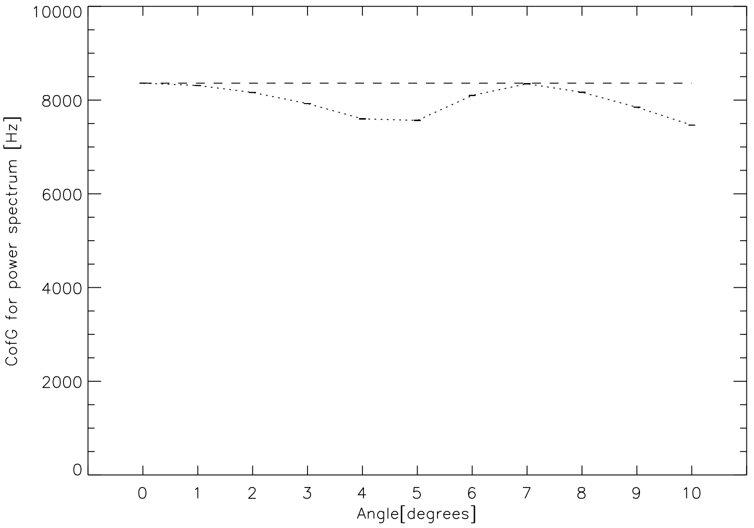

Figure 5.29: *Center of gravity for power spectra, in frequency, as a function of inclination angle [degrees]. The roughness has been set to zero. 15m depth. Theoretical CofG is shown as a dashed line.*

changes in energy and CofG due to the inclination angle should be accounted for in the estimation process.

5.5.3 Sensitivity to beam shape and width

Introduction

This section contains numerical sensitivity analysis of different beam shapes and widths. The parameters for a sandy seafloor – type C2 – has been used, together with a Ricker pulse @8kHz from the TOPAS calibration ([7]). The depth was fixed at 30m. The sensitivity to beam width was analytically treated in Section 3.3.3.

Different beam patterns have been used, the measured one from the TOPAS calibration ([7]) and four synthetic beam patterns with different widths. The synthetic beam patterns are axi-symmetrical and have Gaussian shapes

$$A(\theta) = \exp\left\{-\frac{\theta^2}{2\sigma_\theta^2}\right\} \tag{5.1}$$

where A is the amplitude, θ the angle from vertical and σ_θ^2 the variance of the Gaussian spectrum.

The half beam width has been defined as the point where the amplitude has decreased to $1/e$ (= -8.7dB). Then the half beam width is equal to $\sqrt{2} \cdot \sigma_\theta$. Other definitions might be -3dB (where the energy is halved) and -6dB (where the amplitude is halved). See table 5.3 for the utilized beam widths and a comparison between the definitions of beam widths of a Gaussian spectrum. For other beam pattern shapes, the relations are different.

The TOPAS measured beam pattern is shown together with Gaussian shaped beam patterns in Fig. 5.30. As seen, the shapes are fairly equal but the TOPAS beam does not roll off as quickly as the Gaussian beams. Notice that the TOPAS beam pattern, shown in a 3D representation in Fig. 5.31, is not fully axi-symmetrical such as the Gaussian patterns.

Beam pattern shape

Due to the difference in shape, it is not trivial to find the correct width of a synthetic Gaussian shaped beam pattern to compare with the TOPAS beam

---

[5] 1.5 degrees correspond to slightly less than half the half-beam width of TOPAS. This may be a suitable guideline when using other beam widths as well.

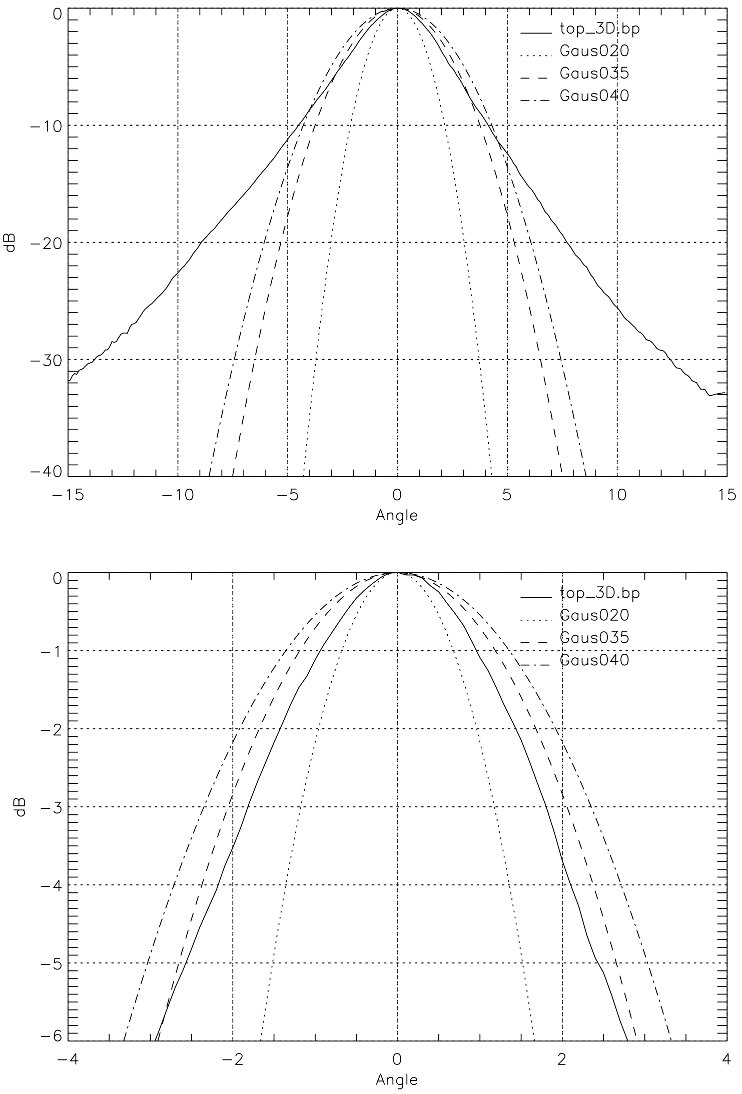

Figure 5.30: *Measured beam pattern of the TOPAS and Gaussian shaped beam patterns (with 2, 3.5 and 4 degrees half width), shown at two different scales.*

$1/e$ (-8.7dB)	-6dB	-3dB
1.00° ⇔ 0.52m	0.83° ⇔ 0.43m	0.59° ⇔ 0.31m
2.00° ⇔ 1.05m	1.66° ⇔ 0.87m	1.18° ⇔ 0.62m
4.00° ⇔ 2.10m	3.33° ⇔ 1.75m	2.36° ⇔ 1.24m
8.00° ⇔ 4.22m	6.66° ⇔ 3.50m	4.71° ⇔ 2.47m

Table 5.3: *Beam widths and radius of the beam at 30m depth, for a Gaussian spectrum. Each line is for one beam width, and shows the half beam width angle and corresponding radius, according to the definitions (1/e, -6dB or -3dB).*

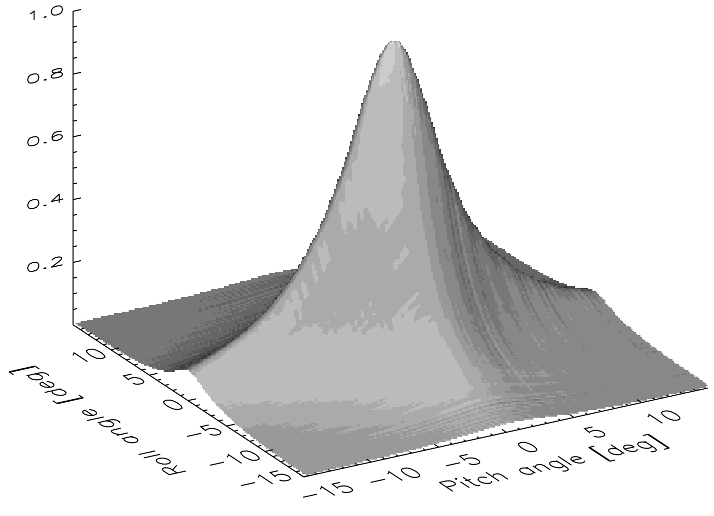

Figure 5.31: *Measured beam pattern strength of the TOPAS beam.*

pattern. However, a half-width around 4 degrees has been chosen to be suitable (Fig. 5.30).

The effect of beam pattern shape, at a fixed depth but with varying RMS roughness, can be studied by comparing Figs. 5.4-5.5 (pages 79, 80), using a TOPAS beam pattern, with Figs. 5.38 and 5.34, using a Gaussian beam pattern with 4 degrees half-width, i.e. with a beam width comparable with the TOPAS. As can be seen, there are no major differences, which could be expected due to the similarity in shape and beam width. The effect of the axial non-symmetry does not seem significant.

Beam pattern width

Figures 5.32-5.35 show the energy as a function of RMS roughness, for the different beam widths. Both single and mean-of-10 traces are shown. Figures 5.36-5.39 show the center frequency shift (using CofG) as a function of RMS roughness, for the different beam widths. Figures 5.42-5.49 compare CofG, energy and the power spectra, respectively, of the different beam widths.

Included in the figures are results from 'BW080win' which is the 8 degrees wide beam but with a tapered window applied to the time series. This was done in order to reduce the effect of overlapping surface and volume contribution, by extracting only the first part of the surface return. In effect this is an 'artificial narrowing' of the beam since only contributions from the seafloor close to normal incidence are included.

Some observations have been done from the figures and are presented below:

The surface:

- CofG: The 8 degrees beam starts to deviate from the theoretical curve relatively early, but for higher roughness the CofG does not increase as much as for the other beam widths. The 2 degrees beam gives the curve closest to theory (for moderate roughness). (Cf. Figs. 5.36-5.39, Fig. 5.42, Fig. 5.44.)
- Energy: The mean-of-10 curve follow the theoretical curve closely for all the beam widths. The single trace follows the theory best for the 2 degree, and then the 4 degree beam, while the 1 degree is the worst. (Cf. Figs. 5.32-5.35, Fig. 5.43, Fig. 5.45.) The wider the beam width, the less the energy decreases when the roughness increases ($\Delta E_{theory,\sigma:0\rightarrow 10cm} =$

$[-42, -39, -33, -27]$dB for half beam widths [1,2,4,8]°, cf. Fig. 5.41). This is due to a higher content of low frequencies in the wider beams (Figs. 5.48-5.49).

- The standard deviation for both energy and CofG increase with increasing roughness, but for an RMS roughness of 4-5cm and above the standard deviation is fairly stable (Figs. 5.32-5.39).
- **Test of windowed 8 degree beam:** Window sizes from 40 to 76 samples wide were tested (a typical Ricker pulse is less than 30 samples long) in order to 'artificially narrow' the beam. The wider windows worked a little better than the narrow ones. All in all, use of a window gave a slight improvement (i.e. the curve followed the theoretical curve better), but the standard deviation increased as well (Figs. 5.40-5.49). The use of a narrower beam still gives markedly better results than the windowed wide beam. The windows used were tapered.

The volume:

- Energy: When stacking traces, the energy decreases proportionally to the number of traces stacked[6]. This confirms that the volume contribution is essentially incoherent. The energy decreases with 13-15dB when the RMS roughness increases from 0 to 10cm. The energy at zero roughness is [-81, -76 -70, -65]dB (for respectively 1, 2, 4 and 8 degrees half beam width), thus higher for larger beam widths (cf. Fig. 5.47). This is due to a larger illuminated area and thus a larger volume covered. The corresponding total energy is [-49, -40, -38, -38]dB. The standard deviation of energy (single traces) is about 2-3dB and fairly similar for all the beam widths and roughness, although a bit larger for 1 and 8 degrees beam width.
- CofG: The shape of the CofG-versus-roughness curve does not change when stacking is done. This is as expected for the incoherent signals from the volume. The standard deviation is about 0.5kHz, fairly independent of beam width and roughness. $f_{CofG}(\sigma = 0) = [10.0, 11.2, 10.4, 9.0]$kHz. $\Delta f_{CofG}(\sigma : 0 \rightarrow 10cm) = [-2.8, -2.2, -2.8, -2.0]$kHz. (Cf. Fig. 5.46.)

---

[6] Thus, by stacking 30 traces, the energy is reduced to 1/30. This has been verified numerically.

Conclusions

From the study of sensitivity to beam width, some conclusions can be drawn:

- Larger beam widths mean that the contributions from surface and volume overlap more (see Fig. 3.2, page 51). A part of the return containing mostly surface contribution can be extracted by using a time window (with suitable tapering). This improves the results, but a narrow beam is still better than a windowed wide one.
- Both CofG and energy (looking at single traces) follow the theoretical curves best for 'medium' beam widths: 2 and 4 degrees half width. This is due to more incoherent energy being returned from a large footprint, since the coherent part comes mostly from vertical return. On the other hand, wide beams are less influenced by the grazing angle (which is determined by sonar/boat tilt and bottom slopes). When looking at the graphs more in detail we see that the 2 degree beam is best at low roughness, but the 4 degree one shows less increase in CofG as the roughness get very high.
- A wide beam will experience less center frequency shift due to depth, because more Fresnel zones are inside the footprint.
- Larger beam widths have less decrease in energy as the roughness increases. This means that the impedance estimate for a wide beam is less influenced by poor RMS height estimates.
- A high volume contribution may increase the CofG and lead to underestimated RMS roughness, due to the CofG and energy for the volume decreasing less than the CofG and energy for the surface, as the roughness increases. This can in principle be corrected for in the calculations.

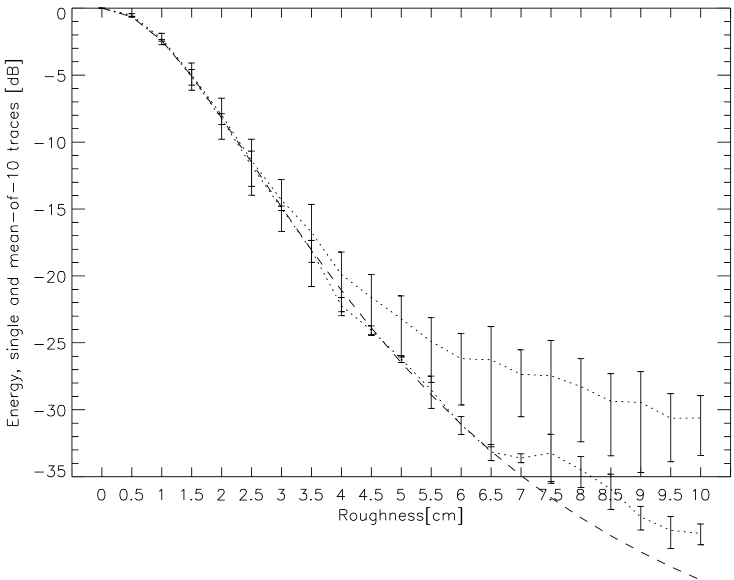

Figure 5.32: *Energy of class C2 (sand), as a function of RMS roughness. Single and mean-of-10 traces are shown, with standard deviations. Theoretical energy is shown as a dashed line. Half beam width 1 degrees.*

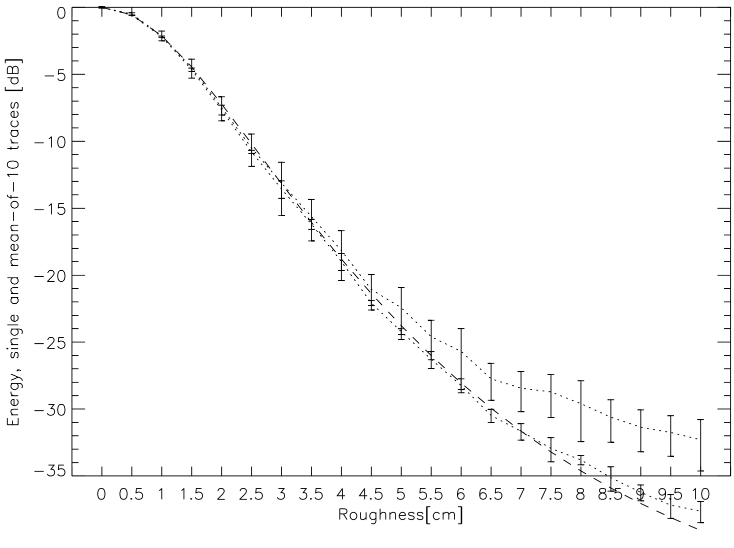

Figure 5.33: *Energy of class C2 (sand), as a function of RMS roughness. Single and mean-of-10 traces are shown, with standard deviations. Theoretical energy is shown as a dashed line. Half beam width 2 degrees.*

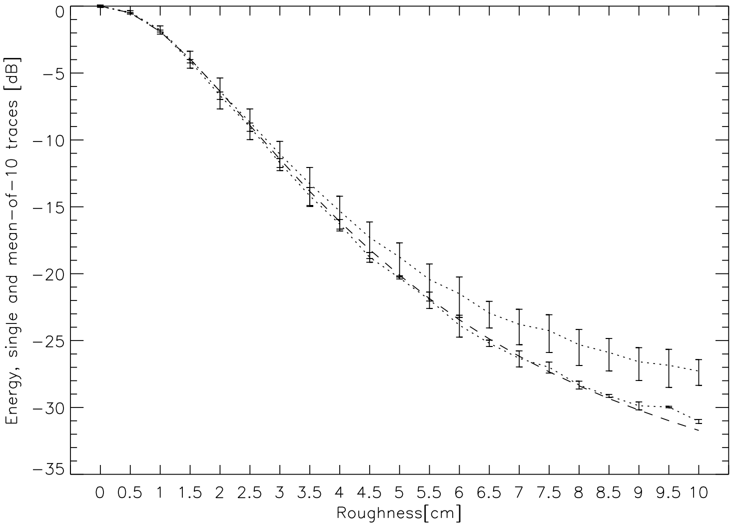

Figure 5.34: *Energy of class C2 (sand), as a function of RMS roughness. Single and mean-of-10 traces are shown, with standard deviations. Theoretical energy is shown as a dashed line. Half beam width 4 degrees.*

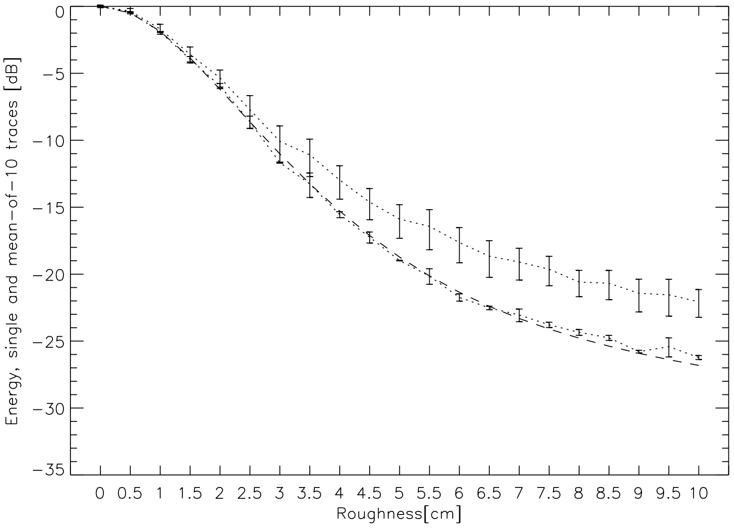

Figure 5.35: *Energy of class C2 (sand), as a function of RMS roughness. Single and mean-of-10 traces are shown, with standard deviations. Theoretical energy is shown as a dashed line. Half beam width 8 degrees.*

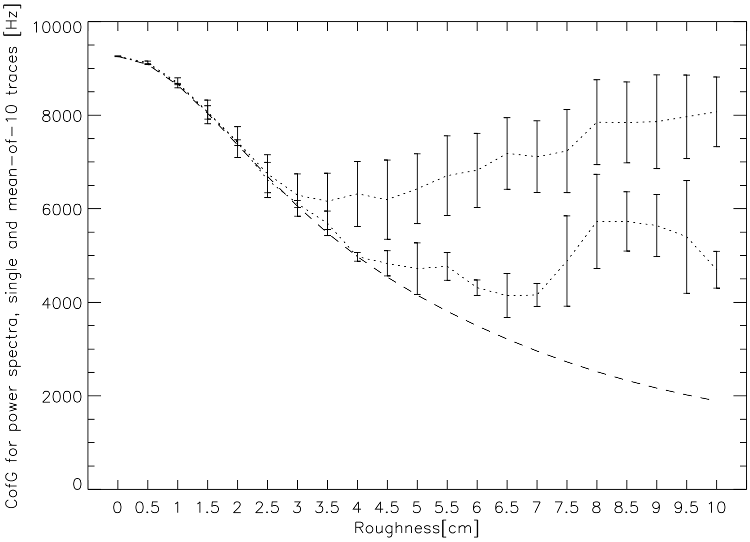

Figure 5.36: *Center of gravity for power spectra, in frequency, as a function of RMS roughness. Single and mean-of-10 traces. Theoretical CofG is shown as a dashed line. Half beam width 1 degrees.*

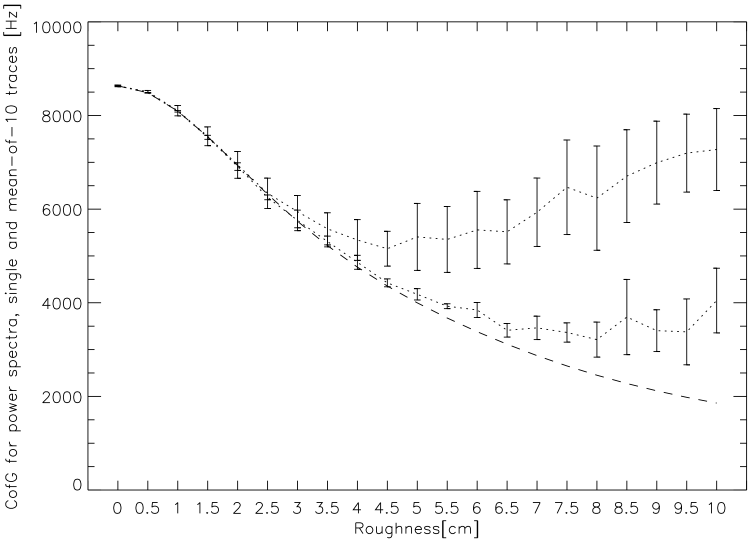

Figure 5.37: *Center of gravity for power spectra, in frequency, as a function of RMS roughness. Single and mean-of-10 traces. Theoretical CofG is shown as a dashed line. Half beam width 2 degrees.*

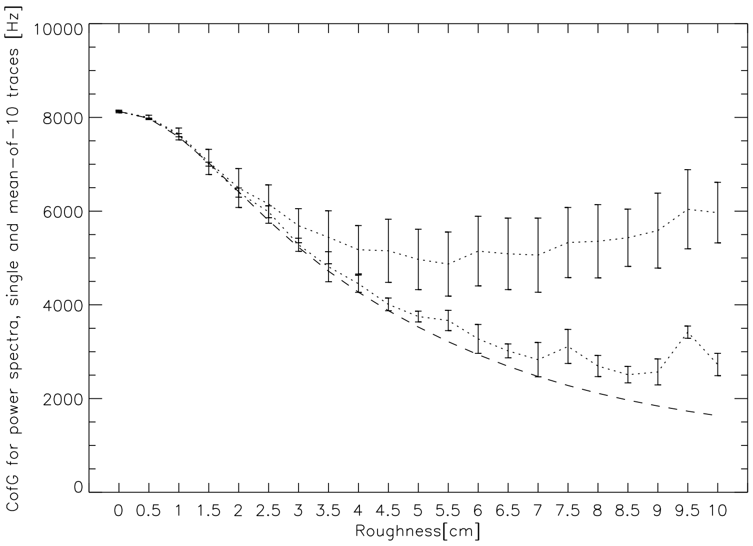

Figure 5.38: *Center of gravity for power spectra, in frequency, as a function of RMS roughness. Single and mean-of-10 traces. Theoretical CofG is shown as a dashed line. Half beam width 4 degrees.*

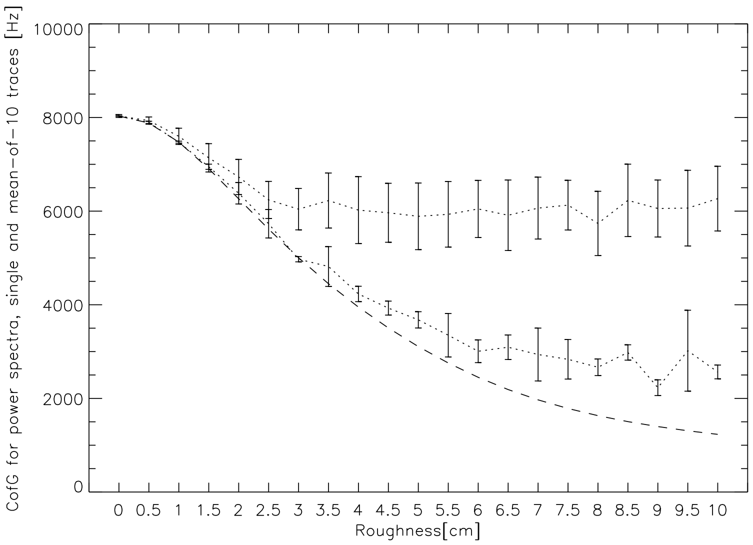

Figure 5.39: *Center of gravity for power spectra, in frequency, as a function of RMS roughness. Single and mean-of-10 traces. Theoretical CofG is shown as a dashed line. Half beam width 8 degrees.*

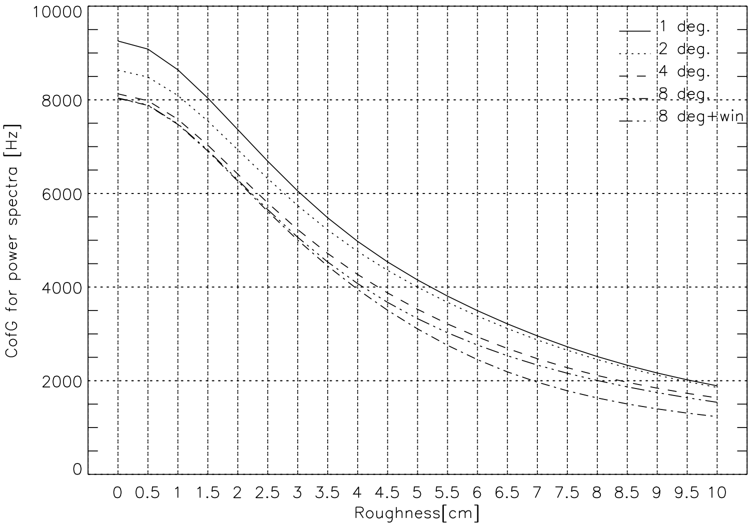

Figure 5.40: *Theoretical center of gravity for power spectra, in frequency, as a function of RMS roughness, for different beam widths.*

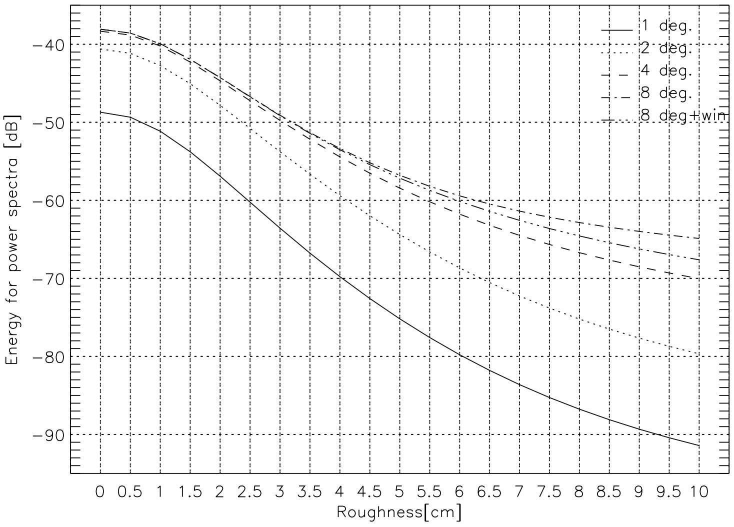

Figure 5.41: *Theoretical energy, as a function of RMS roughness, for different beam widths.*

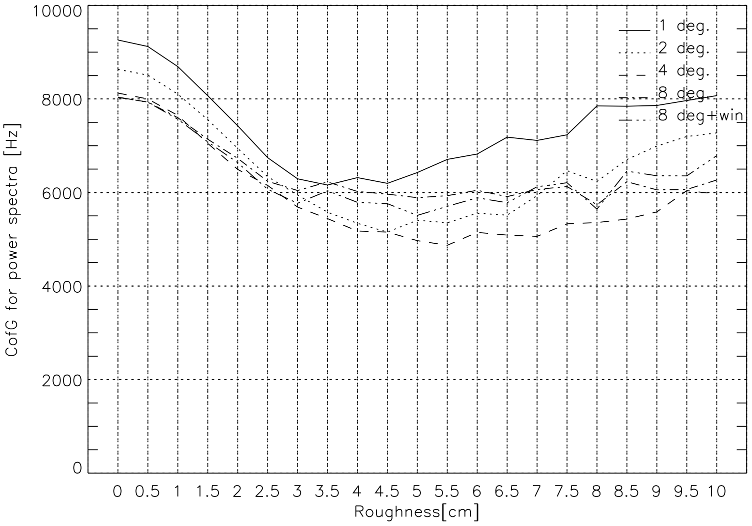

Figure 5.42: *Mean center of gravity for power spectra, in frequency, as a function of RMS roughness, for different beam widths. Single traces.*

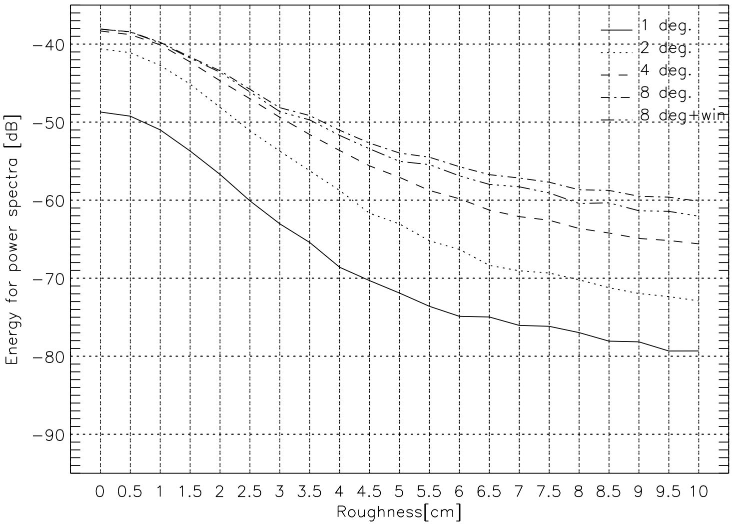

Figure 5.43: *Mean energy, as a function of RMS roughness, for different beam widths. Single traces.*

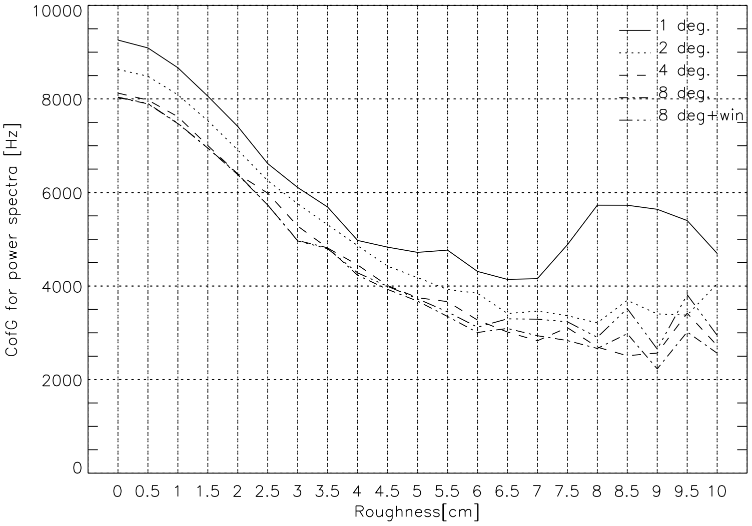

Figure 5.44: *Mean center of gravity for power spectra, in frequency, as a function of RMS roughness, for different beam widths. Mean-of-10 traces.*

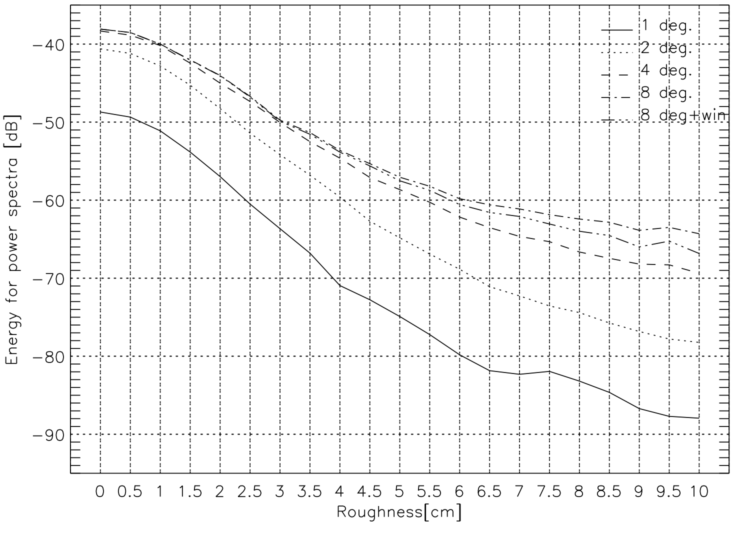

Figure 5.45: *Mean energy, as a function of RMS roughness, for different beam widths. Mean-of-10 traces.*

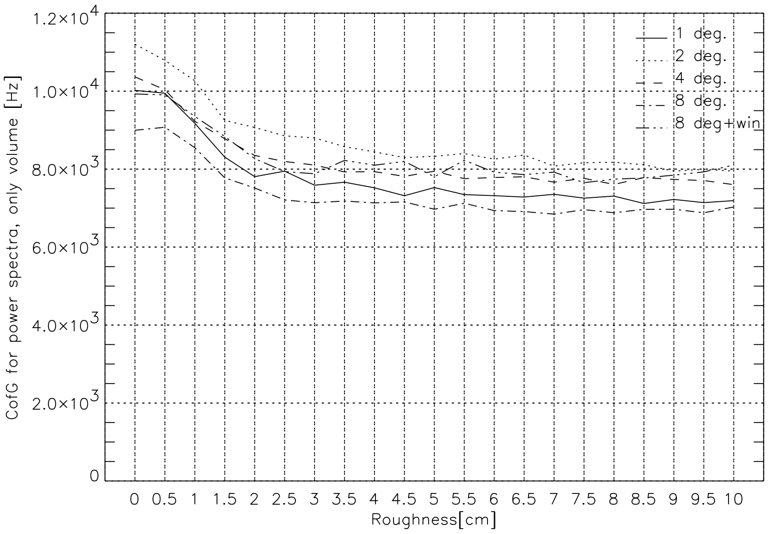

Figure 5.46: *Mean center of gravity for power spectra of the volume, in frequency, as a function of RMS roughness, for different beam widths. The standard deviations are all around 500Hz.*

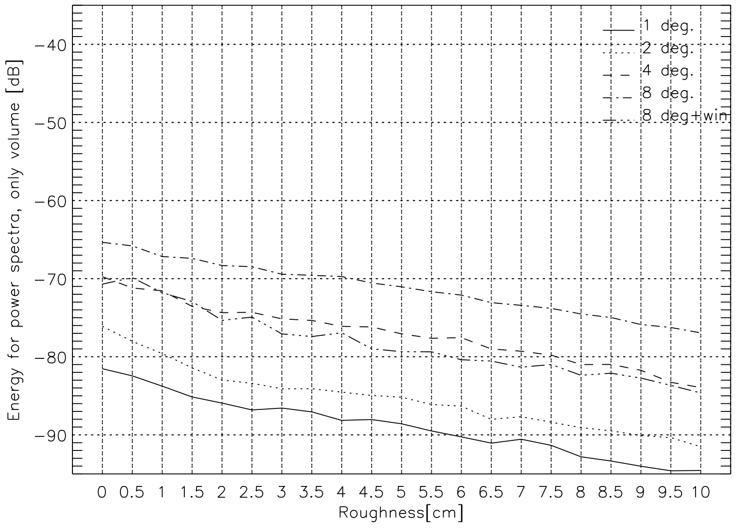

Figure 5.47: *Mean energy of the volume, as a function of RMS roughness, for different beam widths. The standard deviation varies from about 2-4dB.*

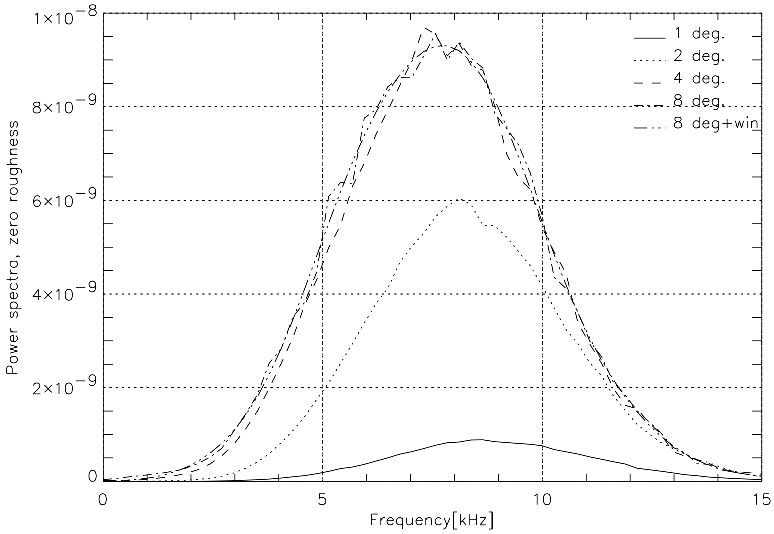

Figure 5.48: *Power spectra, for different beam widths, at zero roughness.*

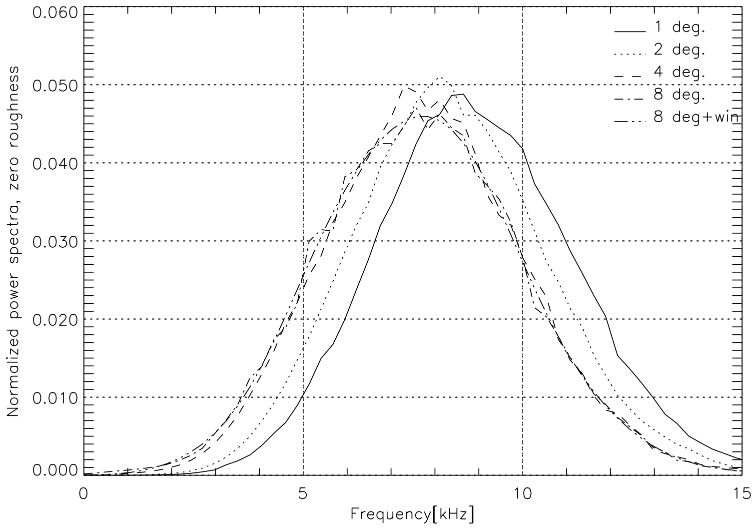

Figure 5.49: *Normalized power spectra, for different beam widths, at zero roughness.*

5.6 Summary and conclusions

This chapter has described a sensitivity analysis of the model parameters determining the acoustic backscattering from a rough seafloor.

The sensitivity analysis has not revealed any major drawbacks or limitations of the estimation method. The following summarizes the findings

- The backscattering is sensitive to the geoacoustical parameters impedance contrast, attenuation and volume inhomogeneity. Seafloor sound speed and density can not be separated and only appear together as impedance.
- The RMS height of the surface influences the energy and CofG of the return significantly, and estimates of RMS height can be found from the CofG. Too large roughness values might be underestimated, however this is indicated by error measures (standard deviations of measurements).
- The effect of volume inhomogeneities is to directly determine the backscattered level from the volume.
- The effect of volume attenuation is to decrease backscattering strength and to lower the high-frequency content in the backscattering from the deeper parts of the volume. Estimation of attenuation has not been studied numerically, nor yet been implemented in FARIM.
- Stacking significantly improves the estimation of both RMS roughness and impedance. This is because stacking retain the coherent part of the backscattering and reduce the incoherent part. The estimation relies on the coherent part.
- Of the surface height spectrum parameters, only the high pass filter wave number has any significant effect on the energy and center frequency shift. This should be further studied.
- The sensitivity to depth is significant, but is easily corrected for. This is automatically done by FARIM.
- The sensitivity to seafloor inclination angle is significant for angles above $\sim 1.5°$ (when using a typical TOPAS beam), but may be corrected for. This is sometimes done in analysis with FARIM.
- The sensitivity to beam width is significant, and must be accounted for. The exact shape of the pattern was not found to be overly important. A medium wide beam (2-4° half-width) gave the best results.

- Low impedance contrast coupled with a high volume inhomogeneities factor might lead to underestimated RMS roughness. This can in principle be corrected for by using both the surface and volume contribution from the synthetic reference data when computing the reference CofG. This should be coupled to an estimation of the volume inhomogeneities factor.

The sensitivity analysis has shown that good estimates of both RMS roughness and impedance can be expected, when a good source calibration (of pulse shape, with absolute values, and beam width (and shape)) is done. Stacking improves the results significantly, and poor estimates are indicated by error estimates. However, the importance of the high pass filter wave number (of the surface height spectrum parameters) should be further studied, in connection with analysis of real seafloors.

Chapter 6

Analysis of field data

Synthetic data has been used to directly verify the estimation technique, with good results (Sec. 4.4). It suggests that roughness and impedance can be accurately determined when the roughness is moderate, and that uncertain estimates can be identified by error measures.

The estimation technique has also been applied to field data, from different areas in the Mediterranean, North Sea and Baltic. The results look promising, show good consistency and correlate well with ground truth and alternative characterization methods.

6.1 Results from applying FARIM to field data

The parametric bottom penetrating sonar Simrad Topas PS040 was used for all the field data acquisition. This sonar provides broadband pulses of different kinds (e.g. Ricker, FM-sweep, Burst). The data from the Mediterranean was collected with a towed buoy where the parametric sonar was mounted. The data from the North Sea and the Baltic were both collected with a hull-mounted system on the vessel M/S Simrad. Various multi-beam echosounders, side-scan sonars and ground-truth data acquisition systems were also used during the surveys.

Some of the work presented in this chapter has previously been published, see [18], [17], [15], [14], [13], [12].

6.1.1 Field data from the Mediterranean

The data from the Mediterranean was collected during the SACLANTCEN cruise 'Mosaic', April 1997, at different shallow water sites outside the West coast of Italy. The sites that have been analyzed are Tellaro, Ombrone, Golfo Stella, Viareggio and Scoglio Africa. Only the pings that had less than 2 degrees tilt from vertical (due to measurement buoy movements) were analyzed. The source pulse was a Ricker, with a center frequency of 8kHz and a band width of about 100%. A stacking of 5 traces were used in the processing.

Ground truth from the areas exists in the form of gravity cores, grab samples, photographs, video footing and divers impressions. Values for compressional sound speed and density have been calculated from the gravity cores. From these, impedance values are calculated. There is no direct measurement of roughness available. A stereo camera for measuring roughness was deployed during the cruise, but broke down and could not be used. Within ISACS, another characterization method has been developed. It is an inversion method called sirOb. The method is described at the end of this section, and comparisons between sirOb and FARIM are presented.

Figures 6.1-6.10 show the roughness and impedance estimates from the processed areas of the Mediterranean. The estimated impedance from the energy of the return alone, i.e. not corrected for roughness, is also shown. At the sites with gravity cores, i.e. Ombrone, Golfo Stella and Viareggio, the impedance value measured from the core is marked in the impedance plots.

The processing of the Mediterranean data has not involved corrections for the real incidence angle with the seafloor. Due to the fairly flat seafloor at most of the sites this was not necessary, although at Golfo Stella it might have slightly improved the estimates.

The impedance from the gravity core at Golfo Stella has been compared with FARIM estimated impedance (at nearby positions) to determine the correct source level.

The estimated impedance values correspond well with the available gravity core values (table 6.1) and thereby improve our confidence in the method. The three estimated values are all within 3% from the core measurements, i.e. less than the combined uncertainty of the core measurements and slightly different positions of the core and acoustic track. The corresponding roughness at the core positions were different, indicating that the roughness correction of the impedance of the FARIM method works well.

	Golfo Stella	Ombrone	Viareggio
Core measurement	*2.52*	*2.79*	*2.99*
FARIM estimates	2.58	2.85	2.90
sirOb estimates	2.55	2.85	3.67

Table 6.1: *Comparison between impedance values from the gravity core measurements and the estimates by FARIM and sirOb. The unit is* $\cdot 10^6 kg/(m^2 s)$.

The different sites from the Mediterranean are described and analyzed below, both for impedance and roughness. A description of the characterization method sirOB and comparisons of results from this method and FARIM then follows.

Tellaro

This area consists of mainly sand, at a water depth of 14m. Figures 6.1-6.2 show estimated roughness and impedance from the area. The impedance values seem reasonable for sand. There are however a few local spots, e.g. at a sailed distance of 70m, 130m and 540m, that are quite high. These might just be local variations, but no further information is available to confirm this. The impedance values that are not corrected for roughness are fairly correlated with the corrected impedance. The values are however unreasonably low, considering the nature of the site. This shows the importance of correcting the impedance estimates for roughness.

The roughness values seem reasonable, except from one outlier ping at 150m sailed distance. The variation of the roughness along the track occurs over several pings indicating that the variation is indeed a variation in the seafloor and not just a random variation.

There are some correlation between the roughness and impedance in the area. This has also been seen in the analysis of other areas (Sections 6.1.2 and 6.1.3). This supports the idea that a harder seafloor (thus having a higher impedance) can sustain a higher roughness.

Ombrone

The track "Ombrone" is close to the estuarine of the Ombrone river, on the southern coast of Tuscany. Water depth is 23-26m along the surveyed track, which is about 700m long and almost parallel to the coast. It comes closer to the river estuarine toward the end of the track. Figures 6.3-6.4 show estimated roughness and impedance from the area.

The core taken at the Ombrone site is about 1m long, and its location is slightly (about 90m) off track. Sound speed and (wet) density have been measured along the core at intervals of 0.02m and 0.06m respectively. The mean acoustic impedance obtained from the core measurement is $2.79 \cdot 10^6 kg/(m^2 s)$. The estimated impedance by FARIM in the proximity of the gravity core is $2.85 \cdot 10^6 kg/(m^2 s)$, which matches well with the ground truth results.

The seafloor is soft up to about 150m, then there is a sandy region which from 400m has some softer material in between. This corresponds well with the estimated impedance. The estimated roughness values seems very reasonable for the given seafloor. The variations in both impedance and roughness take place over several pings, so they are clearly related to properties of the seafloor and are not just random variations. The rather high impedance values estimated near the start and end of the track are somewhat strange, but appears over several pings with a gradual increase and are therefore likely to be related to physical properties of the seafloor.

Golfo Stella

Golfo Stella is on the southern side of the island Elba. The track was from offshore towards the coastline, with the depth varying from 41m at the start of the track to 25m at the end of the track. The bottom is silty, and from about 600m sailed distance the track is covered with Posedonia (a sea weed). Figures 6.5-6.6 show estimated roughness and impedance from the area.

A sea floor covered with vegetation does not necessarily fulfill the Kirchhoff approximation, due to the non-smooth appearance, so the estimated parameters should not be expected to fully correspond to the physical parameters. The results are still very interesting. The roughness increases considerably at 600m, clearly indicating where the bottom is covered with vegetation. There are some fluctuations in both the impedance and roughness in the Posedonia covered area, which are to be expected, since the amount of vegetation (and e.g. the degree of bubbles on the sea weed) varies along the track. This can easily be seen on video recordings of the bottom.

The available gravity core is in the no-vegetation area, and a mean acoustic impedance of $2.52 \cdot 10^6 kg/(m^2 s)$ was measured. This value was used to calibrate the source level of the system.

From the analysis of this area it seems that the FARIM method gives reasonable and predictable results even when the Kirchhoff approximation does not hold.

Viareggio

The track length on Viareggio (on the northern coast of Tuscany) was 1400m. The water depth along the track was around 24m, and a sandy seafloor with possible trapped gas spots was expected (based on previous information about the area). A subsurface layer was found at 0.3m depth. This can at certain spots lead to an overestimation of the impedance, because this layer interferes with the seafloor surface reflection. This might have happened e.g. at the very last part of the track as well as at 900m and 1100m sailed distance.

Figures 6.7-6.8 show estimated roughness and impedance from the area. The estimated impedance seems reasonable for a sandy seafloor, and the available gravity core impedance ($2.99 \cdot 10^6 kg/(m^2 s)$) is in good agreement with the estimated impedance ($2.9 \cdot 10^6 kg/(m^2 s$ for the mean of the 3 last points on the track). However it should be noted that the core was taken about 50m after the end of the track. The estimated roughness is varying and is in general higher than on the other sites (except where Posedonia exists), so the seafloor is apparently rough and inhomogeneous. This seems reasonable for a seafloor with trapped gas spots.

Scoglio Africa

Plots from the Scoglio Africa are shown in Figs. 6.9-6.10. The region consists of Posedonia over rocks[1], and are clearly outside the scope of the Kirchhoff approximation. It was chosen in order to test the estimation algorithm outside its range of validity. The weather during the survey was not good, so many pings had to be discarded due to excessive angles.

The estimates indicate a roughness between 2-6cm, mostly hovering around 4cm. The estimated impedance is mostly from 1.8 to $3.5 \cdot 10^6 kg/(m^2 s)$. The analysis of this area shows that it is possible to distinguish between situations where the FARIM method works well and where the results should be carefully evaluated. In this area, the estimated roughness is high as it should be, but the actual numerical value might not be correct. This may also lead to an

---

[1] This information stems from previous research and video footing

underestimated impedance. This seems to have happened in this analysis, since such a rocky seafloor would be expected to have a somewhat higher impedance than the one estimated.

The analysis of this area shows that the FARIM method is not always directly applicable, but also that these situations are fairly easy to identify.

Comparison with the inversion method sirOb

The software package sirOb – Seafloor Identification by Remote Sensing Of the Bottom – has been developed by A. Caiti *et. al.* within the ISACS project for inversion of parametric sonar data (time series) at normal incidence [20], [22], [23].

sirOb has been developed with BORIS (Sec. 2.5) as forward model but this is no limitation to sirOb, in practice any other time series model can be used as forward model. To compare the acquired and computed time series, sirOb uses cost functions derived from a wavelet processing. The Ricker wavelet is used as mother wavelet, a wavelet that is equal to the one used by the parametric source. The cost functions are minimized to obtain a best possible estimate of the geoacoustic parameters [21]. The sirOb inversion method has relatively long processing times and can not currently be used in real time analysis.

The current version of sirOb provides estimates of geoacoustic and morphological parameters in the upper stratum (first layer): Acoustic impedance, seafloor roughness, P-wave attenuation and volume inhomogeneities

The results from sirOb (for the areas that have been analyzed by both methods) are plotted in the same figures as the FARIM results so that the estimates can be compared. sirOb analysis have only been available from areas in the Mediterranean, and not from all the sites analyzed by FARIM. The sirOb analysis was done by A. Caiti *et. al.* ([20], [23]). A comparison between the results from FARIM and sirOb for the different sites is presented below.

Ombrone:
The estimated impedance by both FARIM and sirOb ($2.85 \cdot 10^6 kg/(m^2 s)$ for both methods) are very close to the ground truth results ($2.79 \cdot 10^6 kg/(m^2 s)$). The roughness estimates are quite similar between the methods, but FARIM estimates a slightly higher roughness. This might be explained by the stacking performed in this FARIM analysis. According to Kirchhoff theory, stacking improves the coherent part of the signal and thus gives less under-estimation for high roughness values. The sirOb results also show somewhat less consistency; the estimates change more abruptly along the track.

Golfo Stella:
Again, both the FARIM and sirOb impedance estimates (2.58 and $2.55 \cdot 10^6 kg/(m^2 s)$, respectively) are in very good agreement with the ground truth ($2.52 \cdot 10^6 kg/(m^2 s)$). The methods however show a different behavior after about 600m sailed distance. In this area the seafloor is covered by posedonia. Here, sirOb estimates a lower impedance, while FARIM estimates are higher than earlier in the track. This might again be explained by stacking; the roughness is very high after 600m and FARIM does indeed show a higher roughness than sirOb. An under-estimated roughness would, according to the theory FARIM is based on, accordingly give under-estimated impedance. Interestingly, FARIM and sirOb give estimates that overall behave very similarily, and in several positions very specific local variations can be observed on the estimates (from both methods), both for impedance and roughness.

The posedonia situation is outside the range of validity of the Kirchhoff approximation, which is used both in FARIM and in BoRIS (the forward model used in the inversion method sirOb), hence the numerical values obtained might have limited physical significance. However, these results may be taken as indications of how the algorithms behave in anomalous situations. It seems that both methods behave reasonably and predictably in such situations, which is good.

Viareggio:
The acoustic impedance measured from the core was $2.99 \cdot 10^6 kg/(m^2 s)$. The core was taken about 50m after the end of the track. The last point on the track in the sirOb estimate gives an acoustic impedance value of $3.67 \cdot 10^6 kg/(m^2 s)$, while FARIM estimates $2.9 \cdot 10^6 kg/(m^2 s)$ for the mean of the 3 last points on the track. sirOb shows larger variations in the roughness than FARIM, which are not easily explained nor verified, since roughness ground truthing is not available.

Scoglio Africa:
Both FARIM and sirOb were tested on the Scoglio Africa data. However, only 49 pings have been presented from the sirOb analysis ([20]), while 177 pings are presented from the FARIM analysis (section 6.1.1). A comparison between the methods has therefore not been done for this area.

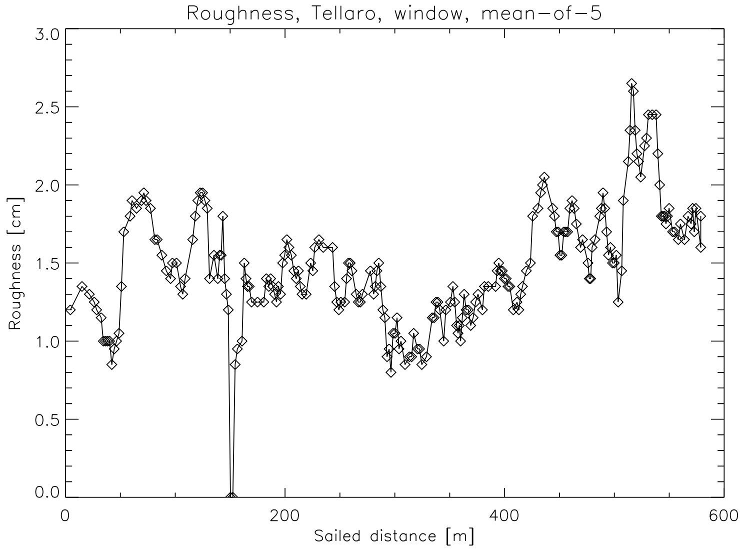

Figure 6.1: *Roughness estimates by FARIM, from the Tellaro site.*

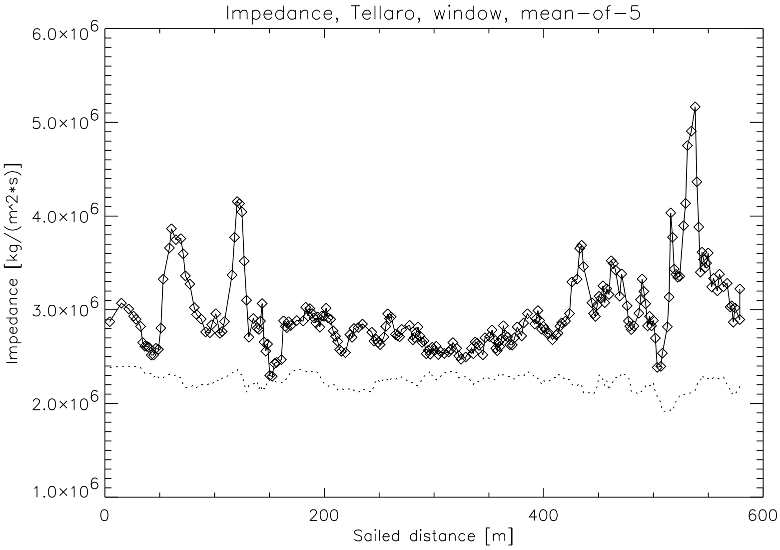

Figure 6.2: *Impedance estimates by FARIM, from the Tellaro site. The estimated impedance without correcting for roughness is shown in the lower dotted line.*

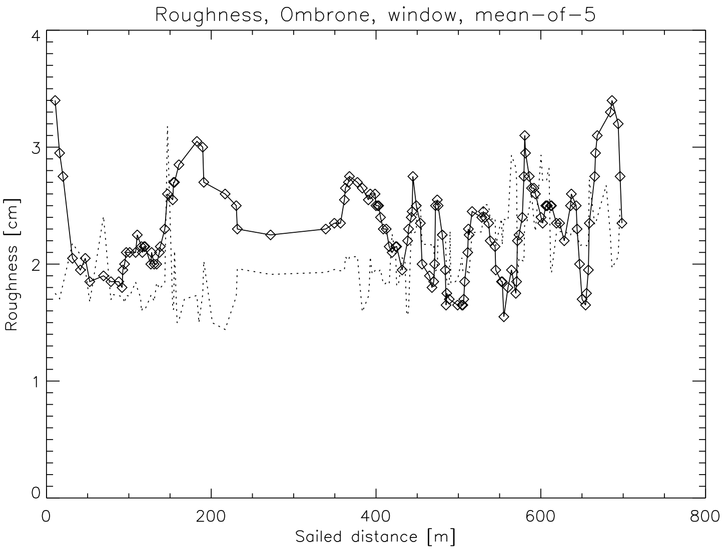

Figure 6.3: *Roughness estimates by FARIM, from the Ombrone site. The sirOb estimates are shown as a dotted line.*

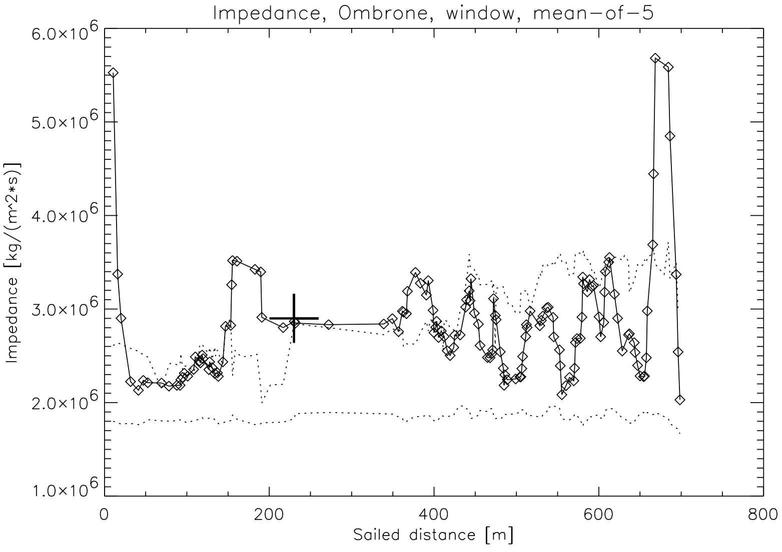

Figure 6.4: *Impedance estimates by FARIM, from the Ombrone site. The impedance value from the gravity core is marked with a + sign. The sirOb estimates are shown as a dotted line. The estimated impedance without correcting for roughness is shown in the lower dotted line.*

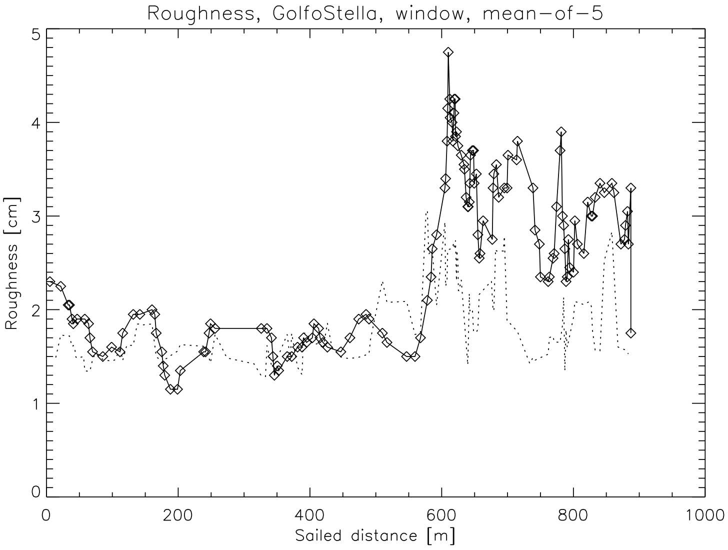

Figure 6.5: *Roughness estimates by FARIM, from the Golfo Stella site. The sirOb estimates are shown as a dotted line.*

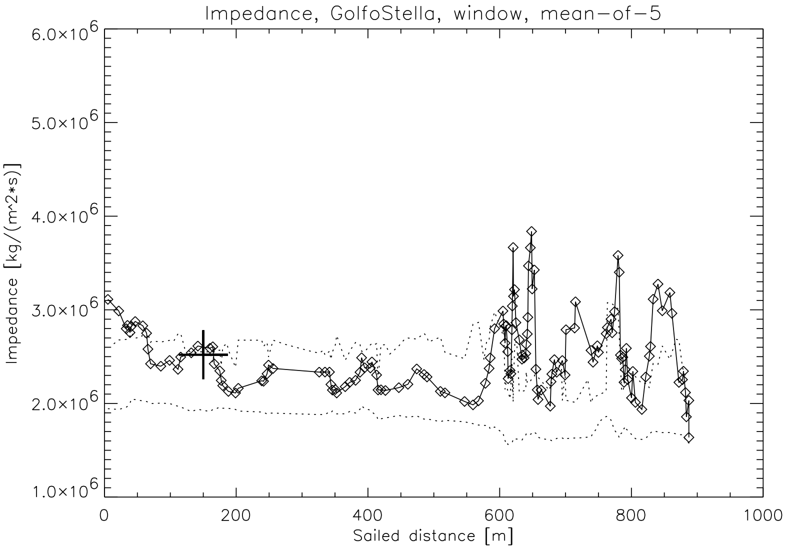

Figure 6.6: *Impedance estimates by FARIM, from the Golfo Stella site. The impedance value from the gravity core is marked with a + sign. The sirOb estimates are shown as a dotted line. The estimated impedance without correcting for roughness is shown in the lower dotted line.*

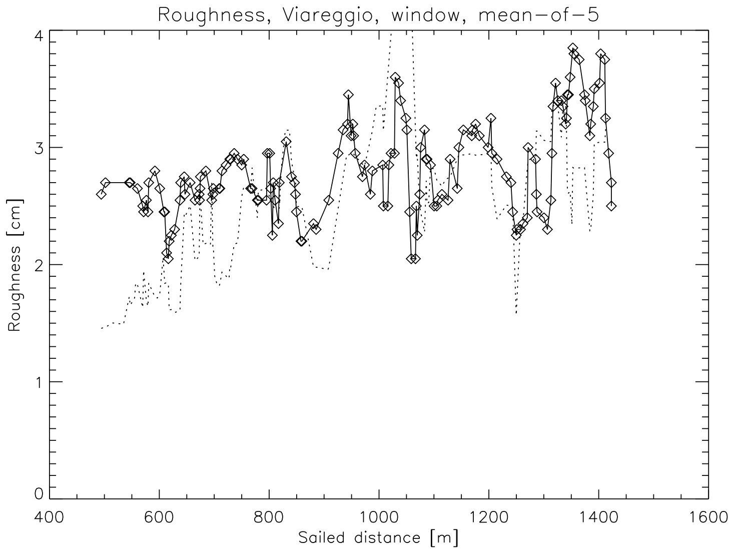

Figure 6.7: *Roughness estimates by FARIM, from the Viareggio site. The sirOb estimates are shown as a dotted line.*

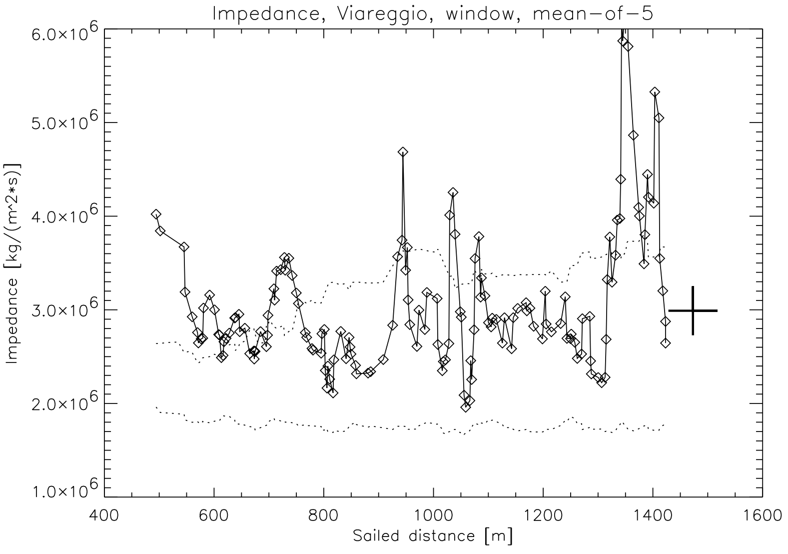

Figure 6.8: *Impedance estimates by FARIM, from the Viareggio site. The impedance value from the gravity core is marked with a + sign. The sirOb estimates are shown as a dotted line. The estimated impedance without correcting for roughness is shown in the lower dotted line.*

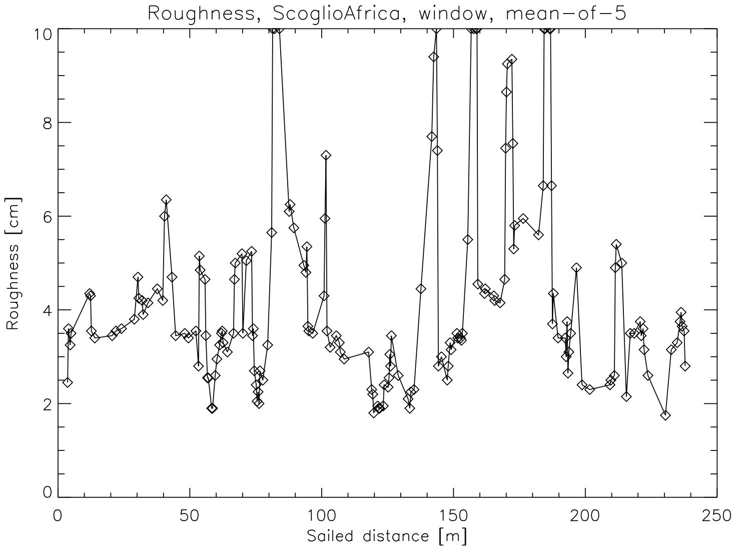

Figure 6.9: *Roughness estimates by FARIM, from the Scoglio Africa site.*

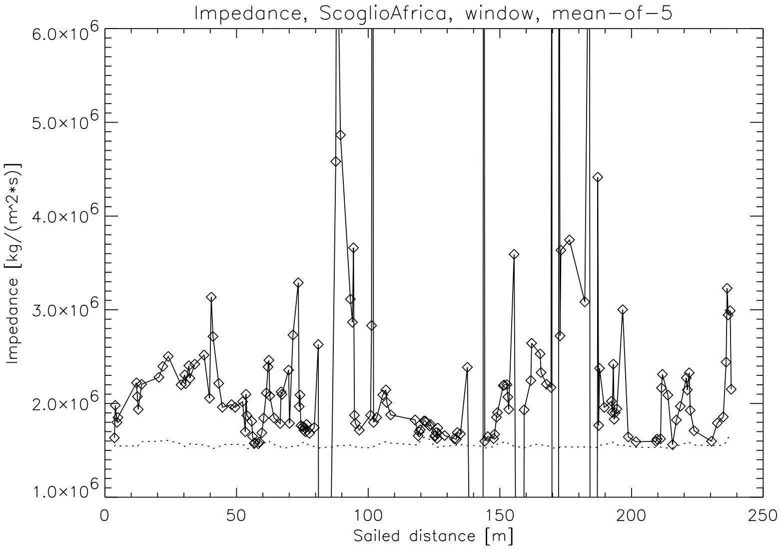

Figure 6.10: *Impedance estimates by FARIM, from the Scoglio Africa site. The estimated impedance without correcting for roughness is shown in the lower dotted line.*

6.1.2 Field data from the North Sea

The analyzed data from the North Sea was acquired during the main sea trials of ISACS, at three sites near Horten, Norway. Only one area, Steinbåen, has been analyzed by FARIM, mainly due to lack of calibration data of the pulse utilized at the other sites.

Figure 6.11 shows the bathymetry along the survey lines of Steinbåen. The positions of the gravity cores are also included. The area is 12-19m deep and consists of clay and sand. The seafloor slope is relatively even, but with a slightly higher slope in the southern part of the area.

Figures 6.12-6.13 show the estimated roughness and impedance for Steinbåen, in a color plot covering the area. The impedance not corrected for roughness is shown in Fig. 6.14.

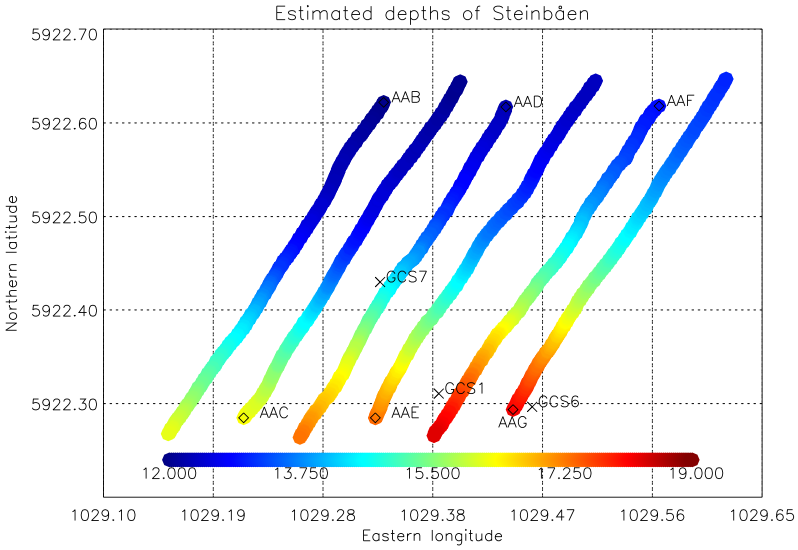

Figure 6.11: *The estimated depths along the survey lines of Steinbåen, with name tags. A small square denotes the start of each line. The positions of the gravity cores are denoted by a cross (GCS7, CCS1, CCS6). The distance between the lines is about 75m.*

Figures 6.15-6.26 show the estimated roughness and impedance along each survey line at the Steinbåen site.

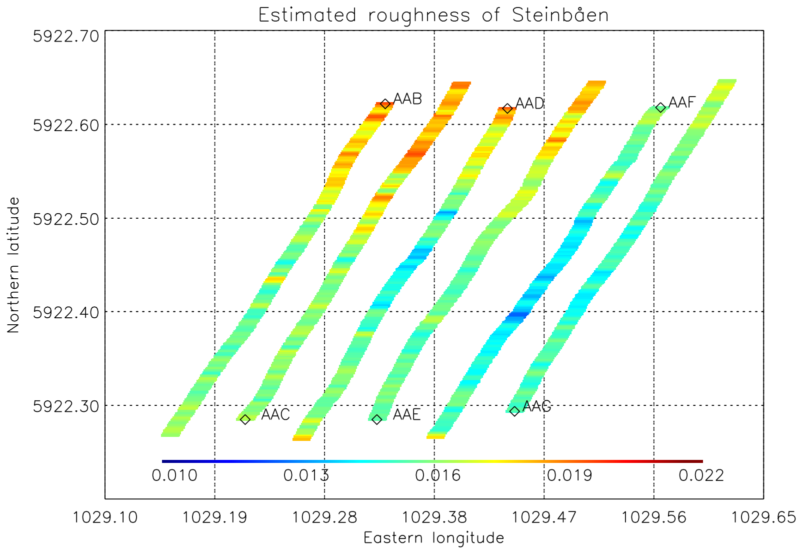

Figure 6.12: *The estimated roughness along the survey lines of Steinbåen, with name tags. A small square denotes the start of each line.*

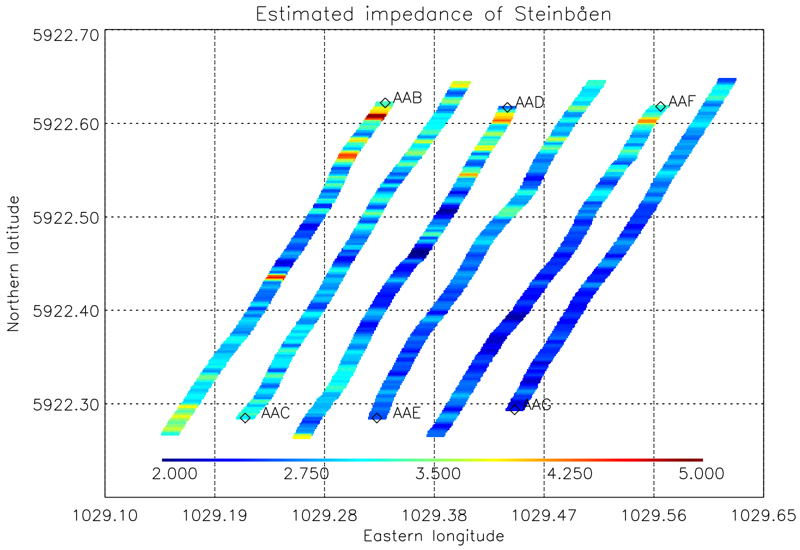

Figure 6.13: *The estimated impedance along the survey lines of Steinbåen, with name tags. A small square denotes the start of each line.*

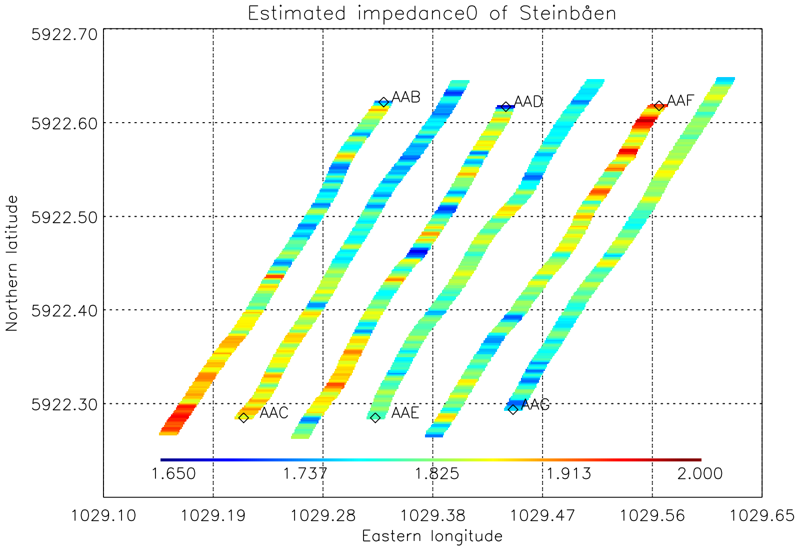

Figure 6.14: *The estimated impedance, without correcting for roughness, along the survey lines of Steinbåen, with name tags. A small square denotes the start of each line. Notice that the color scale is different from the one in Fig. 6.13.*

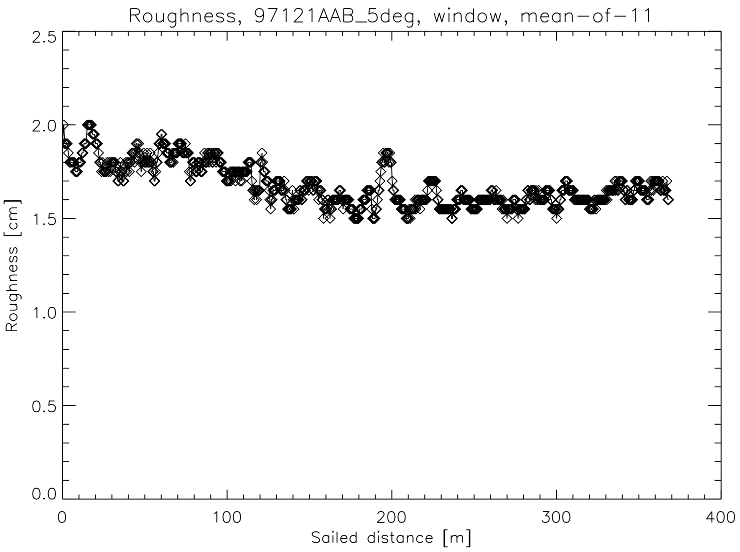

Figure 6.15: *Roughness estimates by FARIM, from Steinbåen.*

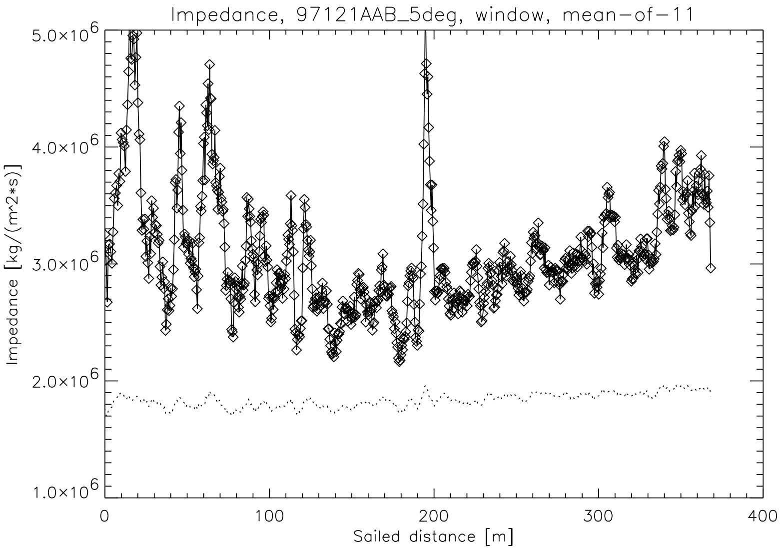

Figure 6.16: *Impedance estimates by FARIM, from Steinbåen. The estimated impedance without correcting for roughness is shown in the lower dotted line.*

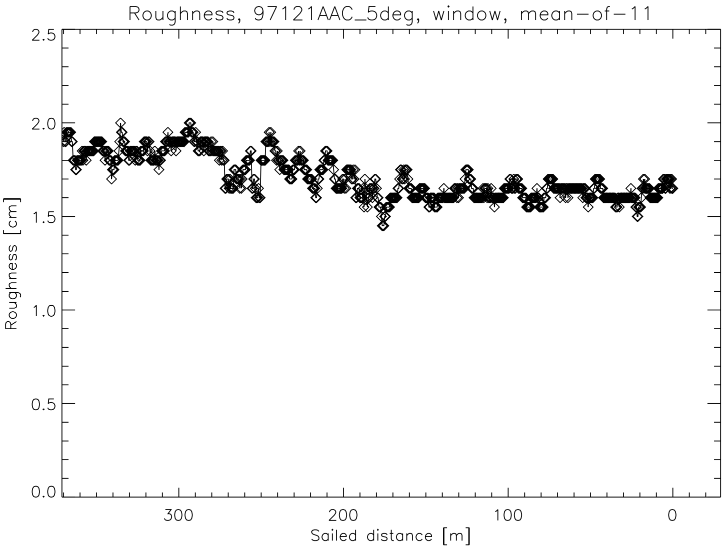

Figure 6.17: *Roughness estimates by FARIM, from Steinbåen.*

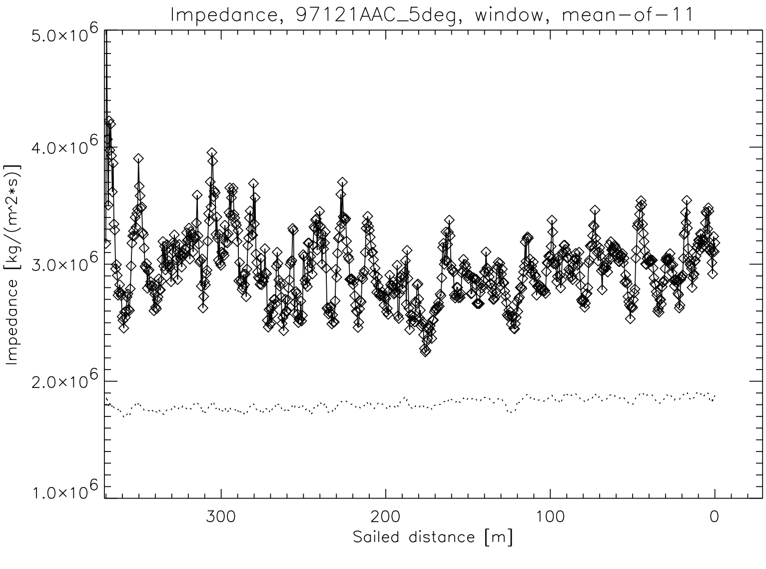

Figure 6.18: *Impedance estimates by FARIM, from Steinbåen. The estimated impedance without correcting for roughness is shown in the lower dotted line.*

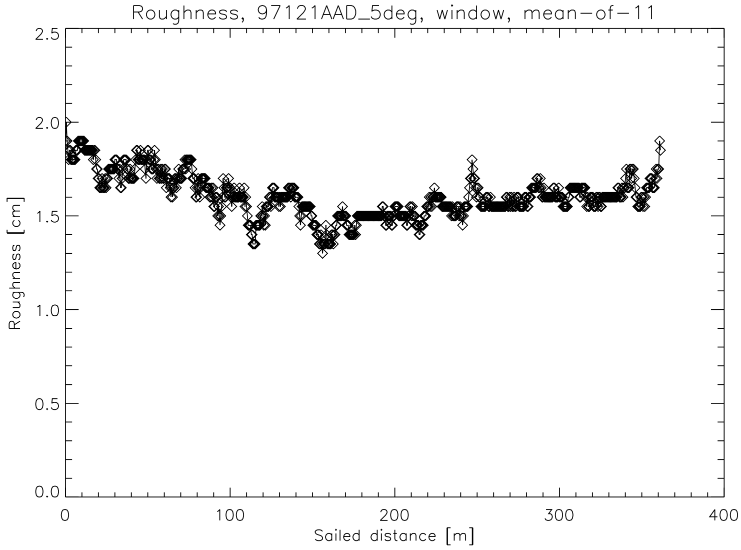

Figure 6.19: *Roughness estimates by FARIM, from Steinbåen.*

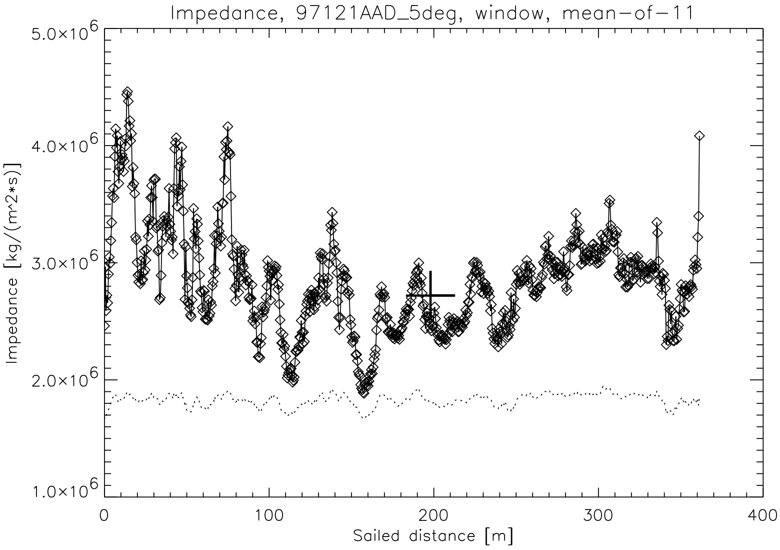

Figure 6.20: *Impedance estimates by FARIM, from Steinbåen. The impedance value from a gravity core is marked with a + sign. The estimated impedance without correcting for roughness is shown in the lower dotted line.*

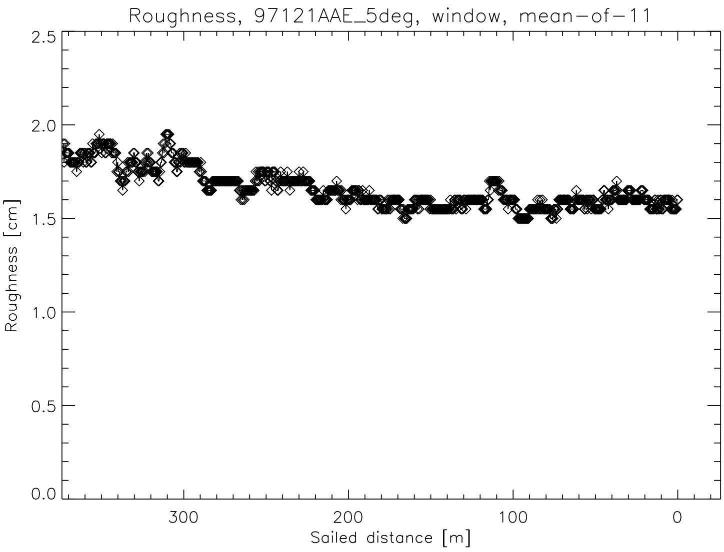

Figure 6.21: *Roughness estimates by FARIM, from Steinbåen.*

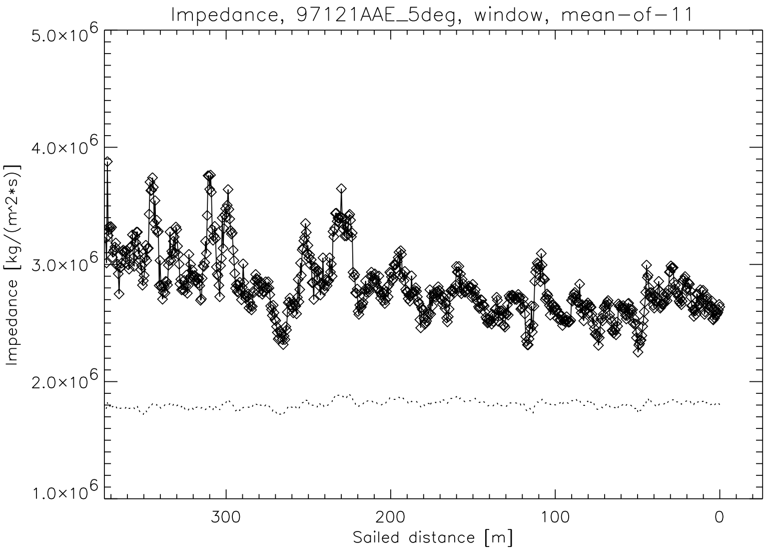

Figure 6.22: *Impedance estimates by FARIM, from Steinbåen. The estimated impedance without correcting for roughness is shown in the lower dotted line.*

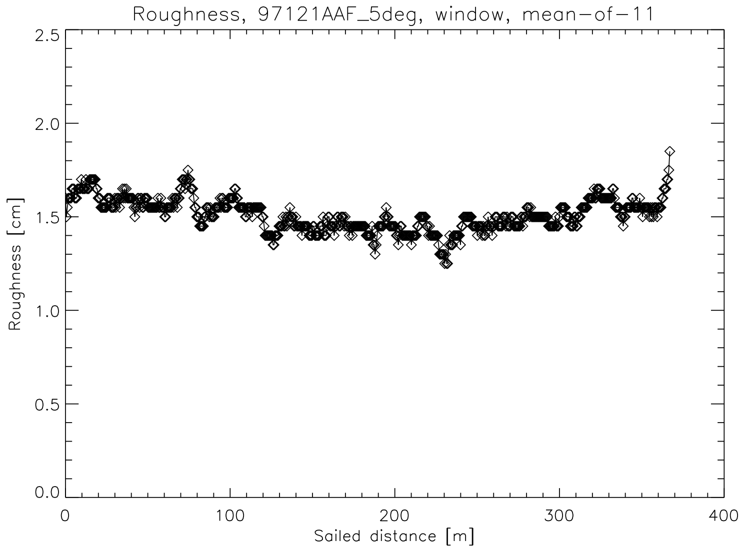

Figure 6.23: *Roughness estimates by FARIM, from Steinbåen.*

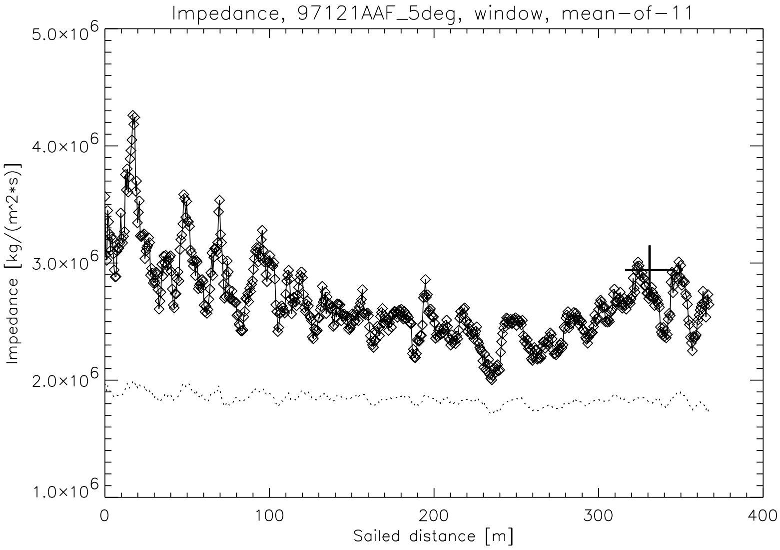

Figure 6.24: *Impedance estimates by FARIM, from Steinbåen. The impedance value from a gravity core is marked with a + sign (at the end of the trace). The estimated impedance without correcting for roughness is shown in the lower dotted line.*

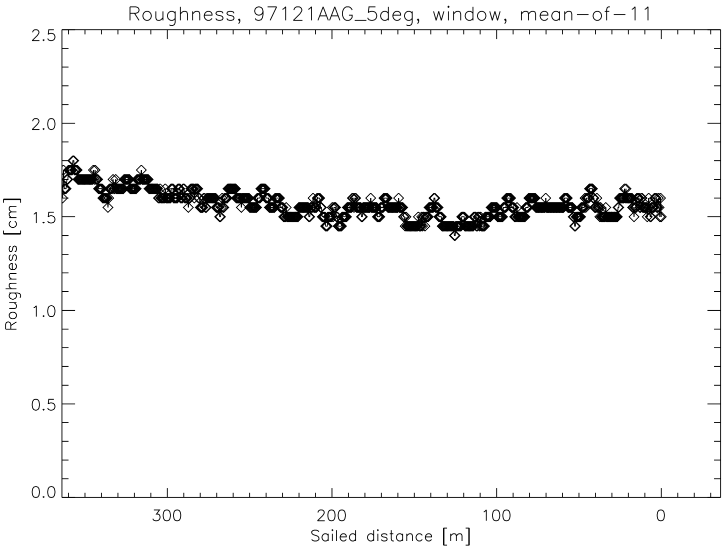

Figure 6.25: *Roughness estimates by FARIM, from Steinbåen.*

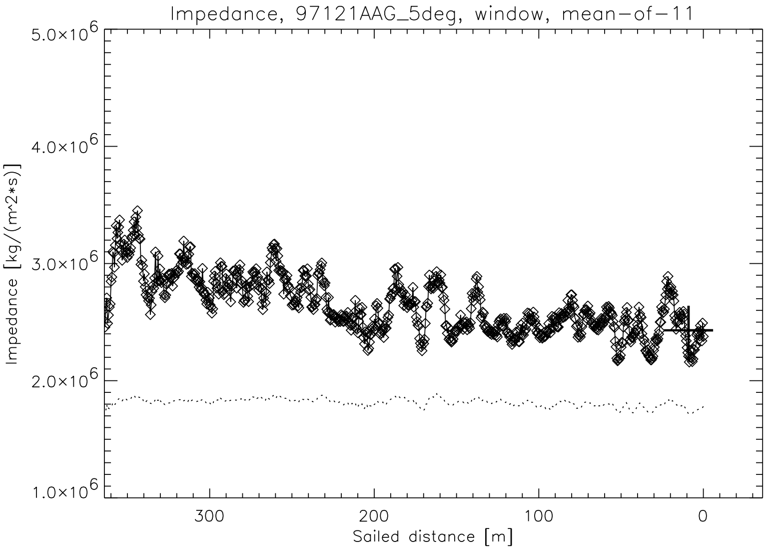

Figure 6.26: *Impedance estimates by FARIM, from Steinbåen. The impedance value from a gravity core is marked with a + sign (at the end of the trace). The estimated impedance without correcting for roughness is shown in the lower dotted line.*

The roughness of the area is from 1.3-2.0cm, and is quite consistent from track to track. Some local variations seem to be repeated on several tracks, and might be caused by e.g. anchor tracks on the seafloor.

The source level was adjusted so that the estimated impedance (including roughness correction) match the measured impedance of three gravity cores available from the analyzed area. A stacking of 11 time traces has been used. This corresponds to a horizontal movement of about 5m.

After this source level calibration, the estimated impedance match well with all the three impedances from the gravity cores. The impedance varies in the area, with typically lower values in the south-east part. There is a fair consistency between the tracks, and some local features (e.g. high impedance values in the northern-most part of most tracks) seem to be repeated over several tracks. The impedance without correcting for roughness (Fig. 6.14) is too low for the given seafloor and the impedance values from the cores, and also show quite a bit of variability. This shows the importance of correcting the impedance estimates for roughness.

The same source level was used during the analysis of the Baltic data, giving a good match between the FARIM estimated impedance and the one estimated from other methods (see Sec. 6.1.3). The seafloors at the North Sea site and the Baltic site 2 where of fairly different types. This seems to be a very good validation of the applied calibration of source level, and at the same time improves the confidence in the FARIM estimation method.

A correction for the seafloor slope was done, using the mean slope of the area. This was especially important since the sonar on MS Simrad is mounted with a tilt of about 1.5°, such that when measuring along a down-sloping surface this tilt in effect is added to the seafloor slope. A more accurate correction for seafloor slope would probably have improved the results even more.

The pulse that was utilized was a 'Burst' pulse, a short pulse with two peaks in the frequency spectrum[2]. These peaks were at about 4kHz and 10-12kHz. The analysis showed that using the lower part of the spectrum was suspicious, possibly due to the low-pass filtering in the measurements or calibration uncertainties. A band pass filter between 8000kHz and 14000kHz was therefore used. This leads to less coherent scattering content in the data. We would therefore expect less accuracy and more random variation in the estimates, especially for the impedance, compared to results from using the whole spectrum. The variation in the estimated roughness and impedance is larger than

---

[2] This type of pulse is used in order to get a maximum of energy into the water while maintaining a short pulse. The pulse is shown in Fig. 2.12, page 37.

e.g. what was found in the estimation of the Mediterranean data. The mean accuracy however seems to be fairly good for both roughness and impedance, both qualitatively and quantitatively. The estimated impedance corresponds very nicely with the gravity cores, and all in all seems reasonable for the given seafloor.

The survey lines at Steinbåen are parallel, and by comparing the different lines the correlation between them is evident, further improving the confidence in the method. It can however be noticed some difference between the estimates depending on the direction of the survey lines. This is mainly due to the incidence angle correction to the impedance, which was crude and based on the mean slope in the area. Using the local along-track slope, or even better the correct local slope (determined from TOPAS or multibeam data), would have been better.

6.1.3 Field data from the Baltic

The data from the Baltic area was collected in the ISACS Baltic Main Sea Trials, Aug 27- Aug 31 1997 at two test sites in the Stockholm archipelago. This was a cooperation between the ISACS partners FOA (Swedish Defense Research Establishment) and Simrad AS. The vessel MS Simrad was utilized. Bottom penetrating sonar (TOPAS), multibeam echosounder (EM 1000) and sidescan sonar were used. In addition to these two surveys there were recorded TOPAS data on both buried and unburied objects. This was done on a small part of Site 2.

The seabed of the Baltic site 2 area consists of a rather inhomogeneous layer, about 1.5m thick, of soft postglacial clay and mud (gyttja clay with an organic carbon content of 3%). The uppermost deposits consist occasionally of very soft, almost suspended materials. Some gas content is suspected in the sediments. There is no vegetation on the fairly smooth seafloor, but locally there are some outstanding features, as old timber on and in the bottom near the south-east part of the area (along the coast line). There are considerable layering in the area, with layers penetrating the surface in some occasions.

Site 2 has been analyzed by FARIM. A Ricker pulse centered at 5kHz was utilized. Both bottom properties of the area and the results of the analysis has been discussed with FOA[3]. An effort was done, by DIST (the developers of sirOb) and FOA, to analyze the area with the alternative method sirOb[4], but

---

[3] Discussions with FOA involved, among others, I. Karasalo, M. Levonen, P. Morén, J. Pihl, P. Söderberg

it was found difficult due to the complex appearance of the data, leading to uncertain estimates. A comparison between FARIM and sirOb, when applied to data from the Baltic, is presented in [18].

The bathymetry of the Baltic site 2 area is shown in Fig. 6.27. Figure 6.28 shows the estimated roughness of the site, while Fig.6.29 shows the estimated impedance. The estimates are shown in color codes on a two-dimensional plot of the survey area. A stacking of 11 time traces was used in the processing.

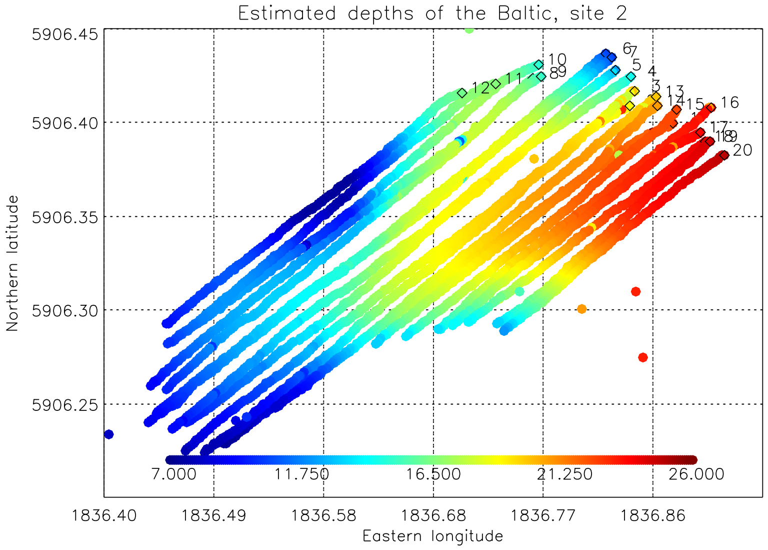

Figure 6.27: *The bathymetry of Baltic site 2, determined from the parametric sonar data.*

A steel sphere is buried at the position 59°06.354’N, 18°36.655’W. None of the tracks directly hit the sphere, even if they were close. The impedance at that location has been estimated by Ivansson to $1.56{\cdot}10^6 kg/(m^2 s)$ ([37]), by comparing the return from the sphere with the return from the seafloor (using other data than presented here). This is very close to the FARIM estimated impedance value near the sphere, see Fig. 6.28. The impedance is somewhat correlated to the bathymetry, which corresponds to a possible ’sediment sliding’ at slopes, giving locally a less dense and smoother (at the surface) sediment, thus lower impedance. It should however be noted that the impedance estimates are not corrected for incidence angle, and the impedance will be somewhat underestimated where the seafloor slope is large.

---

[4] The sirOb method was briefly presented in Sec. 6.1.1

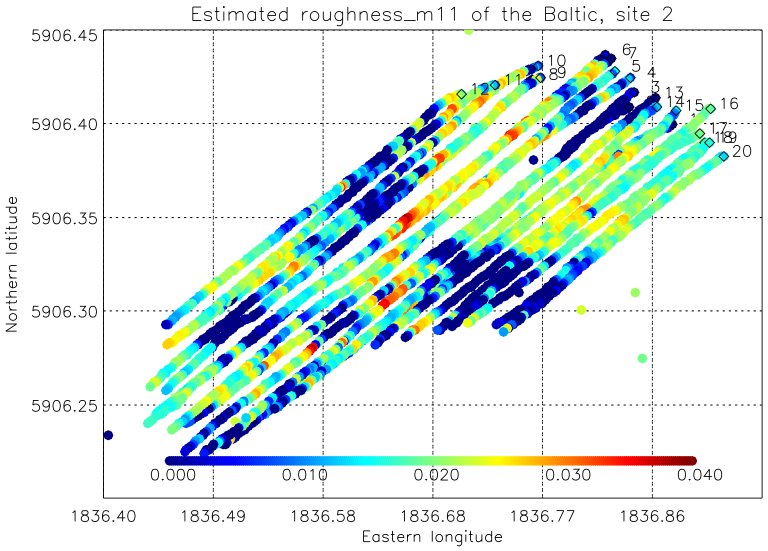

Figure 6.28: *The estimated roughness of the seafloor in the surveyed area, in meters. The distribution seems on the whole to be associated to the bathymetry, which mostly can be confirmed from side scan pictures. A locally higher roughness may be observed close to the object locations.*

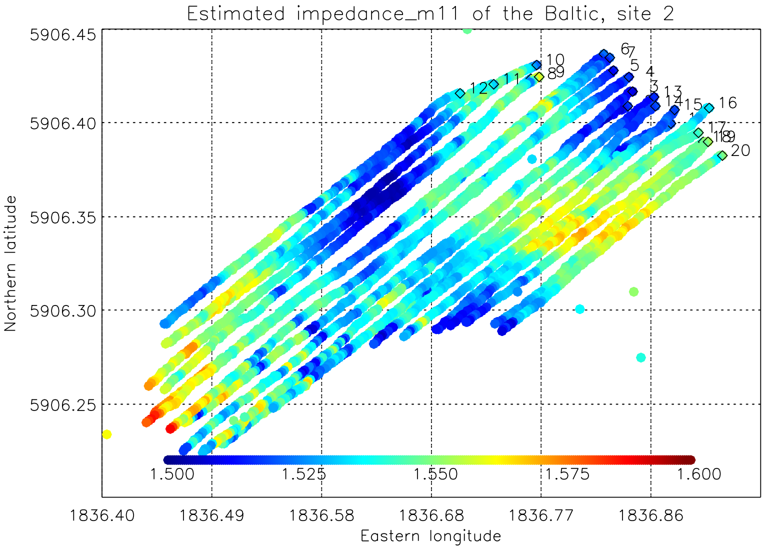

Figure 6.29: *The estimated impedance of Baltic site 2. The distribution is somewhat correlated to the bathymetry, which seems reasonable considering the geological properties of the area.*

The estimated roughness seems to be associated with the bathymetry of the area, which can be confirmed from side scan pictures and be explained by a possible 'sediment sliding' at slopes (leading to a smooth surface). A locally higher roughness can be observed close to the buried steel sphere, and might be explained by the distortion of the sediment in that area. This is only visible in the roughness estimates, not on the impedance estimates. Apparently, the bottom is disturbed because of the object that was buried, but the impedance is unchanged (the object was not directly hit by the TOPAS beam). Another example of an area visible in the roughness estimates but not on the impedance estimates can be found south-west in the area, where the surface looks very smooth. This has been confirmed trough side-scan sonar images. Some spots of higher roughness can also be observed in the sunken timber area. Most of these are also visible in the impedance estimates.

The soft inhomogeneous seafloor combined with the layering makes the area much more difficult to analyze than the other areas being investigated with FARIM. It is seen that the pulse shape in some occasions is completely distorted and irrecognizable. However, the results obtained are fairly consistent and seems reasonable when compared to knowledge about the area, improving the confidence in the method. It must be noted however that the roughness has sometimes been estimated to 0cm, which is unrealistic. However, this behavior is also consistent, and even if the estimated roughness value might not be entirely correct it is calculated from the center frequency shift in the data, which quite clearly seems to be connected to the physics of the area. There are at least two possible explanations to this behavior, apart from the complicating seafloor features mentioned above:

1. From sensitivity analysis we know that a high volume inhomogeneity contributes to a higher CofG in the returned signal, thus leads to an underestimation of the seafloor roughness. This has not been accounted for in the analysis of the field data.
2. The pulse shape that has been used[5] is not from the actual sonar, as this was not available. The pulse shape is important in the estimation process, and thus can contribute to the observed behavior of the method.

6.2 Summary and conclusions

Field data from different sites in the Mediterranean, North Sea and Baltic have been analyzed. The findings are summarized in the following:

- There is a good agreement between the impedance estimates by FARIM and the ground truth impedance (after proper calibration of the data). The difference between estimated impedance and the ground truth values was within the uncertainty of the core measurements and the difference between the core positions and the acoustic track.
- Both the estimated roughness and impedance fit well with available information about the surveyed areas (ground truth, video, divers impressions, side-scan and multibeam sonar, geophysicists knowledge).
- There is however a fairly strong correlation between estimated impedance and estimated roughness, which might indicate a slightly too strong correction of the impedance (for the roughness). This should be further investigated, even though the indications are weak. Possible causes for such overestimation can stem from the calibration, probably either the

---

[5] Calibration data for the TOPAS PS040 (e.g. same type of instrument) of SACLANTCEN has been used.

beam pattern or pulse shape, or from the assumptions of the seafloor surface spectrum (from the sensitivity analysis, the high-pass cut-off frequency seems to be the most likely cause of this).

- 'Difficult data', as the Baltic data (Sec. 6.1.3), have also been analyzed with FARIM with good results. However, some caution should be taken when the estimation technique is applied to such data. These situations can be identified by looking at statistical measures, as standard deviation of estimates.

- FARIM has been applied to data clearly outside the range of validity of the Kirchhoff approximation (e.g. the Scoglio Africa area, Sec. 6.1.1). Such situations are easily identified (by larger standard deviations of the estimated values), and the method behaves in a predictable and consistent manner while giving significant information about the roughness and impedance of the area.

- The calibration of the sonar system is important in order to get accurate results. Calibration can be done of the system itself (pulse shape and source level, shape of the beam pattern, near-field effects) or with measurements on a controlled site where the depth, roughness and impedance is known. The latter method may be used without any other calibration information. This has however not yet been tested, and the FARIM software must be slightly adapted for this use.

- The estimation method relies on measurements of the center frequency shift and the returned energy, and these features can in principle be used for classification/segmentation even without a calibration of the system.

- Some specific features of the seafloor (as e.g. the disturbed area around the buried objects in the Baltic, as well as a very smooth larger area at the same site, see Sec. 6.1.3) can be identified only on the surface roughness estimates, not on the estimated impedance (or energy). This is a very good indication that estimates of roughness indeed can give valuable information of the seafloor that are not necessarily available by other (easily accessible) means.

- Variation along the survey lines are gradual and consistent, indicating that they are indeed connected to the physics of the seafloor and not just statistical variations.

- Stacking is important, and seems to be even more important for field data than synthetic data. This may be because stacking also suppresses noise and effects not incorporated in the model.
- Corrections for depth, source level and near-field effects (reduced effective source level) are important. This is done automatically in FARIM.
- Correction for inclination angle with the seafloor can be important in some cases, when using a narrow beam like the TOPAS beam. The sensitivity analysis, and also experience from analysis of field data, suggests that this is necessary for inclination angles above 1.5-2°.

As a final conclusion, the results from analyzing both synthetic and field data, as well as verification against available information (ground truth etc.), show very promising results. However, more verification of the estimation technique should be done.

Chapter 7

Summary and conclusions

This chapter contains summary and conclusions of the work presented in the preceding chapters. Suggestions for further work are also presented.

7.1 Summary and conclusions

The theoretical treatment shows that there is a potential in using the apparent frequency shift in the coherent return to estimate the seafloor RMS roughness height. This frequency shift is due to the higher frequencies being scattered away more than the lower frequency components, on a rough seafloor.

An analysis of a monostatic sonar system shows that most factors in the scattering process can be controlled or accounted for, such that a characterization should be feasible. An estimate of the surface return compared to the volume return, as a function of time, showed that a window may be used to extract the surface reflection while minimizing the effect of the volume return.

The sensitivity analysis does not reveal any major drawbacks or limitations of the estimation method. The analysis showed that accurate estimation of roughness and impedance should be possible, and that most influencing parameters can be accounted for. The high pass filter wave number was the only surface height spectrum parameter that was found to have any significant effect on the energy and frequency shift.

The implementation of the algorithm has been verified on synthetic data, with good results. For moderate roughness (less than 3cm, which corresponds to 15% of the incoming wavelength), the mean standard deviation for 5 stacked traces were 5% for the estimated roughness and 1% for the estimated impedance. The effect of stacking is significant, which was demonstrated. Error measures was shown to give a good indication of the accuracy of the estimates.

Field data, from the Mediterranean, North Sea and Baltic, have also been analyzed. Good agreement was found with available ground truth. Errors of the impedance estimates were within the uncertainty of the core measurements and slight difference between core positions and the acoustic track. The roughness estimates could only be evaluated qualitatively, with good results. Fair agreement was also found with results from alternative characterization methods.

The FARIM algorithm is computationally very efficient, and can be used for real time calculations.

The algorithm has so far been tested with relatively low frequency sonars (a few kHz) with a narrow beam (a few degrees), utilizing broad-band pulses or multiple frequencies. Careful calibration of the sonar equipment is necessary in order to obtain good results.

7.2 Further work

The estimates of roughness and impedance by FARIM are in good agreement with available ground truth. We however still feel that more verification of the method on field data would be advantageous, with emphasis on comparison with ground truth data.

The sensitivity analysis indicates that the high pass filter wave number in the seafloor roughness description influences the estimation results. The effect of this should be further investigated, together with studies of roughness (both RMS height and the roughness spectra) for real seafloors.

The FARIM estimation method has been applied to data from a parametric sonar. The method can however also be utilized on data from other types of sonars, at least for relatively low frequency sonars. This could be very useful. Sweden´s Defense Research Establishment (FOA) has tested FARIM on data from a conventional sub-bottom profiler, and found the results to be in good agreement with ground truth data and results from FARIM using data from the parametric sonar TOPAS PS040 [40]. Bistatic configurations can, in principle, also be used.

FARIM needs as input the return from a flat seafloor illuminated and measured with the specific sonar. So far this has been done by calibration of the sonar system, more specifically by accurately measuring the beam pattern and source level as well as the signal shape and near field effects of the sonar. Then this has been used to numerically compute the return from a flat seafloor. However, theory predicts a relation between the return from a flat and a rough seafloor, indicating that in principle a sufficient calibration of the sonar system can be done by measurements of backscatter from the seafloor (just like on a normal survey) on a well-controlled site where seafloor impedance and roughness are known. This may often be far easier than direct calibration, and should therefore be investigated. FARIM can relatively easy be adapted to this, but the accuracy of such an approach needs to be determined.

The estimation technique is based on using the coherent return. At higher frequencies, e.g. typical multibeam echosounder frequencies, there is less coherent scattering and more diffuse scattering. The FARIM algorithm might not be directly applicable for such echosounders. However, using the apparent frequency shift and the energy of the signal can still be very interesting. If a characterization is not feasible, a classification or segmentation may be done.

The volume inhomogeneities coefficient and the volume attenuation might be estimated by using the volume return as a function of time. The results presented in a preliminary study of seafloor characterization [11] indicate that this is feasible. Estimation of the volume inhomogeneities coefficient and attenuation may favorably be included in the FARIM software package.

Appendix A

Sensitivity to numerical parameters

A.1 Sensitivity to numerical parameters of BORIS

A.1.1 Introduction

This note describes a sensitivity study of the numerical parameters in BORIS, namely the surface sampling interval, surface patch length, volume sampling interval, volume patch length and bottom penetration depth. The test involved running BORIS on the predefined class C2 (sand, see Table 2.2, page 39), while varying the numerical parameters, one at a time. Sections A.1.2–A.1.6 describes the effect of each parameter on the resulting time-series. The effect on the computing time used is shown in section A.1.7. Some conclusions are drawn in section A.1.8.

The physical parameters of class C2 and the default modeling parameters are described in section A.1.9. The center frequency of the transmitted Ricker pulse is 8kHz, which corresponds to a wave length of about 0.19m in water. The band width is about 10kHz. The footprint of the utilized 2.5 degrees (half-width) synthetic Gaussian shaped beam is about 0.65m in radius. The depth was set to 15m during the simulations.

A.1.2 Variation in the surface sampling

This section describes the influence of the surface sampling on the resulting time series. Figure A.1 shows time series computed at different surface sampling intervals in one plot, while Figs. A.2-A.8 show different realizations at a fixed value of the surface sampling. The surface sampling values are given in meters.

From the figures we see that the surface part starts to deteriorate at sampling intervals 0.48m and 0.96m. The volume part seems to be higher for sampling interval 0.96m than for the other intervals. In the BORIS documentation [25] it is stated that the surface sampling should be smaller than or equal to the surface patch length divided by 16. The surface patch length is here 7.68m, corresponding to a preferred sampling interval equal to or lower than 0.48m. The signal wave length is about 0.19m, as stated above.

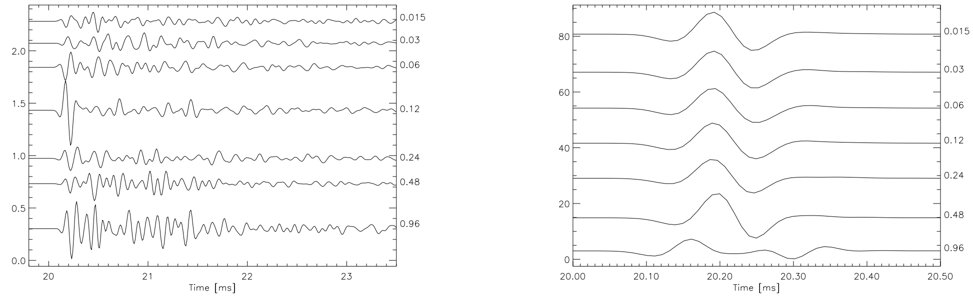

Figure A.1: **Variation of the surface sampling.** *The different sampling intervals used are shown in the legend. The left figure shows the volume contribution while the right one shows the surface part.*

A.1.3 Variation in the surface patch length

This section describes the influence of the surface patch length on the resulting time series. Figure A.9 shows time series computed with different surface patch lengths in one plot, while Figs. A.10-A.14 show different realizations at a fixed value of the surface patch length. The surface patch length values are given in meters.

The value 0.24m for the surface patch length was not handled at all by BORIS. In the BORIS documentation [25] it is stated that the surface sampling should be smaller than or equal to the surface patch length divided by 16. In this case

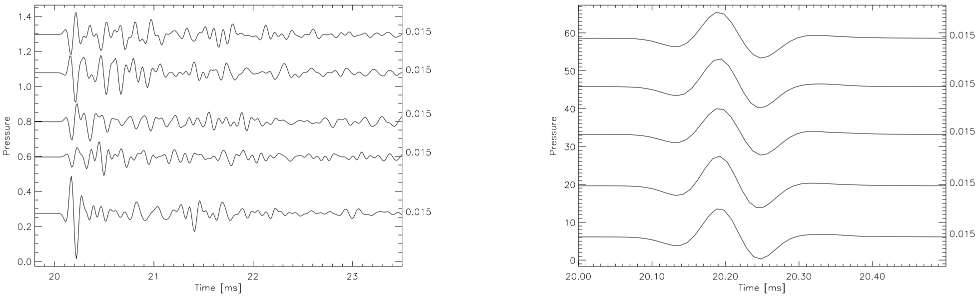

Figure A.2: *Different realizations at one surface sampling interval (see legend). The left figure shows the volume contribution while the right one shows the surface part.*

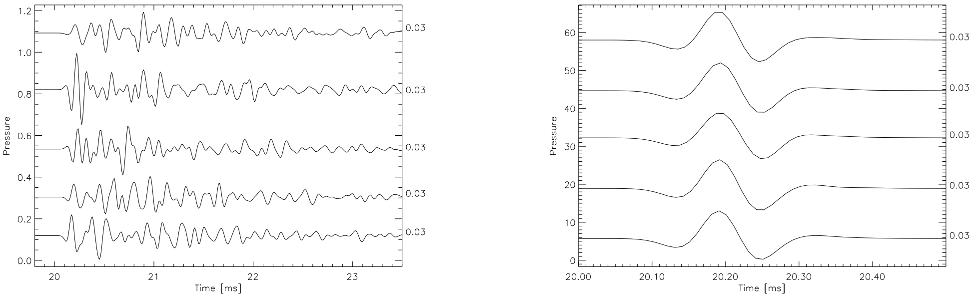

Figure A.3: *Different realizations at one surface sampling interval (see legend). The left figure shows the volume contribution while the right one shows the surface part.*

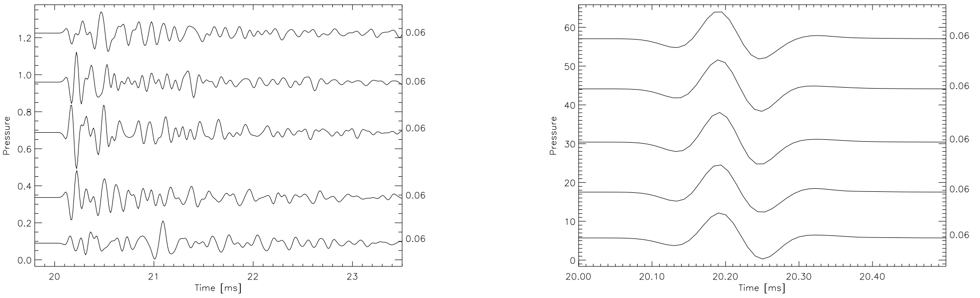

Figure A.4: *Different realizations at one surface sampling interval (see legend). The left figure shows the volume contribution while the right one shows the surface part.*

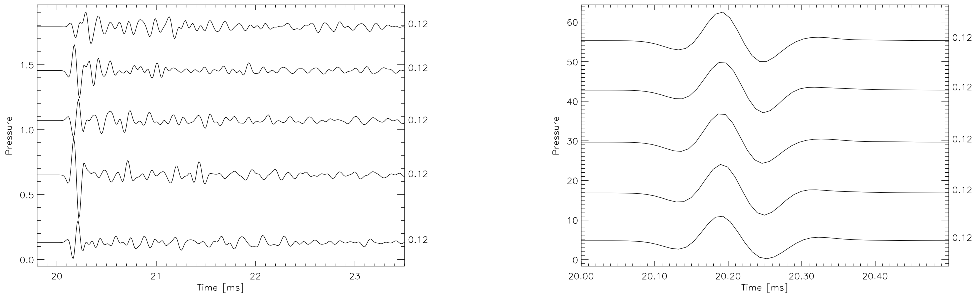

Figure A.5: *Different realizations at one surface sampling interval (see legend). The left figure shows the volume contribution while the right one shows the surface part.*

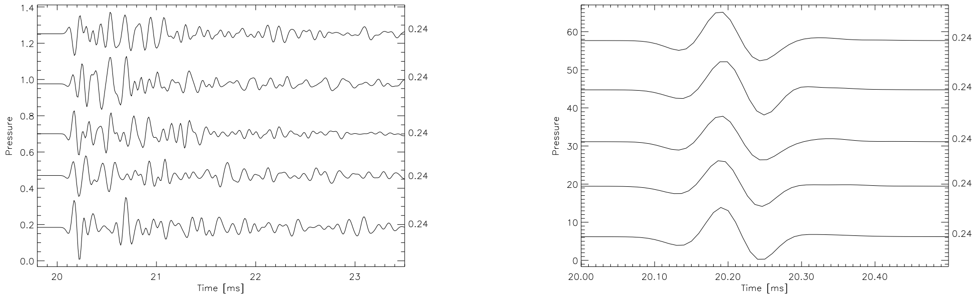

Figure A.6: *Different realizations at one surface sampling interval (see legend). The left figure shows the volume contribution while the right one shows the surface part.*

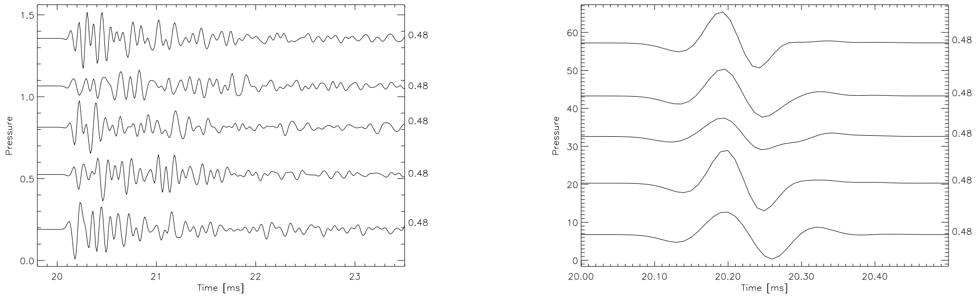

Figure A.7: *Different realizations at one surface sampling interval (see legend). The left figure shows the volume contribution while the right one shows the surface part.*

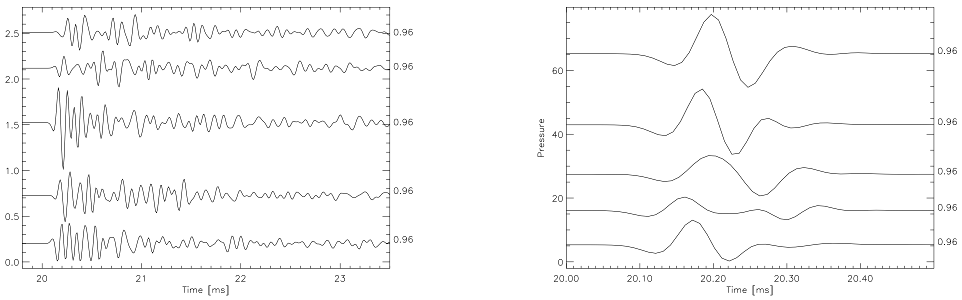

Figure A.8: *Different realizations at one surface sampling interval (see legend). The left figure shows the volume contribution while the right one shows the surface part.*

we used a sampling interval of 0.03m, thus the surface patch length should be equal to or larger than 0.48m. Our investigation confirms this as a necessity in that BORIS would not run. When this condition is satisfied, our plots show no evidence that a larger surface patch length than 16 times the sampling interval is to be preferred, even if the footprint covers several surface patches. Note that this argument applies only to the case we have discussed (where we have a fairly small footprint).

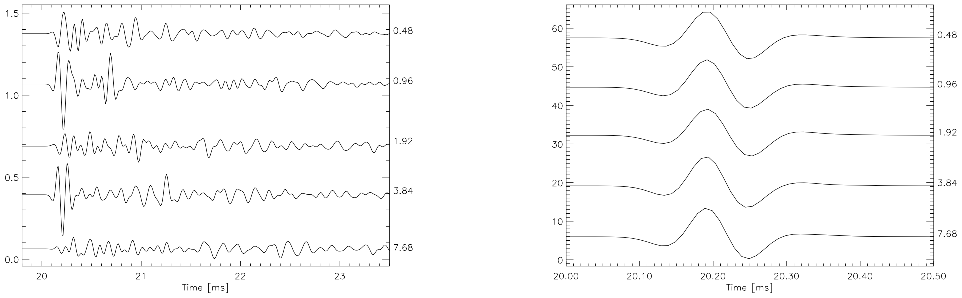

Figure A.9: **Variation of the surface patch length.** *The different lengths used are shown in the legend. The left figure shows the volume contribution while the right one shows the surface part.*

A.1.4 Variation in the volume sampling

This section describes the influence of the volume sampling on the resulting time series. Figure A.15 shows time series computed at different volume sam-

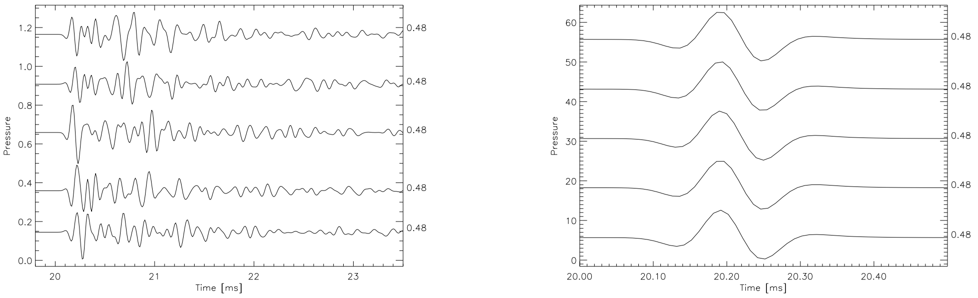

Figure A.10: *Different realizations at one surface patch length (see legend). The left figure shows the volume contribution while the right one shows the surface part.*

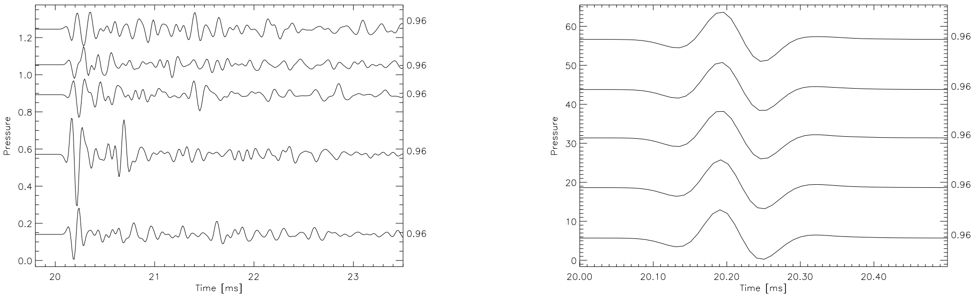

Figure A.11: *Different realizations at one surface patch length (see legend). The left figure shows the volume contribution while the right one shows the surface part.*

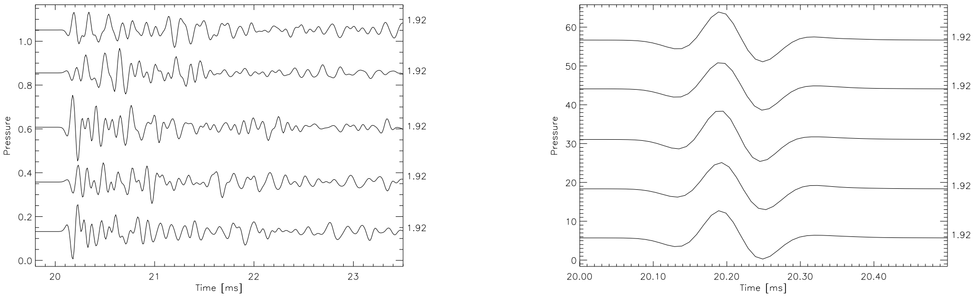

Figure A.12: *Different realizations at one surface patch length (see legend). The left figure shows the volume contribution while the right one shows the surface part.*

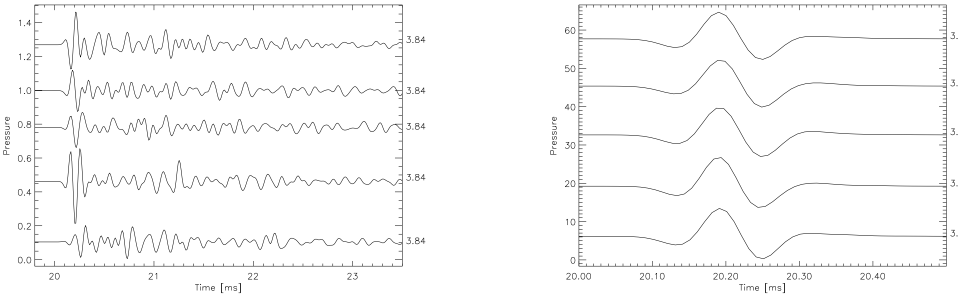

Figure A.13: *Different realizations at one surface patch length (see legend). The left figure shows the volume contribution while the right one shows the surface part.*

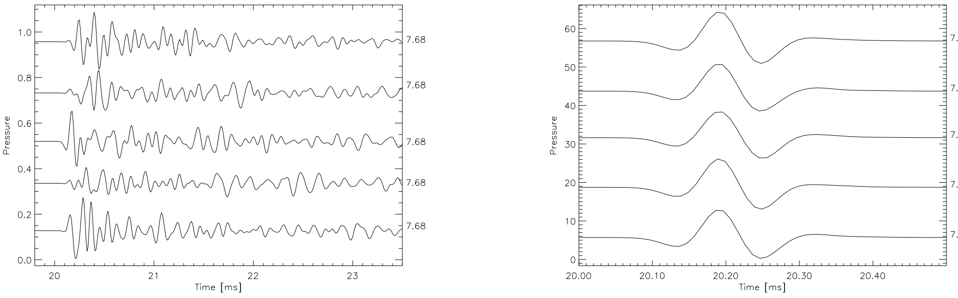

Figure A.14: *Different realizations at one surface patch length (see legend). The left figure shows the volume contribution while the right one shows the surface part.*

pling intervals in one plot, while Figs. A.16-A.20 show different realizations at a fixed value of the volume sampling. The volume sampling values are given in meters.

The value 0.96m for the volume sampling was not handled by BORIS, but the model ran with the value set to 0.48m or lower. In the BORIS documentation [25] it is stated that the volume sampling should be smaller than or equal to the volume patch length divided by 16. In this case we used a volume patch length of 3.84m, thus the volume sampling interval should be equal to or smaller than 0.24m. As seen in the figures, the surface contribution is similar for all volume patch lengths, as expected, but the amplitude of the volume contribution varies a lot even for volume sampling intervals at and below 0.24m. The amplitude grows larger for larger volume sampling intervals. It is also seen some irregularity in the signal at sampling intervals 0.24m and 0.48m, indicating that these are too high to achieve satisfactory results.

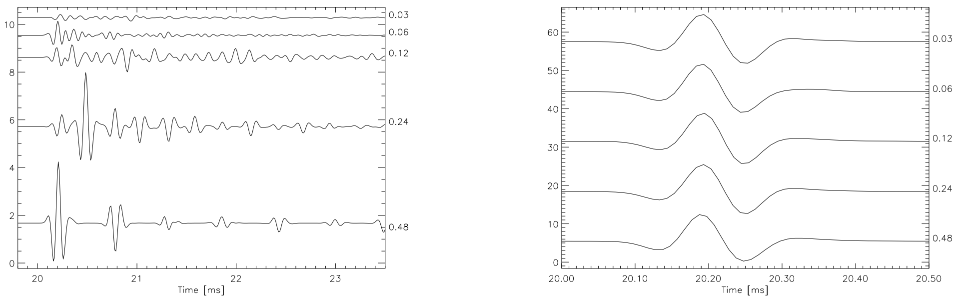

Figure A.15: **Variation of the volume sampling.** *The different sampling intervals used are shown in the legend. The left figure shows the volume contribution while the right one shows the surface part.*

A.1.5 Variation in the volume patch length

This section describes the influence of the volume patch length on the resulting time series. Figure A.21 shows time series computed with different volume patch lengths in one plot, while Figs. A.22-A.26 show different realizations at a fixed value of the volume patch length. The volume patch length values are given in meters.

The value 0.12m for the volume patch length was not handled by BORIS. In the BORIS documentation [25] it is stated that the volume sampling should be smaller than or equal to the volume patch length divided by 16. In this case

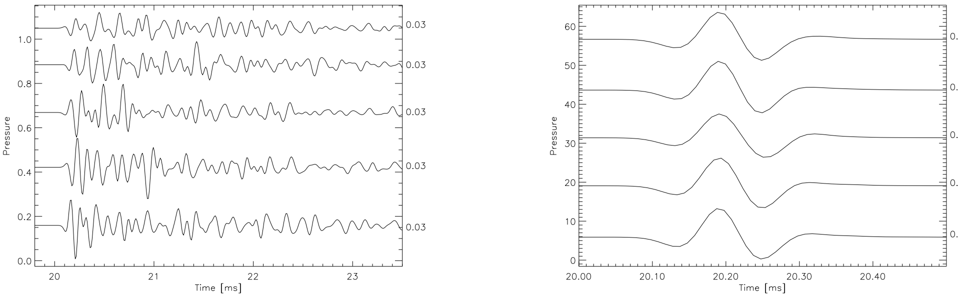

Figure A.16: *Different realizations at one volume sampling interval (see legend). The left figure shows the volume contribution while the right one shows the surface part.*

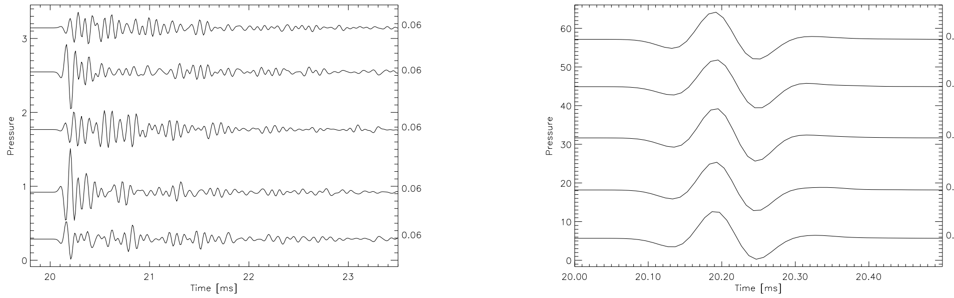

Figure A.17: *Different realizations at one volume sampling interval (see legend). The left figure shows the volume contribution while the right one shows the surface part.*

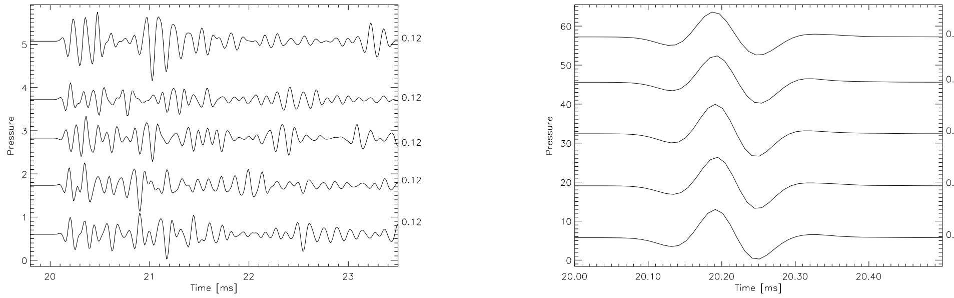

Figure A.18: *Different realizations at one volume sampling interval (see legend). The left figure shows the volume contribution while the right one shows the surface part.*

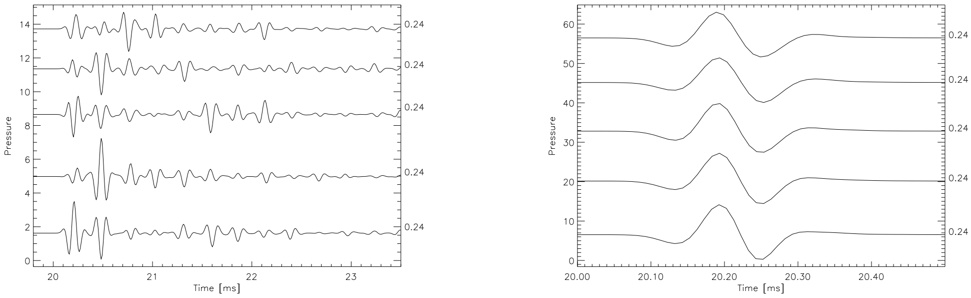

Figure A.19: *Different realizations at one volume sampling interval (see legend). The left figure shows the volume contribution while the right one shows the surface part.*

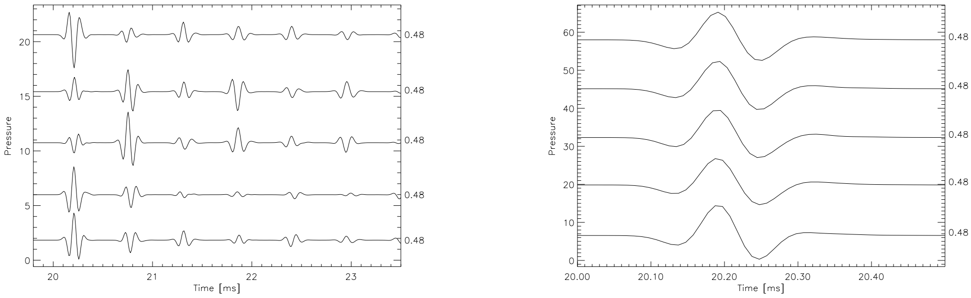

Figure A.20: *Different realizations at one volume sampling interval (see legend). The left figure shows the volume contribution while the right one shows the surface part.*

we used a sampling interval of 0.03m, thus the volume patch length should be equal to or larger than 0.48m. As seen in the figures, the surface contribution is similar for all volume patch lengths, as expected, but the amplitude of the volume contribution varies a lot even for volume patch lengths at and above 0.48m. The amplitude grows substantially larger for larger volume patch lengths.

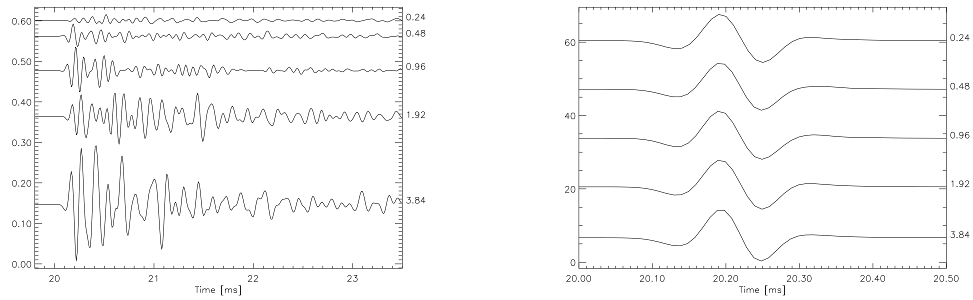

Figure A.21: **Variation of the volume patch length.** *The different lengths used are shown in the legend. The left figure shows the volume contribution while the right one shows the surface part.*

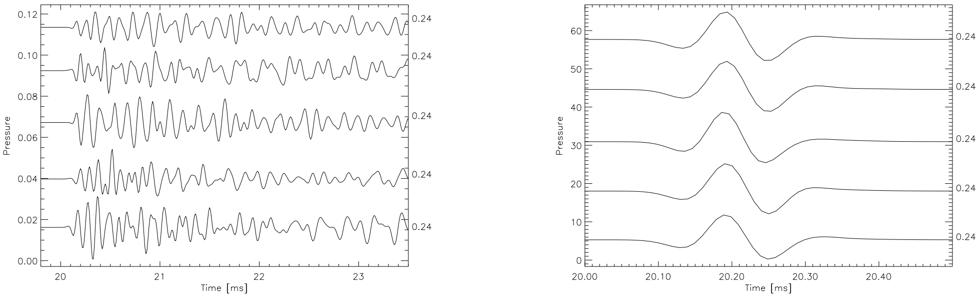

Figure A.22: *Different realizations at one volume patch length (see legend). The left figure shows the volume contribution while the right one shows the surface part.*

A.1.6 Variation in the bottom penetration depth

This section describes the influence of the bottom penetration depth on the resulting time series. Figure A.27 shows time series computed with different bottom penetration depths in one plot, while the other plots show different

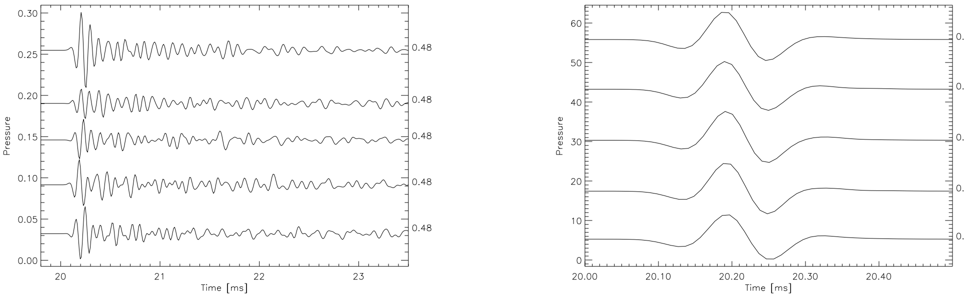

Figure A.23: *Different realizations at one volume patch length (see legend). The left figure shows the volume contribution while the right one shows the surface part.*

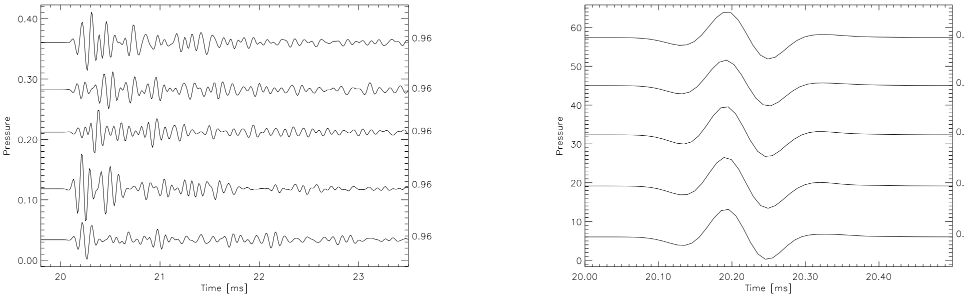

Figure A.24: *Different realizations at one volume patch length (see legend). The left figure shows the volume contribution while the right one shows the surface part.*

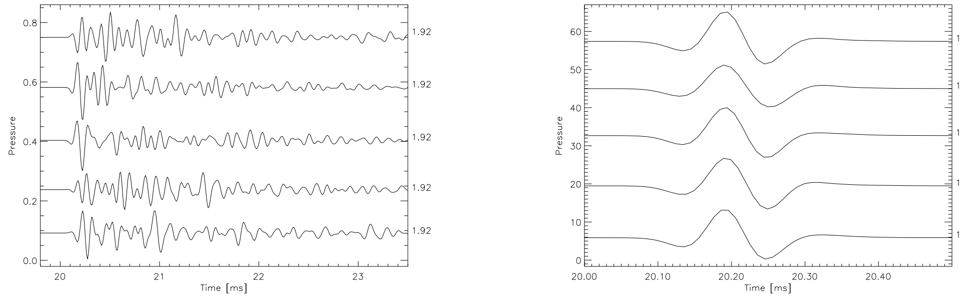

Figure A.25: *Different realizations at one volume patch length (see legend). The left figure shows the volume contribution while the right one shows the surface part.*

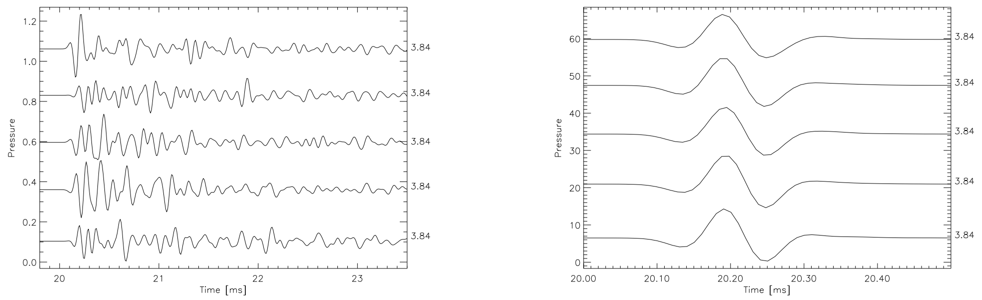

Figure A.26: *Different realizations at one volume patch length (see legend). The left figure shows the volume contribution while the right one shows the surface part.*

realizations at a fixed value of the bottom penetration depth. The bottom penetration depth values are given in meters. The center frequency of the transmitted pulse is 8kHz, which corresponds to a wave length of about 0.19m in water. The footprint of a 2.5degrees (half-width) beam at 15m depth is about 0.65m in radius.

In order to be able to run the simulations with smaller bottom penetration length values than the default, the volume patch length also had to be reduced. It was set to 0.96m.

The double travel time in the sediment, corresponding to penetration depths of 0.96m, 1.92m and 3.84m are, respectively, 1.28ms, 2.56ms and 5.12ms, for a normal incidence beam. This can easily be seen in Fig. A.27. Apart from this, there are no obvious differences between the traces for different bottom penetration depths.

A.1.7 Computing time

The influence of the variation in parameters on the computing time is shown in table A.1.

A.1.8 Conclusions

From sections A.1.2 and A.1.3 on surface sampling interval and surface patch length it seems reasonable to state that the surface sampling interval must be comparable to or lower than the wavelength of the pulse, and that the surface

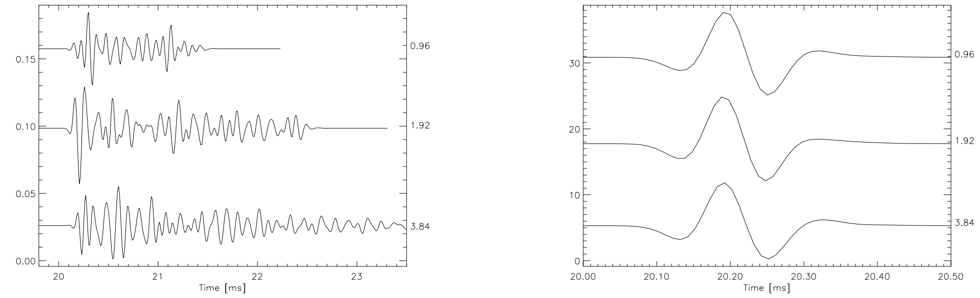

Figure A.27: **Variation of the bottom penetration depth.** *The different lengths used are shown in the legend. The left figure shows the volume contribution while the right one shows the surface part.*

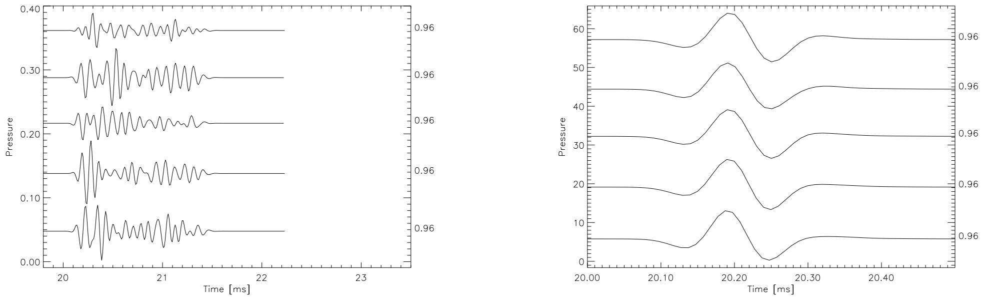

Figure A.28: *Different realizations at one bottom penetration depth (see legend). The left figure shows the volume contribution while the right one shows the surface part.*

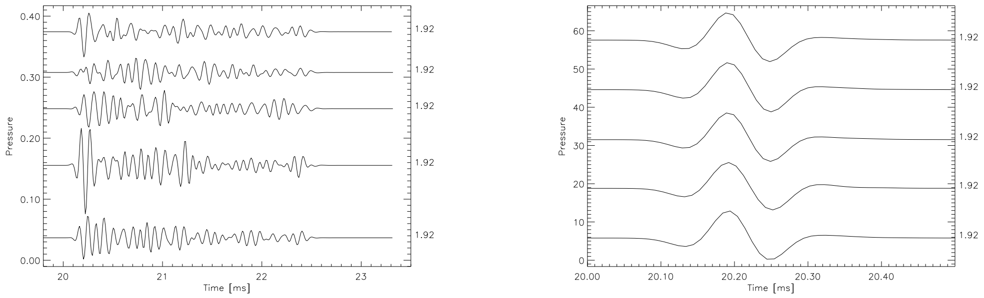

Figure A.29: *Different realizations at one bottom penetration depth (see legend). The left figure shows the volume contribution while the right one shows the surface part.*

Parameter	**Value**	**Mean computing time [s]**
Surface patch length	*7.68m*	*31*
	3.84m	29
	1.92m	29
	0.96m	29
	0.48m	29
Surface sampling	0.96m	18
	0.48m	18
	0.24m	18
	0.12m	19
	0.06m	21
	0.03m	*32*
	0.015m	77
Volume sampling	0.48m	3
	0.24m	4
	0.12m	5
	0.06m	10
	0.03m	*34*
Volume patch length	*3.84m*	*32*
	1.92m	16
	0.96m	14
	0.48m	13
	0.24m	13
Bottom penetration	3.84m	13
NB: vol.length=0.96	1.92m	8
	0.96m	5

Table A.1: *Computing times in second. The value is a mean of 5 runs of the model at a depth of 15m and with the aforementioned parameters. The default values are emphasized. The computing took place on a 200MHz Pentium Pro PC with 64MB RAM, running Windows NT.*

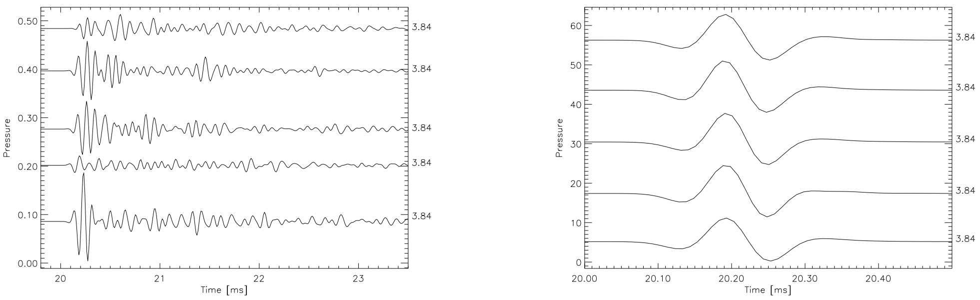

Figure A.30: *Different realizations at one bottom penetration depth (see legend). The left figure shows the volume contribution while the right one shows the surface part.*

patch length should be at least 16 times the sampling interval. However, this limited test shows no evidence that the surface patch length must be larger than the footprint; the footprint was about 1.3m in diameter while the lowest 'good' surface patch length was 0.48m

The effect of the bottom penetration depth was only to affect the time series after the time set by the double travel time in the water column and bottom sediments. The two other parameters involving the volume, the volume sampling interval and volume patch length, were somewhat confusing. As expected they did not influence the surface contribution, but they influenced the volume part even for values which should be OK (according to the BORIS documentation, [25]). For these values, the shape looked reasonable, but the amplitude increased with increasing volume length or volume sampling. A closer look at the values reveals that the volume part amplitude seems very close to proportional to both the volume length and volume sampling interval, with no correlation effects between them. Similar to the surface parameters, the volume length must be at least 16 times the volume sampling interval, and the volume sampling interval should probably not be much larger than the pulse wavelength. If these conditions are not satisfied, it might influence the shape and amplitude of the time series, and in some cases BORIS will not run at all.

A.1.9 Physical and model parameters

The beam that is used is a gaussian beam with a beamwidth of 5 degrees (2.5 degrees half-width). The pulse is a Ricker with a center frequency of 8kHz and a frequency band of about 10kHz.

The model parameters `SURFACE_LENGTH`, `SURFACE_SAMPLING`, `VOLUME_LENGTH`, `VOLUME_SAMPLING` and `BOTTOM_PENETRATION` have been changed during this exercise. Listing of the default values that have been used are listed below, as a typical content of `mod_common.in`:

```
; This file is meant to be a common part for several files
; It is used by Make_MOD etc. to make mod-*.ini files

NORTH_POSITION=0
EAST_POSITION=0

HEADING=0
PITCH=0
ROLL=0

R_START_ANGLE= -10
R_STOP_ANGLE= 10
P_START_ANGLE= -10
P_STOP_ANGLE= 10

SURFACE_LENGTH=7.68              ; Preferably=surf_samp*2^n
SURFACE_SAMPLING=0.03            ; Change dependent on pulse freq.


VOLUME_LENGTH=3.84               ; Preferably=surf_samp*2^n
VOLUME_SAMPLING=0.03             ; Change dependent on pulse freq.
BOTTOM_PENETRATION=3.84          ; Set to 0 for no volume.

BP_MIN=0

SAMPLING_FREQUENCY=100000
; BORIS_SEED=10                  ; Seed for generating volume and surface
```

Listing of the file `phy-C2.ini`, describing the physical properties of the class C2, fine sand:

```
[Ver_1.0]

; Nametag: C2     Description: Fine sand

SEDIMENT_SOUNDSPEED = 1750
SEDIMENT_DENSITY    = 1.90000
SURFACE_RMS_HEIGHT  = 0.0100000
VOLUME_RMS_HEIGHT   = 0.0200000
SEDIMENT_ATTENUATION= 0.600000

WATER_SOUNDSPEED = 1500
```

```
WATER_DENSITY    = 1
SOURCE_LEVEL     = 1

SURFACE_EXPONENTIAL_PL= 4.00000

WAVE_RMS       = 0.000000
WAVE_NUMBER_RMS= 15
WAVE_DIRECTION = 10
WAVE_NUMBER_N  = 100

VOLUME_H_CORRELATION_LENGTH= 0.300000
VOLUME_V_CORRELATION_LENGTH= 0.0600000

S_HP_FREQUENCY  = 10
S_LP_FREQUENCY  = 30
V_H_HP_FREQUENCY= 0.000000
V_H_LP_FREQUENCY= 200000
V_V_HP_FREQUENCY= 0.000000
V_V_LP_FREQUENCY= 200000
```

Listing of the file `boris.in`, supplying names of input files:

```
[Ver_1.0]

DEFAULT_DIR=
DEFAULT_BP_FILE=gau_025.bp
DEFAULT_PULSE_FILE=r100_8.pls
DEFAULT_ECHO_VOLUME_FILE=vol.out
DEFAULT_ECHO_SURFACE_FILE=surf.out
DEFAULT_VOLUME_FILE=vol.map
DEFAULT_SURFACE_FILE=surf.map

; End of the common part for BORIS.INI
; The following lines specify the files
; containing the model and physics parameters
```

Appendix B

File structure definitions for the TOPAS raw-data format

Below, the file `io_TOPAS.hpr` is listed. It contains the structure definitions for the TOPAS raw-data format.

```
;*********************************************************************
;    This file contains file structure definitions for the TOPAS format
;
;    Time-stamp: <2000-04-04 13:49:13 berntsen>
;
; The names in the structures usually correspond to the TOPAS format,
; but where there are discrepancies between TOPAS and ADAM names, ADAM
; names are (usually...) preferred.
;*********************************************************************

; Define the structure of each TOPAS ping
topasPingHead =  {topasPingHead_struct, $
$
$   ; Block ID + version
    block_id:0, $         ; Block ID
    version:0, $          ; Version
$
$   ; File name etc.
    orgFilename:REPLICATE(' ',16), $  ; Original file name
    line_id:REPLICATE(' ',18), $      ; Line identification
    customer:REPLICATE(' ',20), $     ; Customer
```

```
$
$   ; Time stamps
    year:0, $                ; Start of acquisition info
    month:0, $
    day:0, $
    hour:0, $
    min:0, $
    sec:0, $
    msec:0, $
$
$   ; Transmitter data
    ch_nr:0, $            ; Ch_nr
    level:0, $            ; Level (%)
    interval:0, $         ; Ping interval (ms)
    pulsform:0, $         ; Type of pulse 0=Te, 1=Burst 2=Ricker 3=Chirp ??
    HRP_comp:0, $         ; Heave, roll pitch compensation used 1 = on
    sec_freq:0, $         ; Secondary frequency
    chirp_start:0, $      ; Chirp/CW descriptions
    chirp_stop:0, $
    chirp_length:0, $
    chirp_type:0, $
    beam_dir_along:0.0, $         ; Beam direction, alongship
    scan_sec_along:0.0, $         ; Scan sector of beam, alongship
    scan_step_along:0.0, $        ; Scanning step, alongship
    beam_dir_athwart:0.0, $       ; Beam direction, athwart
    scan_sec_athwart:0.0, $       ; Scan sector of beam, athwart
    scan_step_athwart:0.0, $      ; Scanning step, athwart
$
$   ; Environmental data
    lat_north:0.0D, $      ;  Environmental data at start of acquisition
    lon_east:0.0D, $
    zone_lon:0.0D, $
    heading:0.0, $
    speed:0.0, $
    system:0, $
    zone_no:0, $
$
$   ; HPR info
    tx_heave:0.0, $          ; Transmitter
    tx_roll:0.0, $
    tx_pitch:0.0, $
    rx_heave:0.0, $          ; Receiver
    rx_roll:0.0, $
    rx_pitch:0.0, $
$
```

```
$   ; Acquisition data
    delay:0, $               ; Delay (in points)
    delay_ms:0, $            ; Delay (ms)
    length:0, $              ; Acquisition length (in points)
    length_ms:0, $           ; Acquisition length (ms)
    sfreq:0L, $              ; Sampling frequency
    gain:0, $                ; Gain
    hp_filter:0L, $          ; HP filter
    lp_filter:0L, $          ; LP filter
    roll_dir:0.0, $          ; Roll_dir (degrees)
    pitch_dir:0.0 $         ; Pitch_dir (degrees)
$
}    ; End of structure definition
```

Bibliography

[1] W. S. Ament. Toward a theory of reflection by a rough surface. In *Proc. IRE*, volume 41, pages 142–146, 1953.

[2] J. M. Augustin, X. Lurton, et al. Contribution of the multibeam acoustic imagery to the exploration of the sea-bottom. *Marine Geophysical Researches*, 18(2-4):459–486, June 1996.

[3] S. Barnett and T.M. Cronin. *Mathematical Formulae.* Longman Scientific & Technical, 4 edition, 1986.

[4] M.F. Barnsley, R.L. Devaney, B.B. Mandelbrot, H.O. Peitgen, D. Saupe, and R.F. Voss. *The science of fractal images.* Springer Verlag, Berlin, 1988.

[5] P. Beckmann and A. Spizzichino. *The Scattering of Electromagnetic Waves from Rough Surfaces.* Pergamon, Oxford, 1963. (Reprinted 1987 by Artech House Inc., Norwood, Massachussetts, USA).

[6] O. Bergem. ADAM file format specification, ver. 2. Technical note, SACLANTCEN, May 1996. Web: http://www.ntnu.no/ISACS/.

[7] O. Bergem and N. G. Pace. Calibration of the TOPAS PS040. Part 1: Measurements recorded with TOPAS acquisition system. Special Report M-119, SACLANTCEN Undersea Research Centre, La Spezia, Italy, January 1996.

[8] O. Bergem and N. G. Pace. Installation and calibration of a parametric array for shallow water backscatter measurements. *IEEE Transactions*, pages 773–777, 1996.

[9] O. Bergem, E. Pouliquen, G. Canepa, and N. G. Pace. Time-evolution modelling of seafloor scatter. Part II: Experimental verification. Technical Report SM-327, NATO SACLANTCEN, La Spezia, Italy, 1997.

[10] O. Bergem, E. Pouliquen, G. Canepa, and N. G. Pace. Time-evolution modeling of seafloor scatter. II. Numerical and experimental evaluation. *J. Acoust. Soc. Am.*, 105(6):3142–3150, 1999.

[11] B. Berntsen. Preliminary studies of seafloor characterization using BORIS simulations. In *Annual report 1997, MAST III ISACS*. NTNU, Norway, 1997.

[12] B. Berntsen. Classification of the seafloor using predefined classes and numerical simulations. In Halvor Hobæk, editor, *Proceedings of the 21st Scandinavian Symposium on Physical Acoustics*, volume ISSN 0803-2696, Ustaoset, Norway, February 1998. University of Bergen.

[13] B. Berntsen. Model-based estimation of geoacoustic parameters for seafloor characterization, applied to simulated and parametric sonar data. In *Annual report 1999, MAST III ISACS*. NTNU, Norway, 1999.

[14] B. Berntsen. On characterization and classification of the seafloor. In U.R. Kristiansen, editor, *Proceedings of the 22nd Scandinavian Symposium on Physical Acoustics*, volume ISSN 1501-6773, Ustaoset, Norway, February 1999. NTNU.

[15] B. Berntsen. The FARIM seafloor characterization package. In *Final report, MAST III ISACS*. NTNU, Norway, January 2000.

[16] B. Berntsen, S.A. Frivik, and J.M. Hovem, editors. *ISACS – Integrated System for Analysis and Characterization of the Seafloor – Final Report 1996-1999*, NTNU, Norway, January 2000.

[17] B. Berntsen, J.M.Hovem, and O.Bergem. Characterization of the seafloor using normal incidence acoustic backscattered time domain signals from a parametric sonar. In *Proc. OCEANS'99 MTS/IEEE Conf.*, Seattle, Washington USA, Sep. 13-16 1999.

[18] B. Berntsen, I. Karasalo, M. Levonen, P. Moren, and V. Westerlin. Seabed characterization in the Baltic with the SIROB and FARIM methods. Methodology report FOA-R–99-01237-409–SE, ISSN 1104-9154, Defence Research Establishment, Sweden, Oct. 1999.

[19] D.R. Burns et al. Rapid and convenient acoustic sea-bed discrimination for fisheries applications. In *Proc. I.O.A.*, volume 11, 1989.

[20] A. Caiti. Data Inversion and Seafloor Characterization/Classification. In *Final report, MAST III ISACS*. NTNU, Norway, January 2000.

[21] A. Caiti et al. Seabed Characterization by Inversion of Parametric Sonar Data: Selection of the Cost Function. *MAST III ISACS*, 1997.

[22] A. Caiti and R. Zoppoli. Seafloor parameter identification from parametric sonar data. In *Proceedings of the 4th European Conference on Underwater Acoustics*, Rome, Italy, 1998.

[23] A. Caiti and R. Zoppoli. sirOb: an interactive package for inversion of parametric sonar data. In *Proceedings of the IEEE Oceans'98 Conference*, Nice, France, 1998.

[24] G. Canepa and O. Bergem. Small C-routines to read the ADAM data files. Technical note, SACLANTCEN, May 1996. Web: http://www.ntnu.no/ISACS/.

[25] G. Canepa, O. Bergem, and E. Pouliquen. The implementation of Boris-3D: BOttom Response from Inhomogeneities and Surface. Technical Report M-125, SACLANTCEN, La Spezia, Italy, 1997.

[26] C. S. Clay and H. Medwin. *Acoustical oceanography: Principles and applications.* John Wiley and Sons, 1977.

[27] C. de Moustier and H. Matsumoto. Sea-floor acoustic remote-sensing with multibeam echo-sounders and bathymetric sidescan sonar systems. *Marine Geophysical Researches*, 15(1):27–42, February 1993.

[28] S. Dugelay. Deep Seafloor Characterization with Multibeam Echosounders using Image Segmentation and Angular Acoustic variations. In *Proceedings Oceans'96*, 1996.

[29] C. Eckart. The scattering of sound from the sea surface. *J. Acoust. Soc. Am.*, 25:566–570, 1953.

[30] S. A. Frivik. A study on the possibility of using angle dependent acoustic backscattering strength data for seafloor classification. Technical Report 429810, NTNU, Trondheim, Norway, 1998.

[31] M. Gensane. Sea-bottom reverberation: the role of volume inhomogeneities of the sediment. In D.D. Ellis, J.R. Preston, and H.G. Urban, editors, *Ocean Reverberation*, pages 59–64, New York, 1993. Kluwer Academic.

[32] S.M. Goodnick, D.K. Ferry, C.W. Wilmsen, Z. Liliental, D. Fathy, and O.L. Krivanek. Surface roughness at the Si(100)-SiO_2 interface. *Phys. Rev B*, 32:8171–8185, 1985.

[33] E. L. Hamilton. Geoacoustic modeling of the sea floor. *J. Acoust. Soc. Am.*, 68:1313–1340, 1980.

[34] E. L. Hamilton. Acoustic properties of sediments. In *Acoustics and ocean bottom, F.A.S.E. Conference.* Madrid, June 1987.

[35] E. L. Hamilton and R. T. Bachman. Sound velocity and related properties of marine sediments. *J. Acoust. Soc. Am.*, 72:1891–1904, 1982.

[36] ISACS: Integrated System for Analysis and Characterization of the Seafloor, Project proposal under the MAST III initiative, March 1996. Project coordinator: Jens M. Hovem, NTNU.

[37] S. Ivansson. Private communication. FOA, Sweden, 1999.

[38] D. R. Jackson. Application of the composite roughness model to high-frequency bottom backscattering. *J. Acoust. Soc. Am.*, 79(5), May 1986.

[39] F.B. Jensen, W.A. Kuperman, M.B. Porter, and H. Schmidt. *Computational Ocean Acoustics.* AIP series in modern acoustics and signal processing. American Institute of Physics, USA, 1994.

[40] I. Karasalo. Private communication. FOA, Sweden, 1996-2000.

[41] S.R. Lang et al. The Hilbert Techniques: An Alternative Approach For Non-Steady Time Series Analysis. *IEEE Geoscience and Remote Sensing Society Newsletter*, mar 1995. review article.

[42] X. Lurton. Caractérisation des fonds marins par acoustique: état de l'art et perspectives. *Journal de Physique IV*, 4(C5):1031–1038, May 1994.

[43] X. Lurton and E. Pouliquen. Automated sea-bed classification system for echosounders.

[44] B. Mandelbrot. *The Fractal Geometry of Nature.* W.H. Freeman, New York, 1975.

[45] H. Medwin and C. S. Clay. *Fundamentals of Acoustical oceanography.* Academic Press, 1998.

[46] Z. H. Michalopoulou and D. Alexandrou. Bayesian modeling of acoustic signals for seafloor identification. *J. Acoust. Soc. Am.*, 99(1):223–233, January 1996.

[47] J. A. Ogilvy. *Theory of wave scattering from random rough surfaces.* Adam Hilger, Bristol, 1991.

[48] N. Pace and H. Gao. Swathe seabed classification. *IEEE Journ. Ocean Eng.*, 13(2):83–90, 1988.

[49] Y-H Pao and C-C Mow. *Diffraction of Elastic Waves and Dynamic Stress Concentrations.* Hilger, London, 1973.

[50] E. Pouliquen, O. Bergem, and N. G. Pace. Time-evolution modelling of seafloor scatter. Part I: Theory. Technical Report SM-328, NATO SACLANTCEN, La Spezia, Italy, 1997.

[51] M. Rasigni and G. Rasigni. Surface structure autocorrelation functions and their Fourier transforms for rough deposits of magnesium. *Phys. Rev. B*, 19:1915–1919, 1979.

[52] Research Systems, Inc. IDL – The Interactive Data Language. Web: http://www.rsinc.com/index.cfm.

[53] Documentation from Simrad Norge, N-7501 Stjørdal, Norway.

[54] Simrad Norge AS, Stjørdal, Norway. *Simrad TOPAS PS040 Parametric Sub-bottom Profiler*, 1996. Product description manual.

[55] T. Stanton and C. S. Clay. Sonar Echo Statistics as a Remote-Sensing Tool: Volume and Seafloor. *IEEE Journal of Oceanic Engineering*, OE-11(1):79–96, January 1986.

[56] T.R. Thomas. *Rough Surfaces.* Imperial College Press, London, 2 edition, 1999.

[57] P. D. Thorne and N. G. Pace. Acoustic studies of broadband scattering from a model rough surface. *J. Acoust. Soc. Am.*, 75:133–144, 1984.

[58] W.H. Thorp. Analytic Description of the Low Frequency Attenuation Coefficient. *J. Acoust. Soc. Am.*, (42):270–271, 1967.

[59] R. J. Urick. *Principles of underwater sound.* Peninsula Publishing, California, 3 edition, 1983.

[60] Ståle Vilming. Literature Studies in Swath Bathymetry. Report, NTNU, January 1998.

[61] D.J. Whitehouse and J.F. Archard. The properties of random surfaces of significance in their contact. *Proc. Roy. Soc.*, A316:97–121, 1970.

[62] T. Yamamoto. Acoustic scattering in the ocean from velocity and density fluctuations in the sediments. *J. Acoust. Soc. Am.*, 99(2):866–879, February 1996.